

WL-TR-91-4032
DOT/FAA/CT-91/23
VOL II, Part 3

AD-A249 131



COMPOSITE FAILURE ANALYSIS HANDBOOK
VOLUME II - TECHNICAL HANDBOOK
PART 3 - CASE HISTORIES

R.J. Kar
Northrop Corporation
One Northrop Avenue
Hawthorne, California 90250-3277

February 1992

Final Report for Period January 1987 - October 1990



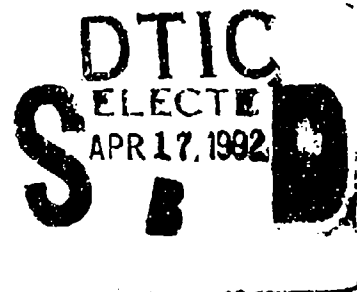
U.S. Department
of Transportation
**Federal Aviation
Administration**

Approved for public release; distribution unlimited.

MATERIALS DIRECTORATE
WRIGHT LABORATORY
AIR FORCE SYSTEMS COMMAND
WRIGHT-PATTERSON AIR FORCE BASE, OH 45433-6533

and

FEDERAL AVIATION ADMINISTRATION TECHNICAL CENTER
U.S. DEPARTMENT OF TRANSPORTATION
ATLANTIC CITY, NEW JERSEY 08405



92-09219




92 09 029

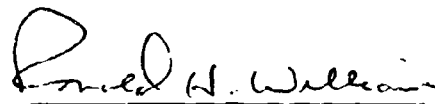
NOTICE

When Government drawings, specifications, or other data are used for any purpose other than in connection with a definitely Government-related procurement, the United States Government incurs no responsibility or any obligation whatsoever. The fact that the Government may have formulated or in any way supplied the said drawings, specifications, or other data, is not to be regarded by implication, or otherwise in any manner construed, as licensing the holder, or any other person or corporation; or as conveying any rights or permission to manufacture, use, or sell any patented invention that may in any way be related thereto.

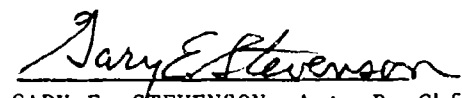
This report is releasable to the National Technical Information Service (NTIS). At NTIS, it will be available to the general public, including foreign nations.

This technical report has been reviewed and is approved for publication.


PATRICIA L. STUMPF
Project Engineer
Materials Integrity Branch


RONALD H. WILLIAMS
Technical Manager
Structural and Electronic
Failure Analysis

FOR THE COMMANDER


GARY E. STEVENSON, Actg Br Chf
Materials Integrity Branch
Systems Support Division

If your address has changed, if you wish to be removed from our mailing list, or if the addressee is no longer employed by your organization please notify WL/MLSA, WPAFB, OH 45433-6533 to help us maintain a current mailing list.

Copies of this report should not be returned unless return is required by security considerations, contractual obligations, or notice on a specific document.

REPORT DOCUMENTATION PAGE			Form Approved OMB No. 0704-0188	
<small>Public reporting burden for this collection of information is estimated to average 1 hour per response, including the time for reviewing instructions, searching existing data sources, gathering and maintaining the data needed, and completing and reviewing the collection of information. Send comments regarding this burden estimate or any other aspect of this collection of information, including suggestions for reducing this burden, to Washington Headquarters Services, Directorate for Information Operations and Reports, 1215 Jefferson Davis Highway, Suite 1204, Arlington, VA 22202-4302, and to the Office of Management and Budget, Paperwork Reduction Project (0704-0188), Washington, DC 20503</small>				
1. AGENCY USE ONLY (Leave blank)		2. REPORT DATE February 1992	3. REPORT TYPE AND DATES COVERED Final for 1 Jan 1987 to 31 Oct 1990	
4. TITLE AND SUBTITLE Composite Failure Analysis Handbook Volume II: Technical Handbook Part 3 - Case Histories			5. FUNDING NUMBERS Contract Number F33615-87-C-5212	
6. AUTHOR(S) R.J. Kar				
7. PERFORMING ORGANIZATION NAME(S) AND ADDRESS(ES) Northrop Corporation Aircraft Division One Northrop Avenue Hawthorne, California 90250-3277			8. PERFORMING ORGANIZATION REPORT NUMBER	
9. SPONSORING/MONITORING AGENCY NAME(S) AND ADDRESS(ES) Wright Laboratory (WL/MLSA) Materials Directorate Wright-Patterson AFB, Ohio 45433-6533			10. SPONSORING/MONITORING AGENCY REPORT NUMBER WL-TR-91-4032, DCT/FAA/CT-91-23 Volume II - Part 3	
11. SUPPLEMENTARY NOTES Additional Funding/Sponsorship Provided By: FEDERAL AVIATION ADMINISTRATION TECHNICAL CENTER U. S. DEPARTMENT OF TRANSPORTATION ATLANTIC CITY, NEW JERSEY 08405				
12a. DISTRIBUTION/AVAILABILITY STATEMENT Approved for public release; distribution is unlimited			12b. DISTRIBUTION CODE	
13. ABSTRACT (Maximum 200 words) The objective of this program was to create a comprehensive handbook for use in conducting failure analysis investigations on failed composite structure. This program builds upon previous efforts as documented in the "Compendium of Post-Failure Analysis Techniques for Composite Materials," AFWAL-TR-86-4137. The purpose of creating this handbook was to document the techniques, the fractographic and material property data and case history studies currently being utilized in the analysis of failed composite structure. The major tasks on this program included: (1) procedural guidelines for field investigation techniques; (2) an expanded fractographic data base for carbon/epoxy materials tested under known conditions, (3) a fractographic data base for resin based composite materials other than carbon/epoxy; (4) fractographic documentation of composite material and processing defects; (5) documentation of fracture characteristics in adhesive and mechanical joint failures; (6) compilation of material property data for composite materials; and (7) documentation of case histories recently conducted on failed composite structure.				
14. SUBJECT TERMS Composites; Composite Structures; Failure Analysis; Fractography; Adhesive Joints; Mechanical Joints; Case History Studies			15. NUMBER OF PAGES 125	
			16. PRICE CODE	
17. SECURITY CLASSIFICATION OF REPORT UNCLASSIFIED	18. SECURITY CLASSIFICATION OF THIS PAGE UNCLASSIFIED	19. SECURITY CLASSIFICATION OF ABSTRACT UNCLASSIFIED	20. LIMITATION OF ABSTRACT	

SUMMARY

The objective of this program was to develop a comprehensive handbook for failure analyses of fiber-reinforced composites. The program objectives were accomplished through technical tasks that resulted in the compilation of a reference manual for evaluating failed composite structures.

A field handling logic network was prepared for on-site handling of composites during accident investigations. Procedural guidelines were developed from inputs provided by key field personnel from several government agencies, and from the results of tests performed in-house at Northrop. Several current and new fractographic techniques were evaluated to identify methods for initiation site determination and failure sequence identification in failed composite specimens. Macrophotography, ply-sectioning, and photographic methods were determined to be valuable supplemental techniques but could not directly provide initiation site/fracture propagation direction when used alone. The microchemical analysis technique of Fourier Transform Infrared Spectroscopy was determined to be useful in contaminant failure investigations but will require development of a database of chemical "signatures."

Northrop expanded the fractographic database originally developed by the Boeing Company for AS4/3501-6 graphite/epoxy (Gr/Ep) under Air Force Contract No. F33615-84-C-5010 to include the effects of load, manufacturing, processing, and environmental variables on simple interlaminar and translaminar test coupons. It was determined that applied load was the principal parameter that altered the fracture surface characteristics in Gr/Ep. Material form and processing variables indirectly affected the fracture characteristics in that these caused localized variations in applied load, thereby altering fractographic features. No significant effects of environment on fracture surface features were determined. The fractographic database also included documentation of manufacturing and processing defects that occur in Gr/Ep. The flaws were characterized using optical microscopy, and macrophotography techniques.

Failure modes in adhesively bonded Gr/Ep and graphite/bismaleimide (Gr/BMI) specimens were also characterized. Variations in ply thickness, orientation, and loading were carried out to develop mixed cohesive-adhesive, and singular cohesive or adhesive failures. It was determined that specimen geometry, lap/strap ratios, and test load played roles in controlling fracture surface characteristics. Fracture characteristics in the failed adherends served as indicators of fracture direction in mixed and total adhesive failure modes. The crack directions could not be readily determined in pure cohesive joint failures.

A test matrix was developed for characterizing the six different failure modes in mechanically joined composite structures. A computer code entitled SAMCJ (Strength Analysis of Multifastened Composite Joints), previously developed by Northrop for the USAF was run to develop the matrix for quasi-isotropic AS4/3501-6 Gr/Ep joined with titanium "Hi-Lok" tension or

shear-type flush head fasteners. Failure tests and fractographic evaluation were carried out on the specimens. It was determined that the failure modes were a function of applied load, specimen, and fastener geometries.

Detailed in-plane shear tests were also carried out for Gr/Ep. This failure mode was characterized by the occurrence of hackles on fractured resin and tension fracture characteristics on fractured fiber ends. Processing variables did not significantly alter the fracture surface characteristics for Gr/Ep tested under in-plane shear. The information gained from the Northrop and Boeing Gr/Ep studies was used in initiating a fractographic database for other material systems. The material systems chosen were kevlar 49/3501-6 epoxy (K/Ep), AS4 graphite/5250-3 bismaleimide (Gr/BMI), and AS4 graphite/APC-2 PEEK thermoplastic (Gr/PEEK). Testing and fractographic evaluation were carried out for baseline and several variable conditions. The results for these systems indicated that the type of resin and fiber played strong roles in controlling the resulting fracture surface characteristics. As for Gr/Ep, environment and processing variables did not significantly alter fracture characteristics.

Northrop reviewed formats previously used for reporting metallic and composite fractography and failure analysis data. Based on an assessment of existing report schemes, Northrop proposed three data formats for 1) reporting fractographic data, 2) failure analysis information, and 3) organization of the Composite Failure Analysis Handbook. These were subsequently approved by the Air Force with minor modifications.

Northrop compiled material properties on current and near-term composite structural materials. Literature searches were carried out on government and commercial databases for product information and properties. Properties obtained were incorporated into database files using a personal computer. The data were organized into tabular formats for reporting in the Handbook. The properties for several classes of fiber, prepreg, and laminates were compiled and organized into the Handbook.

Under an engineering services agreement between Northrop and the University of Utah, Professor Willard Bascom of the University of Utah performed a literature search and made on-site visits to several government agencies to gather information on composite fractography and failure analysis that may have been performed at these agencies. No other information was found other than that previously reported by Boeing. Dr. Bascom also reviewed stress analysis methods and failure micromechanisms for use in failure analysis investigations. A new failure criterion developed by Dr. Richard Christensen of Lawrence Livermore Laboratories was determined to be of utility in composite failure investigations.

Verification of the composite failure analysis logic system was performed through evaluation of several failed structural items provided by the Air Force. The structural items represented "real-world" configurations and included 1) a vertical stabilizer, 2) a horizontal torque box assembly, 3) a canopy support fitting, and 4) two simple components. All the results are presented as case histories in the Handbook.

As part of the verification process, two simple Gr/Ep structures containing intentional defects were fabricated and tested to failure under controlled laboratory conditions. The failed

specimens and related test documentation were shipped to the Air Force for subsequent evaluation by the Boeing Company.

The Composite Failure Analysis Handbook is divided into two volumes. Volume I is the Program Overview. Volume II comprises the Technical Handbook, and is divided into three parts. Part 1 describes all the techniques and procedures for performing composite failure analysis. Part 2 represents an atlas of fractographs. Part 3 is a compilation of case histories of investigations performed by Northrop, Boeing, and General Electric.

In summary, Northrop has achieved the objective of producing a Handbook containing all the known techniques, procedures, sample data, and reference supporting data for performing post-failure analysis of fiber-reinforced composite structures.



Accession For	
NTIS GRA&I	<input checked="checked" type="checkbox"/>
DTIC TAB	<input type="checkbox"/>
Unannounced	<input type="checkbox"/>
Justification	
By	
Distribution/	
Availability Codes	
Dist	Avail and/or Special
A-1	

FOREWORD

The final report documents work performed under Contract F33615-87-C-5212 from January, 1987 through October, 1990 by the Northrop Corporation, Aircraft Division, Hawthorne, California for the United States Air Force Systems Command. The program was administered under the technical direction of Ms Patricia Stumpff, Materials Directorate, Wright Laboratory, Wright-Patterson Air Force Base, Ohio 45433-6533. The majority of funding for this program was provided by the Federal Aviation Administration Technical Center, Aviation Safety Division, Atlantic City, New Jersey 08405. Mr Lawrence Neri, ACD-210, acted as the Federal Aviation Administration technical manager. Mr Joseph Soderquist, National Resource Specialist, Advanced Materials, Federal Aviation Administration, AIR-103, 800 Independence Avenue, S.W., Washington, D. C. 20591, also provided technical direction for this program.

The work was performed by Northrop's Materials Analysis Laboratory. Dr R. J. Kar was the Program Manager and Principal Investigator. The contributions of the following members of the Materials Analysis Laboratory are gratefully acknowledged: Ms L. M. Concepcion (Co-Principal Investigator), Mr O. P. DeCastro (SEM and materialography), Mr J. M. Dobson (case histories), Mr T. N. Gindraux (materialography and SEM) Mr L. J. Havemann (SEM), Mr M. D. Ensminger (FTIR), Mr L. S. Dhillon (materialography) and Mr E. E. Ramirez (materialography). Mr P. J. Dager of Northrop's Mechanical Testing Laboratory and Mr R. J. Isberner of Northrop's Structures Test Laboratory performed the mechanical testing of laminate coupons and real-world elements. Mr R. B. Deo, and Mr T. A. Dyer of Northrop's Structures Research Department participated in the selection of test laminates.

Professor W. D. Bascom, Department of Materials Science and Engineering at the University of Utah, also made significant contributions by conduction of literature survey on composite fractography and identifying new composite failure criteria.

The results of additional work in composites failure analysis by the Boeing Military Airplane Company under Air Force Contracts F33615-84-C-5010 and F33615-86-C-5071 from 1984 through 1988 have been included in this report for the purpose of providing the most complete Composite Failure Analysis Handbook. Mr R. A. Grove, Mr B. W. Smith, and Ms C. T. Hua were Principal Investigators, and Mr D. F. Sekits was the Program Manager of these programs. The author wishes to thank Boeing and the numerous publishing houses and authors who granted permission to include their works in this document.

TABLE OF CONTENTS

Section	Page
1 INTRODUCTION AND PURPOSE	1-1
2 CASE HISTORIES	2-1
2.1 FAILURE ANALYSIS OF A 737-300 ELEVATOR TEST BOX.....	2-1
2.1.1 Background History	2-1
2.1.2 Nondestructive Examination	2-2
2.1.3 Materials Characterization	2-2
2.1.4 Fractography	2-2
2.1.5 Stress Analyses	2-4
2.2 FAILURE ANALYSIS OF A J VX-22 OSPREY FULL SCALE WING TEST BOX.....	2-4
2.2.1 Background History	2-4
2.2.2 Nondestructive Evaluation	2-4
2.2.3 Materials Characterization	2-10
2.2.4 Fractography	2-10
2.2.5 Stress Analysis	2-12
2.3 FAILURE ANALYSIS OF THE NASA HIMAT WING.....	2-13
2.3.1 Background History	2-13
2.3.2 Nondestructive Evaluation	2-13
2.3.3 Materials Characterization	2-17
2.3.4 Fractography	2-17
2.3.5 Stress Analysis	2-22
2.4 FAILURE ANALYSIS OF A CARBON FIBER REINFORCED PLASTIC I-BEAM	2-22
2.4.1 Background History	2-22

TABLE OF CONTENTS (Continued)

Section	Page
2.4.2 Nondestructive Evaluation	2-23
2.4.3 Materials Characterization	2-23
2.4.4 Fractography	2-23
2.4.5 Stress Analysis	2-25
2.5 FAILURE ANALYSIS OF A BALLISTICALLY DAMAGED COMPOSITE TEST PANEL	2-28
2.5.1 Background History	2-28
2.5.2 Visual Examination	2-28
2.5.3 Nondestructive Evaluation	2-35
2.5.4 Materials Characterization	2-35
2.5.5 Fractography	2-39
2.5.6 Stress Analysis	2-40
2.5.7 Summary	2-40
2.5.8 Conclusions/Recommendations	2-40
2.6 FAILURE ANALYSIS OF A MAIN LANDING GEAR STRUT	2-42
2.6.1 Background History	2-42
2.6.2 Visual Examination	2-42
2.6.3 Nondestructive Evaluation	2-42
2.6.4 Material Characterization	2-48
2.6.5 Fractography	2-48
2.6.6 Stress Analysis	2-48
2.6.7 Conclusion/Recommendation	2-48
2.7 FAILURE ANALYSIS OF A VERTICAL RUDDER	2-56
2.7.1 Abstract	2-56
2.7.2 Background	2-56

TABLE OF CONTENTS (Continued)

Section	Page
2.7.3 Analysis of Failure	2-56
2.7.3.1 Visual Examination	2-56
2.7.3.2 Ultrasonic Testing of Rudder Assembly	2-57
2.7.3.3 Fractographic Examination	2-61
2.7.3.4 X-ray Tests	2-61
2.7.3.5 Microstructure	2-61
2.7.4 Summary	2-61
2.8 FAILURE ANALYSIS OF A HORIZONTAL STABILIZER TORQUE BOX ASSEMBLY	2-66
2.8.1 Abstract	2-66
2.8.2 Background	2-66
2.8.3 Analysis of Failure	2-66
2.8.3.1 Visual Examination	2-66
2.8.3.2 Ultrasonic Testing of Stabilizer Assembly	2-66
2.8.3.3 Fractographic Examination	2-67
2.8.3.4 Microstructure/Material Tests	2-72
2.8.4 Summary	2-72
2.9 FAILURE ANALYSIS OF A CYLINDRICAL SPECIMEN	2-72
2.9.1 Abstract	2-72
2.9.2 Background	2-76
2.9.3 Analysis of Failure	2-76
2.9.3.1 Visual Examination	2-76
2.9.3.2 NDE Tests	2-76
2.9.3.3 Fractographic Examination	2-79
2.9.3.4 Material Tests	2-84

TABLE OF CONTENTS (Continued)

Section	Page
2.9.3.5 Stress Analysis	2-84
2.9.4 Summary	2-84
2.10 FAILURE ANALYSIS OF A COMPOUND PLATE AND FASTENER ASSEMBLY	2-84
2.10.1 Abstract	2-84
2.10.2 Background	2-84
2.10.3 Analysis of Failure	2-84
2.10.3.1 Visual Examination	2-86
2.10.3.2 NDE Tests	2-86
2.10.3.3 Fractographic Examination	2-86
2.10.3.4 Stress Analysis	2-93
2.10.4 Summary	2-93
2.11 FAILURE ANALYSIS OF A COMPOSITE ARCH REINFORCEMENT	2-93
2.11.1 Abstract	2-93
2.11.2 Background	2-95
2.11.3 Analysis of Failure	2-95
2.11.3.1 Visual Examination	2-95
2.11.3.2 NDE Testing of Component	2-95
2.11.3.3 Fractographic Examination	2-95
2.11.3.4 Microstructure/Material Tests	2-99
2.11.3.5 Stress Analysis	2-99
2.11.4 Summary	2-105
2.12 EDITORIAL NOTES	2-105
2.12.1 Ballistically Damaged Composite Test Panel	2-105

Table of Contents (Concluded)

Section	Page
2.12.2 Main Landing Gear Strut	2-107
2.12.3 Compound Plate and Fastener Assembly	2-107

LIST OF FIGURES

Figure		Page
2-1	737-300 Elevator Static Test Evaluation	2-1
2-2	737-300 Elevator Static Test Fracture Directions	2-3
2-3	Central Portion of JVX V-22 Central Wing Test Box	2-5
2-4a	JVX Wing Test Box Upper Skin Surface	2-6
2-4b	JVX Wing Test Box Inner Side of Upper Skin	2-7
2-5	JVX Wing Test Box Front and Rear Spars	2-8
2-6	JVX Wing Test Box Lower Skin Surface	2-9
2-7	Ultrasonic C-Scan of Upper Skin Surface	2-11
2-8	JVX Wing Test Box Crack Mapping Results	2-12
2-9	NASA HiMAT Test Wing in the As-Received Condition	2-14
2-10	Upper Skin Inboard Edge Damage	2-15
2-11	NDE Results of the Lower Surface	2-16
2-12	NDE Results of the Upper Surface	2-16
2-13	Fiber Identification by Surface Analysis	2-18
2-14	Photomicrograph of Zone B Cross Section	2-19
2-15	Cross Section Illustrating Boron Fiber Misalignment Resulting in Resin-Rich Adjacent Regions	2-19
2-16	Photomicrograph of Beach Marks Indicative of Cyclic Crack Growth and Crack Propagation Direction	2-20
2-17	Crack Mapping Results From Selected Delamination Regions	2-21
2-18	CFRP I-Beam in the As-Received Condition	2-22
2-19	Regions of (a) Compression Buckling and (b) Delamination in the Upper Cap Section of the I-Beam	2-24
2-20	Regions of (a) Compression Buckling and (b) Delamination in the Upper Cap Section of the I-Beam	2-25
2-21	ITU C-Scans of the I-Beam Subcomponents	2-26

LIST OF FIGURES (Continued)

Figure		Page
2-22	Extensive Porosity and Laminate Deformity in the Web-to-Cap Junction	2-27
2-23	Results of Fractographic Crack Mapping of an Upper Cap Delamination	2-27
2-24	Photomacrographs of the Component As-Received	2-29
2-25	Apparent Impact Damage	2-30
2-26	Damage in Fastener Hole Loaded Under Shear	2-31
2-27	Damage in the Fastener Hole Loaded Under Tension	3-32
2-28	Mapping of the Fastener Hole Damage	2-33
2-29	Difference in Fastener Fit in the Undamaged Fastener Hole	2-33
2-30	Macrophotographs Showing the Fit of the Fastener in the Damaged Holes	2-34
2-31	Through Transmission Ultrasonic (TTU) Scan of Component	2-35
2-32	Infrared Spectroscopy Result	2-36
2-33	DSC Thermogram	2-37
2-34	TMA Thermograms Showing an Average Glass Transition Temperature of 210° C	2-38
2-35	TGA Thermogram	2-39
2-36	Wavelength Dispersive X-Ray (WDX) Scan of the Fiber	2-40
2-37	Cross-Sectional View of the Panel	2-41
2-38	Macrophotograph of the Upper Surface of the Landing Strut As-Received	2-43
2-39	Macrophotograph of the Translaminar Fracture Surface on the Small (Fixed Piece) of the Strut	2-44
2-40	Macrophotographs of the Top of the Small Piece Fracture Surface Showing Delamination, Upper Surface, Tension Fracture (T) and Compression Fracture (C)	2-45
2-41	Macrophotograph of the Lower Surface of the Strut As-Received	2-46
2-42	Macrophotographs of Side of Strut Showing Delaminations.	2-47
2-43	TMA and DSC Thermograms of Strut	2-49

LIST OF FIGURES (Continued)

Figure		Page
2-44	Macrophotographs of the Lower Surface of Strut	2-50
2-45	Macrophotograph (A) and Photomicrograph(B) of Section X-X Taken Through the Bolt Hole and End	2-51
2-46	SEM Fractographs of Delamination at the Translaminar Fracture Surface of the Small Piece	2-52
2-47	SEM Fractographs of Delamination Adjacent to Translaminar Fracture.....	2-53
2-48	SEM Fractographs of the Tensile Half of the Translaminar Fracture Surface	2-54
2-49	SEM Fractographs of the Compressive Half of the Translaminar Fracture	2-55
2-50	FALN Sequence Used in Investigation of Rudder Failure	2-57
2-51	As-Received Photographs of Rudder	2-58
2-52	Composite TTU Plot of Rudder.....	2-59
2-53	B-Scan of Repair Region on Inboard Skin	2-59
2-54	Pulse-Echo Images of Damaged Region	2-60
2-55	Macrophotographs of Delamination Fracture in Coupon From Damaged Area	2-62
2-56	SEM Photographs of Delaminated Surface.....	2-63
2-57	SEM Photographs Showing Fracture Details in Delamination	2-64
2-58	X-Ray Radiograph Shows Blown -Core in Rudder	2-65
2-59	Photograph of Cross-Section Taken Through Rudder Skin	2-65
2-60	FALN Sequence Used to Evaluate Horizontal Stabilizer Torque Box Assembly Failure	2-67
2-61	As-Received Photographs of Horizontal Stabilizers	2-68
2-62	TTU C-Scans of Horizontal Stabilizer	2-69
2-63	Pulse-Echo Images of Damage at the Outboard End of the Stabilizer (Zone A) ...	2-70
2-64	Pulse-Echo Images of Damage at the Mid-Section of the Stabilizer (Zone B).....	2-71
2-65	Evaluation of Skin Damage in Zone A After Ply Removal	2-73

LIST OF FIGURES (Continued)

Figure		Page
2-66	SEM Photographs of Delamination in Zone A (Top Layer Removed)	2-74
2-67	SEM Photographs of Delamination in Zone A (Second Layer Removed)	2-75
2-68	Macrograph of Zone B Damage With Top Layer Removed	2-76
2-69	SEM Photographs of Zone B Delamination (Top Layer Removed)	2-77
2-70	As-Received Documentation of Failed Cylindrical Specimen	2-78
2-71	Photograph of Cylindrical Specimen After Sectioning to Expose Internal Damage	2-79
2-72	Photographs Showing Damage in Fragment B of Cylinder	2-80
2-73	SEM Photographs of Damage on Outer Surface of Cylinder	2-81
2-74	SEM Photographs of Outer Surface Damage With Clusters of Fibrils Removed ..	2-82
2-75	SEM Photographs of Damage on Inner Surface of Cylinder	2-83
2-76	Optical Photomicrographs of Cross-Section Taken Through Defects in Cylinder.	2-85
2-77	As-Received Documentation of Compound Plate and Fastener Assembly	2-87
2-78	SEM Photographs in Region A of Delamination of Bottom Surface of Compound Plate	2-89
2-79	SEM Photographs in Region B of Delamination of Bottom Surface of Compound Plate	2-90
2-80	SEM Photographs in Region C (Honeycomb Region) of Delamination of Bottom Surface of Compound Plate	2-91
2-81	SEM Photographs of Bolt Hole Cross-Section in Bottom Surface of Compound Plate (Region D)	2-92
2-82	Delamination in Top Surface of Compound Plate (Mating Halves)	2-93
2-83	Optical and SEM Photographs of Delaminated Fragment of Top Surface of Compound Plate	2-94
2-84	As-Received Documentation of Composite Arch Reinforcement	2-96
2-85	Documentation of Cracks in Part	2-97
2-86	Documentation of Ply Removal and Sectioning	2-98

LIST OF FIGURES (Concluded)

Figure		Page
2-87	Optical and SEM Photographs of Shear Fracture at Fastener Hole	2-100
2-88	SEM Characterization of Fastener Hole Crack in Bow	2-101
2-89	Characterization of Sheath Surface	2-102
2-90	Evaluation of Bow Surface	2-103
2-91	SEM Characterization of Bow Delamination	2-104
2-92	Macrograph of Cross-Section Taken Through Fastener Hole	2-105
2-93	Optical Photomicrographs of Cross-Section Through Fastener Hole	2-106

LIST OF TABLES

Table		Page
2-1	Fractography Results From NASA HiMAT Wing	2-20
2-2	Resin Content Determined By Acid Digestion	2-39

SECTION 1
INTRODUCTION AND PURPOSE

SECTION 1

INTRODUCTION AND PURPOSE

Advanced composites are rapidly emerging as a primary material for use in near-term and next-generation aircraft as they provide greater structural efficiency at lower weight than equivalent metallic components. Based on trends to date, the next generation of military aircraft could contain as much as 65 percent of their structural weight in advanced composite materials.

As composite materials continue to be developed and incorporated into airframe structures, needs have arisen for solving problems associated with their use. Composite structures can and will prematurely fail due to gross manufacturing defects, design errors or severe in-service damage. Needs exist for a systematic compilation of failure analysis techniques, procedures, and supporting fractographic data, in a handbook form that can be used by experienced laboratory personnel, working in consultation with field investigators, to diagnose the cause for premature component failure and to make recommendations for preventing similar failures.

The goal of this Composite Failure Analysis Handbook is to provide a guide for conducting post-failure analysis of fiber-reinforced composite structures. It forms a compilation of the procedures, techniques, and sample data required to conduct analyses of composite structures. Volume II of this report is the Technical Handbook and it has been divided into three parts.

Part 3 of the Handbook consists of a compilation of case histories of work performed by Northrop under Air Force Contract F33615-87-C-5212, and by Boeing and General Electric under Air Force Contracts F33615-84-C-5010 and F33715-86-C-5071. The case histories performed by Boeing and General Electric were previously reported in AFWAL TR-86-4137 and WRDC-TR-89-4055.

The case histories presented in this part are intended to provide the investigator with a basic understanding of the overall post-failure analysis process, involving the three fundamental areas required to identify the sequence and cause of failure of the component. These fundamental areas are:

1. The use of the failure analysis logic networks (FALNs) which provide the guidelines delineating the logical sequence of investigative operations
2. The application of the analytical tools to best determine the physical characteristics present within the failed part
3. The interpretive methodology and decisions which provide the evidence and rationale to determine the causes, sequences, and contributory factors related to part failure (with the most direct, accurate, timely and cost-effective methods available).

The use of these fundamental and interdependent investigative methods are applied to each of the post-failure analyses presented in this part. These case histories provide a valuable reference source of several typical fracture analyses. Each example provides a basic illustration of the sequence, analytical tools, results, and decisions involved. The collection and review of background information, nondestructive evaluations, material characterizations, fractography and stress analysis all contributed to the determination of the cause of failure. Some of the case histories presented are test specimens which were fractured in the laboratory under known conditions and other case histories presented are actual aircraft components that failed during use or during repair for unknown reasons.

Parts 1 and 2 (the Procedures and Techniques and the Atlas of Fractographs, respectively) of the Technical Handbook are discussed in the Summary of this report. Further information has been presented in the Introduction and Purpose section of each of these section.

The Handbook has been designed to be a living document that can be updated readily. This work reports the results of six years of fundamental work that has been sponsored by the United States Air Force (USAF) and the Federal Aviation Administration (FAA).

SECTION 2
CASE HISTORIES

SECTION 2

CASE HISTORIES

2.1 FAILURE ANALYSIS OF A 737-300 ELEVATOR TEST BOX

Failure analysis of the elevator box was conducted by the Boeing Company.

2.1.1 Background History

Figure 2-1 illustrates a portion of a graphite/epoxy tapered box structure which fractured during test. This graphite/epoxy box consisted of two honeycomb skin panels fastened to a spanwise spar with intermediate chordwise ribs. A review of the test history revealed that premature fracture occurred during hingeline deflection of the front spar.

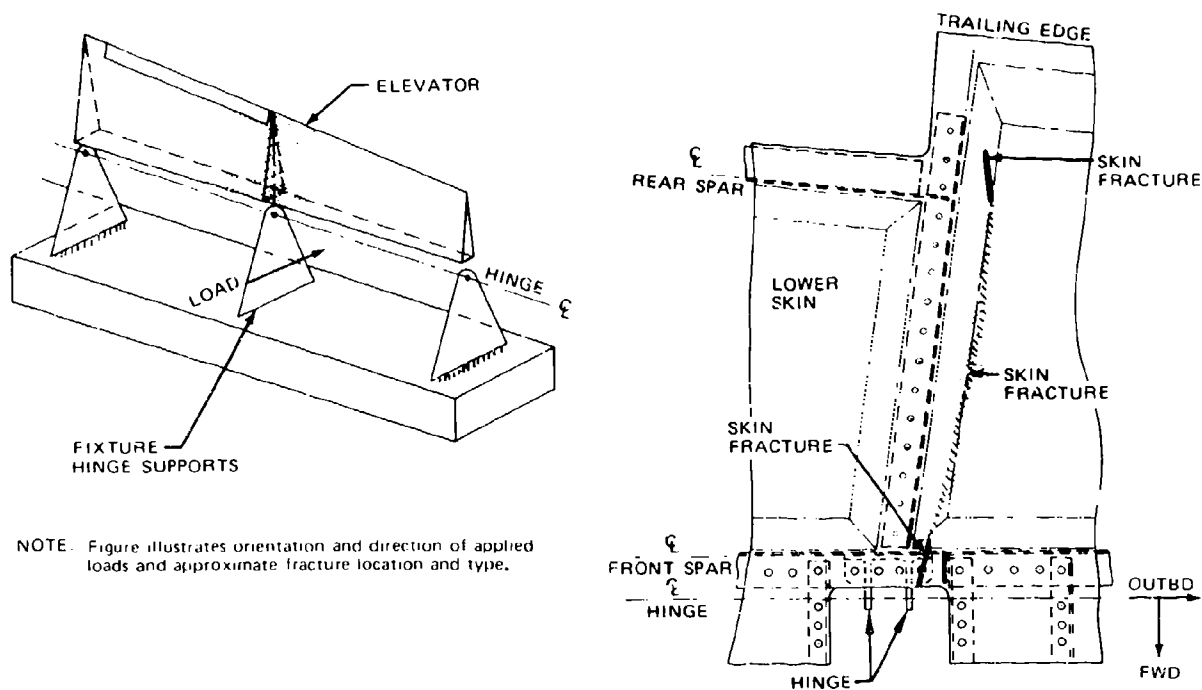


Figure 2-1. 737-300 Elevator Static Test Evaluation

2.1.2 Nondestructive Examination

Visual inspection of the fractured box revealed several through-thickness translaminar cracks in the forward and trailing edges of the compression loaded skin panel. Upon further examination, some localized buckling of the skin panel, indicative of interlaminar fracture, was evident between each of these translaminar fractures. A nondestructive evaluation was performed using C-scan through transmission ultrasonics (TTU) to define areas of nonvisible damage so the specimen could be removed for laboratory investigations without damaging evidence. The TTU scans were performed over the entire part, and revealed a roughly four inch wide band of delamination between the areas of through-thickness skin fracture at the front and rear spar. Since a honeycomb core was involved, X-ray inspections of the core damage to determine the extent of translaminar damage was performed. Although some core crushing had occurred in the immediate vicinity of the skin fracture, the core condition in the non-damaged area surrounding the fracture was found to be free of defects such as poor splicing or potting.

2.1.3 Materials Characterization

Following the definition of the type and extent of fracture, tests were performed to determine if any major material discrepancies existed in either fabrication or processing. Accordingly, sections of the skin, spar and rib panels were cut from nondamaged regions immediately adjacent to the fracture and were examined to verify the layup and determine the overall panel quality. In addition, thermomechanical analyses (TMAs) were performed to verify the extent of cure. Since Boeing uses both 250°F (121°C) and 350°F (177°C) curing prepregs, this analysis was also performed to confirm the specified use of the 350°F prepregs. Dimensions of skin panel, spar and rib details were also measured and checked against required dimensions and tolerances. For each of these analyses, all of the individual components of the elevator were found to be in proper compliance with the drawing, materials, and process specification requirements.

2.1.4 Fractography

Since no discrepancies were identified in the above analyses, fractographic examinations were selected as the next investigative operation. Primary emphasis was placed on identifying the direction of crack propagation, origin, and any anomalous conditions that could be associated with fracture. To help in the examination, the delaminated interlaminar areas were removed from the skin panel and sectioned into approximately 6 inch by 6 inch squares and examined optically. The optical examinations were performed at 400 to 600X magnification, which provided a rapid and efficient means of identifying characteristic fracture features. Scanning electron microscopy (SEM) was performed on selected areas of interest requiring higher magnifications and to document specific fracture features identified during the optical analyses. The orientation of river patterns and resin microflow (Figure 2-2) observed on the fracture surface were used to generate a map of the local directions of crack propagation over the fracture surface. Although some areas of interlaminar fracture separated by shear loading (as evidenced by the presence of hackles and scallops), a majority of the fracture exhibited Mode I tension river mark features. SEM analysis of the translaminar

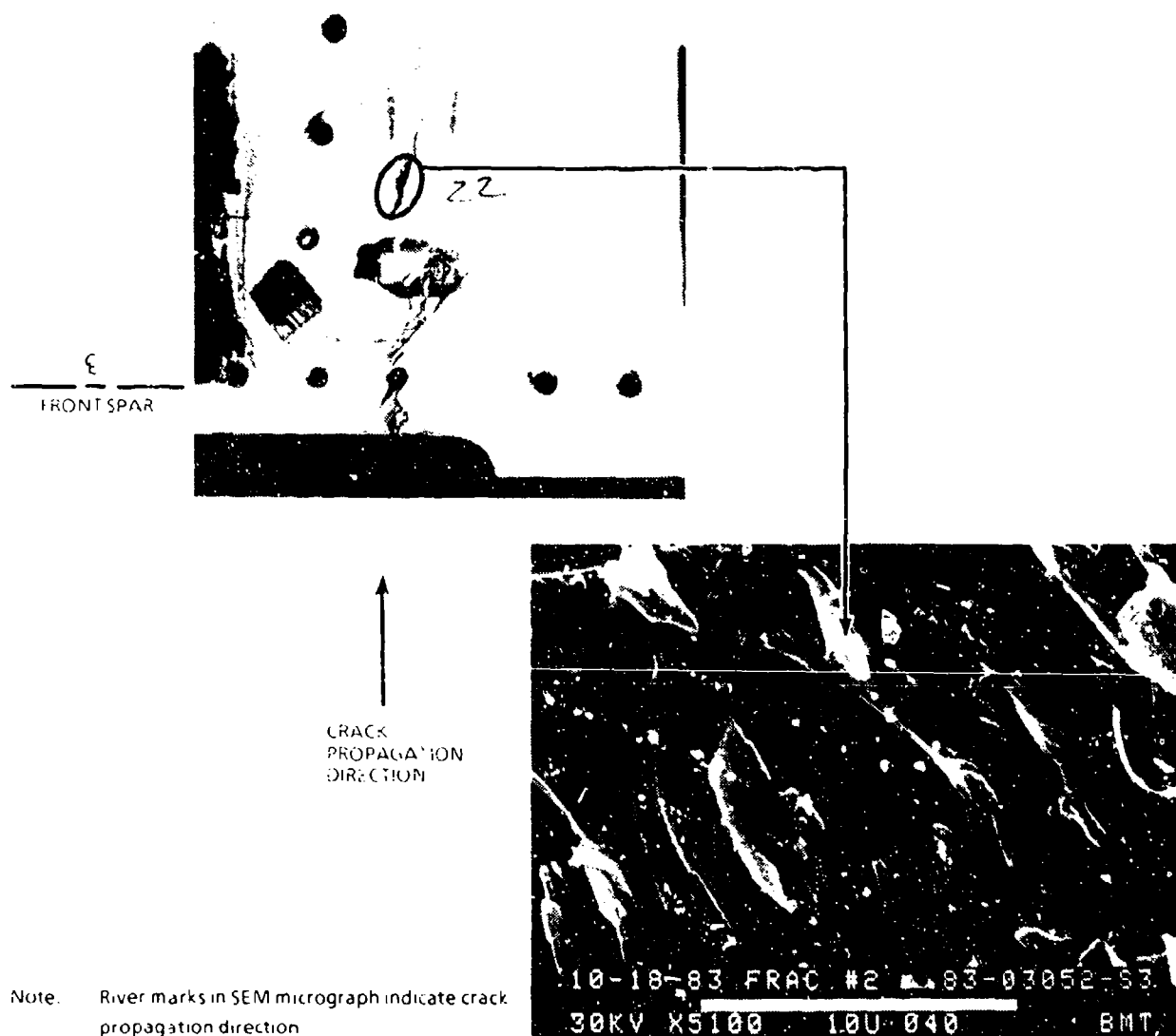


Figure 2-2. 737-300 Elevator Static Test Fracture Directions

fracture regions were not fruitful in positively identifying the direction of fracture, although the macroscopic and microscopic analyses indicated compressive buckling failure.

By reconstructing the fracture process through the interlaminar crack mapping process, it was discovered that crack initiation occurred at the periphery of a fastener hole located at the front spar. Subsequent propagation occurred in a chordwise direction across the compression loaded skin panel. See Figure 2-2 for the arrow across the skin panel illustrating the direction of the delamination process, particularly related to the fastener hole and the translaminar crack near the hole. No microscopic anomalies were identified at the origin region, and therefore no contamination analyses such as surface chemical tests were required.

2.1.5 Stress Analyses

Since no anomalies were identified at the origin area which might explain premature fracture, detailed stress analyses of this area were initiated. These analyses evaluated both the basic in-plane panel strains, as well as the buckling stability of the origin area since it was in compression during fracture. These investigations revealed that premature skin buckling occurred under compression loading due to a relatively large fastener spacing in this local area. As a result of these analyses, further attention was paid to this design detail and the fastener spacing was reduced to prevent the buckling mode that precipitated premature fracture.

2.2 FAILURE ANALYSIS OF A JVX-22 OSPREY FULL SCALE WING TEST BOX

Failure analysis of the wing box was conducted by the Boeing Company.

2.2.1 Background History

Analysis of the wing box was initiated after premature fracture had occurred during testing of the structure. Figure 2-3 illustrates the central portion of the forty five foot-long structure, immediately following fracture, with the cracking occurring in the center bay region. Discussions with the test and design engineers indicated that the loading conditions were applied to simulate upward and aft bending of the outboard ends of the box, so as to create a maximum compressive stress at the upper skin surface. The construction was found to be a stringer stiffened skin, with front and rear spars, and the ribs fabricated from graphite/epoxy tape. At this time, the manufacturing data regarding the specific materials, processes, and design (as well as the intended operational envelope) were collected.

2.2.2 Nondestructive Evaluation

Initial visual inspections of the damage region were carried out to identify the areas of visible fracture or deformation. As shown in Figure 2-4a, the upper skin surface exhibited a branching translaminar crack across the entire surface (severing all five stringers) and compression type translaminar fracture morphology for both the skin and stringers (as indicated by the flat fracture appearance). This macroscopic translaminar branching most likely indicated the gross overall fracture direction, such that the cracking progressed across the skin from the rear spar region in a chordwise direction toward the front spar. The translaminar cracking intersected the trailing edge of the skin at a radius for a runout of an overhanging tab. Extensive delamination was evident on each side of the translaminar cracking, often wedged open from mating fracture surface overrun during compression loading. Figure 2-4b presents the underside of the upper skin surface, at the trailing edge tab region, illustrating the type and extent of damage.

The front and rear spars, shown in Figure 2-5, were also cracked, each exhibiting vertical translaminar fractures that appeared to intersect the upper skin fracture. The spar webs were delaminated around the translaminar cracks, with extensive buckling indicative of a compressive load at failure.

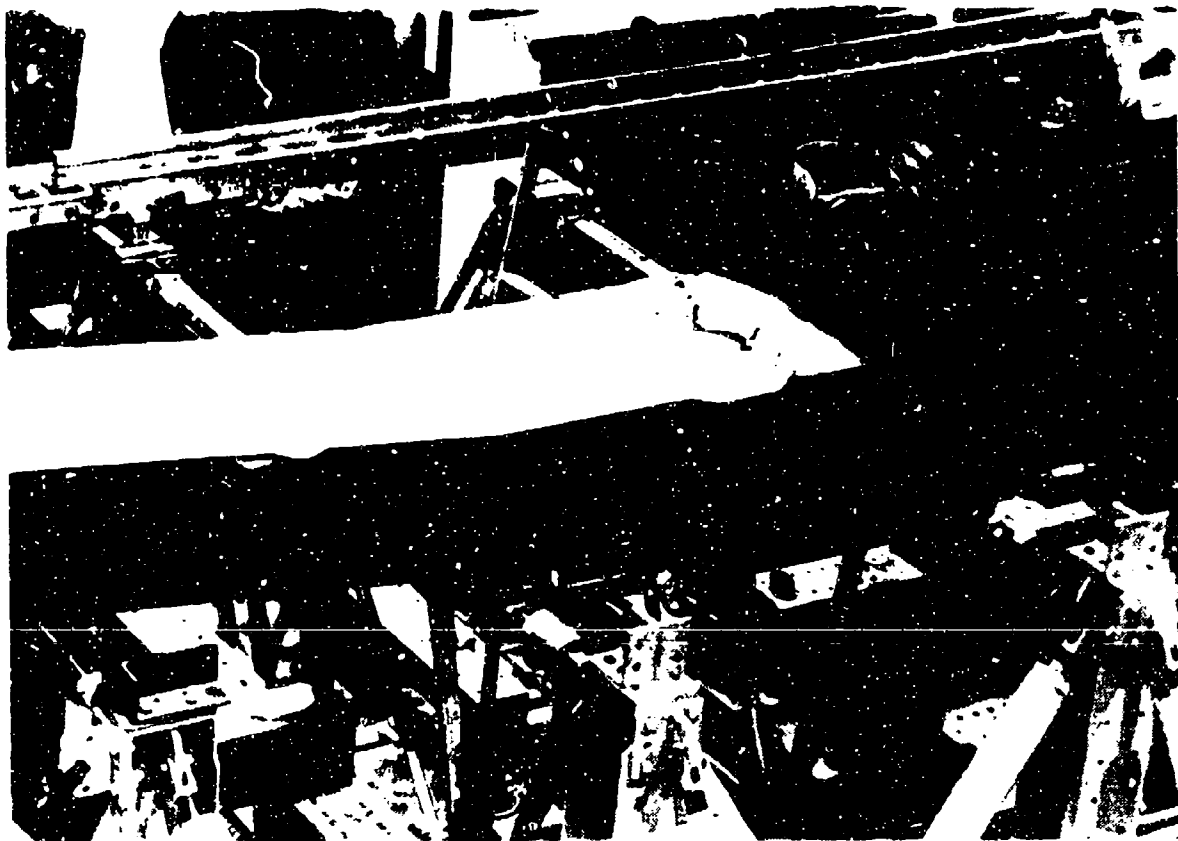
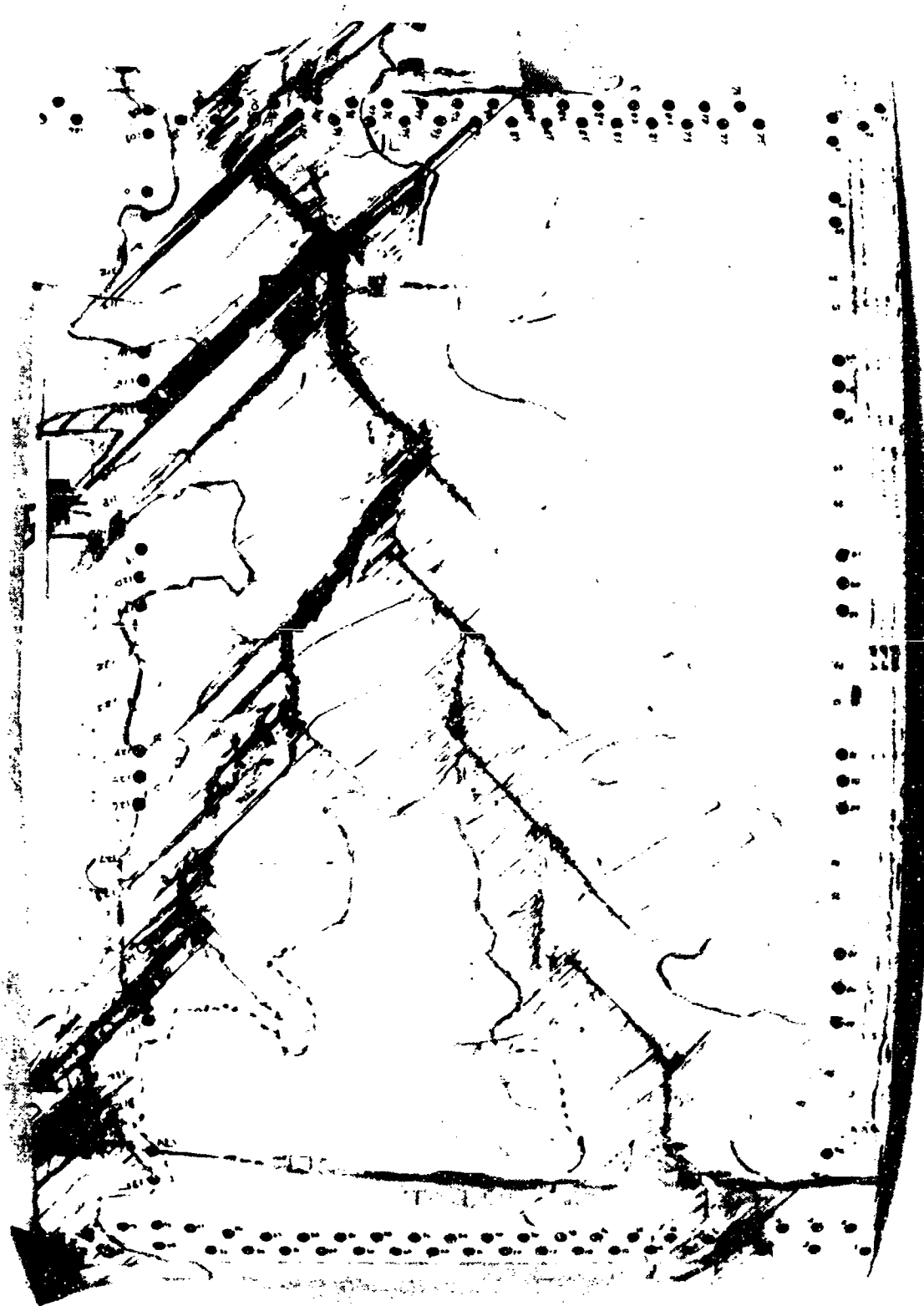


Figure 2-3. Central Portion of JVX V-22 Central Wing Test Box

The lower skin surface, shown in Figure 2-6, was damaged in a similar manner to the upper skin, although to a lesser extent. The skin buckling also indicated a compressive loading. Since the stress prior to fracture was supposed to be tensile, the neutral axis between tension and compression must have shifted to below the lower skin surface during the failure process. As a result of these visual observations, it appeared that damage in the upper skin and spars occurred prior to cracking in the lower skin.

Nondestructive examinations were then performed to determine the extent of nonvisible damage. While still intact as a complete structure, the entire wing box was subjected to hand-held pulse echo inspection. This allowed determination of the extent of delamination surrounding the translaminar fracture as well as checking the remaining structure for any other damage that may have either contributed to, or occurred during, the failure. The outline of the delaminations surrounding the translaminar fractures as indicated by pulse echo are visible in Figures 2-4, 2-5 and 2-6.



Trailing Edge

Figure 2-4a. J VX Wing Test Box Upper Skin Surface

Leading Edge

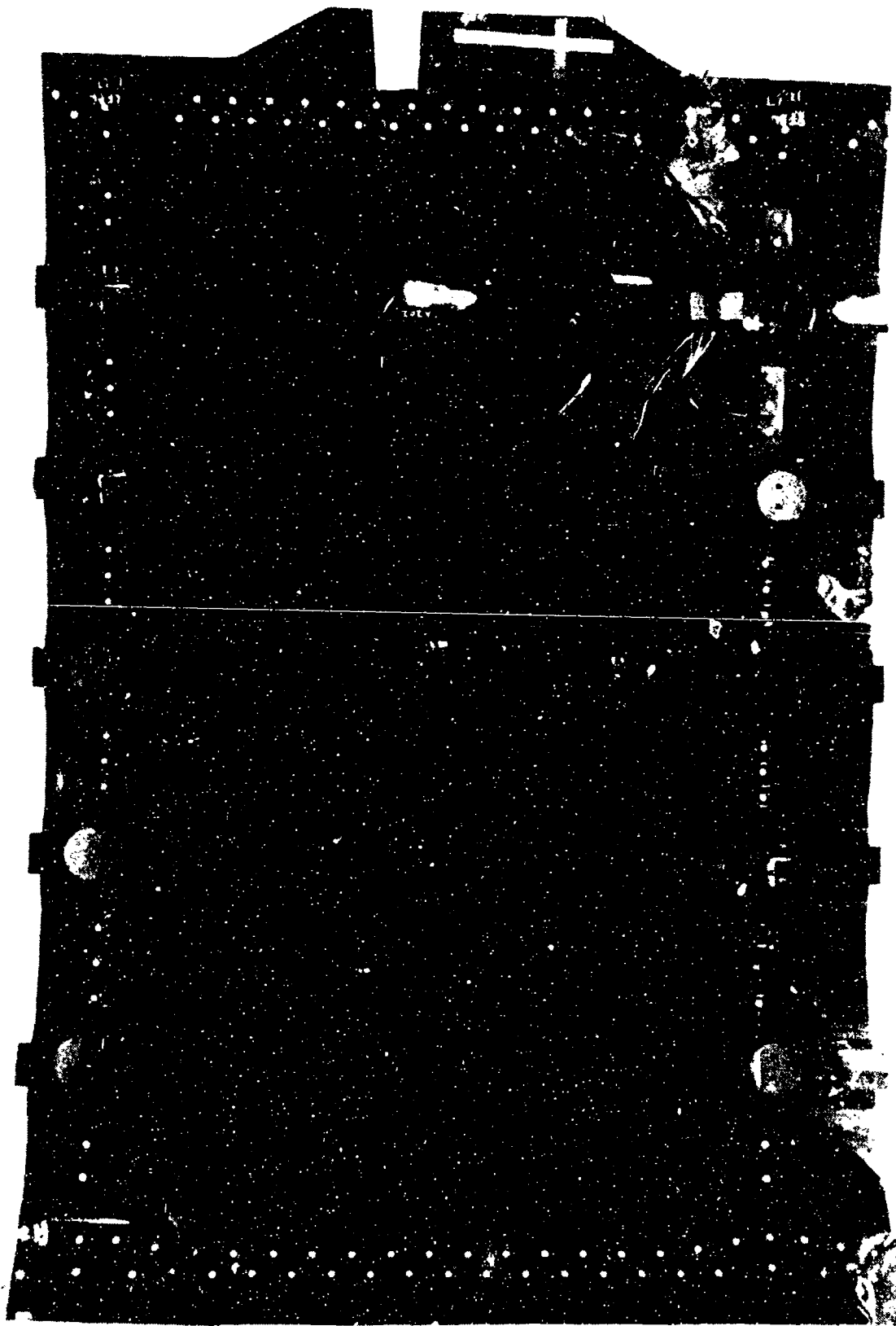
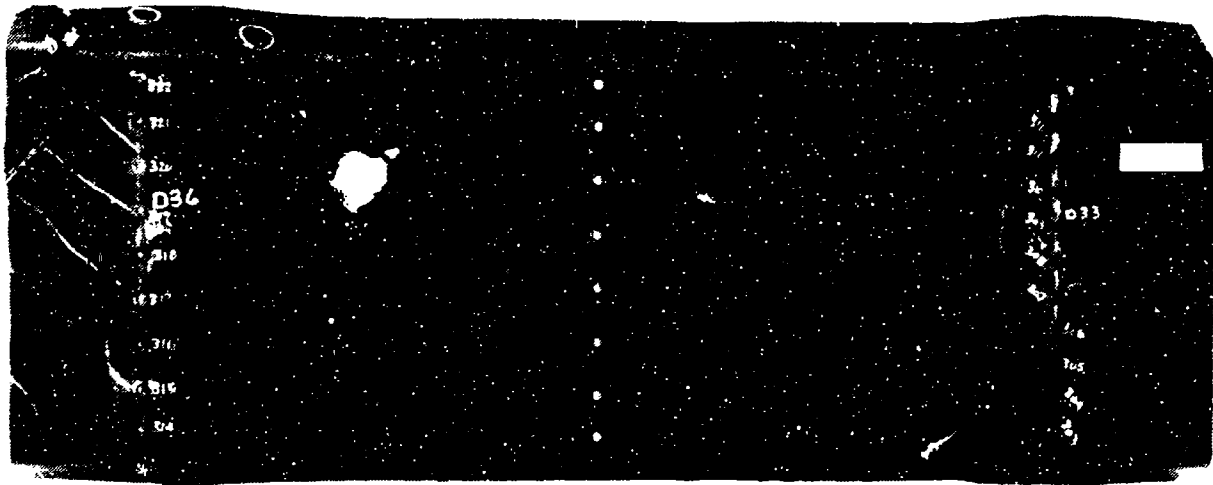
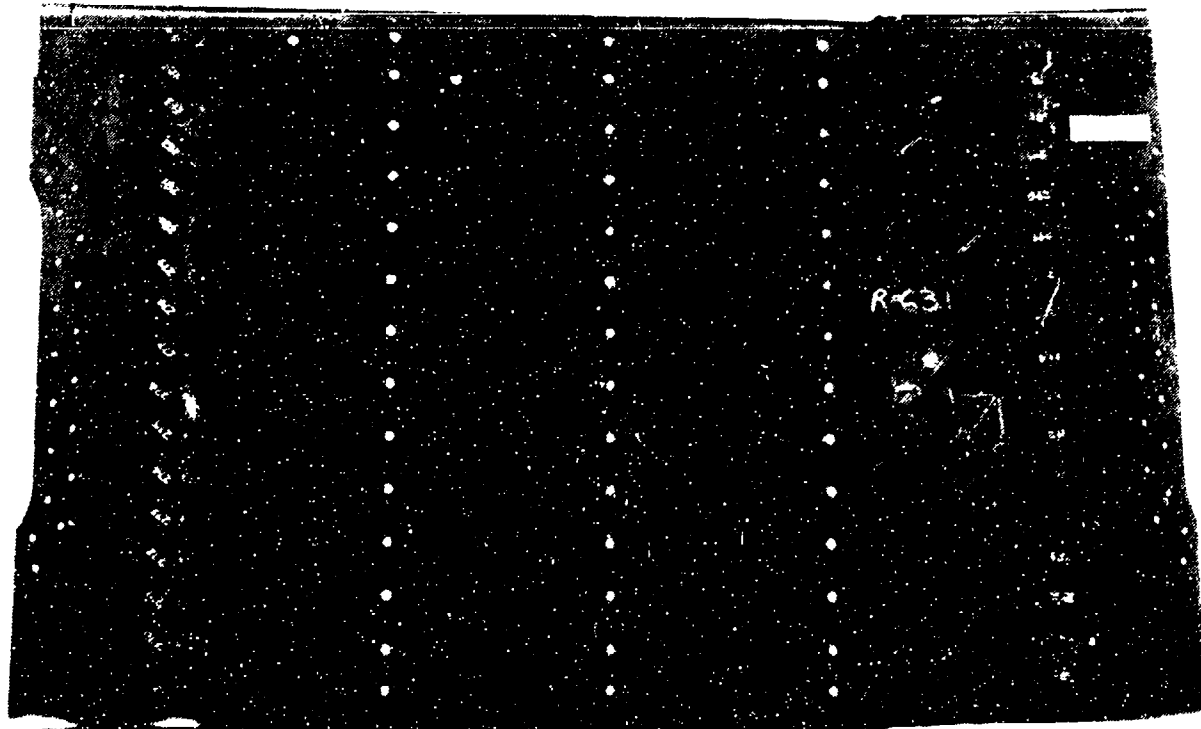


Figure 2-4b. JVX Wing Test Box Inner Side of Upper Skin



Front Spar



Rear Spar

Figure 2-5. JVX Wing Test Box Front and Rear Spars

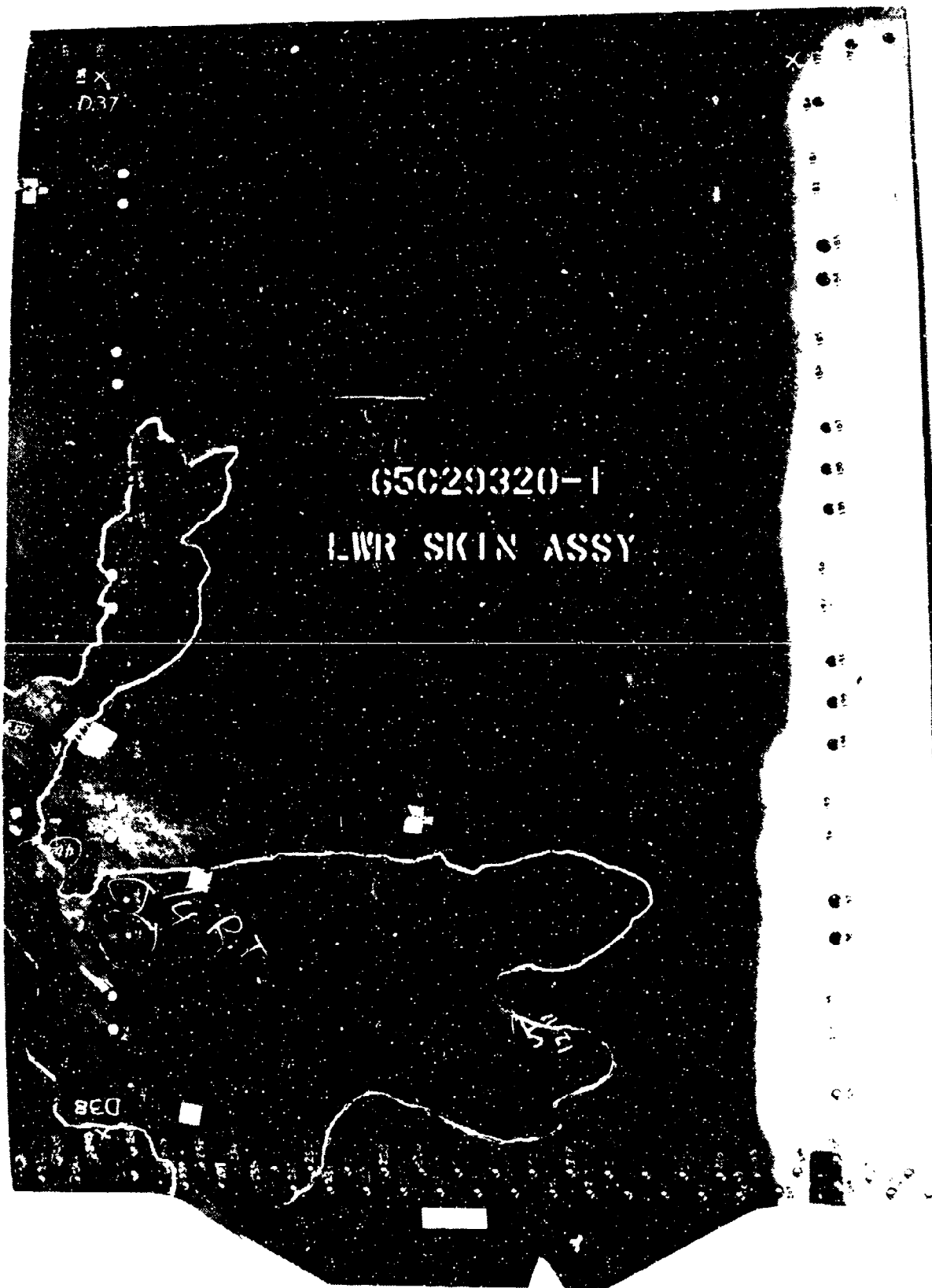


Figure 2-6. J4X Wing Test Box Lower Skin Surface

Following the visual inspections and photo documentation, the damaged central wing box portion was cut out and the major components (skins, ribs, spars, etc.) were separated from one another. During component breakdown, each fastener was carefully removed and examined for proper fabrication and installation. No damage or incorrect manufacturing anomalies were identified related to fastening. Following removal of the skins, spars and ribs in the failure region, each of these components were subjected to C-scan through-transmission ultrasonic (TTU) inspections to more accurately appraise the extent of delaminations. As shown in Figure 2-7, the upper skin surface damage at the trailing edge tab radius was easily defined. Suspecting damage such as small translaminar cracking at the radius on the other side of the tab, radio-opaque penetrant X-ray inspection was performed in this region, however no damage was present.

2.2.3 Materials Characterization

Materials characterization involved performance of the following tests on all components, with a brief summary of the results:

1. Degree of cure (T_g) using TMA flexural method; $T_g = 191^\circ\text{C}$ to 201°C – indicating a proper cure (180°C specification minimum)
2. Resin content using density gradient column method; acceptable 33.8 percent by weight (35 percent prepreg)
3. Microstructure/porosity using optical microscopy; no resin starvation or porosity, no fiber waviness
4. Ply count and orientation using optical microscopy; all components in good condition except slight ply discrepancies in upper skin near trailing edge tab radius
5. Dimensional conformance to engineering drawings; upper skin tab radius was 1.5 inches but the drawing call-out was 3.0 inches (this discrepancy was evaluated by analysis for stress concentration factor, k_t effect).

2.2.4 Fractography

Using the outline of the delamination generated by NDE, the fractures were abrasively sectioned open to minimize artifacts. Detailed crack mapping of the delamination surfaces was performed by optical microscopy, with documentation of the fracture morphologies obtained by the SEM. Areas of delamination were found to be principally Mode I tension dominated, with localized Mode II shear regions. The overall crack growth directions, as well as the fracture origin regions for the upper skin surface and the rear spar are shown in Figure 2-8. These analyses revealed cracking of the upper skin initiated by compression buckling fracture mode at the trailing edge tab radius with resultant fracture propagating toward the leading edge. Similarly, the rear spar fracture originated in a region adjacent to the upper skin surface. Crack mapping in this region was very inconsistent, with a nearly random variation in the microscopic river marks and hackle orientation. No anomalous conditions such as porosity, resin starvation, or chemical contamination were identified in the origin regions.

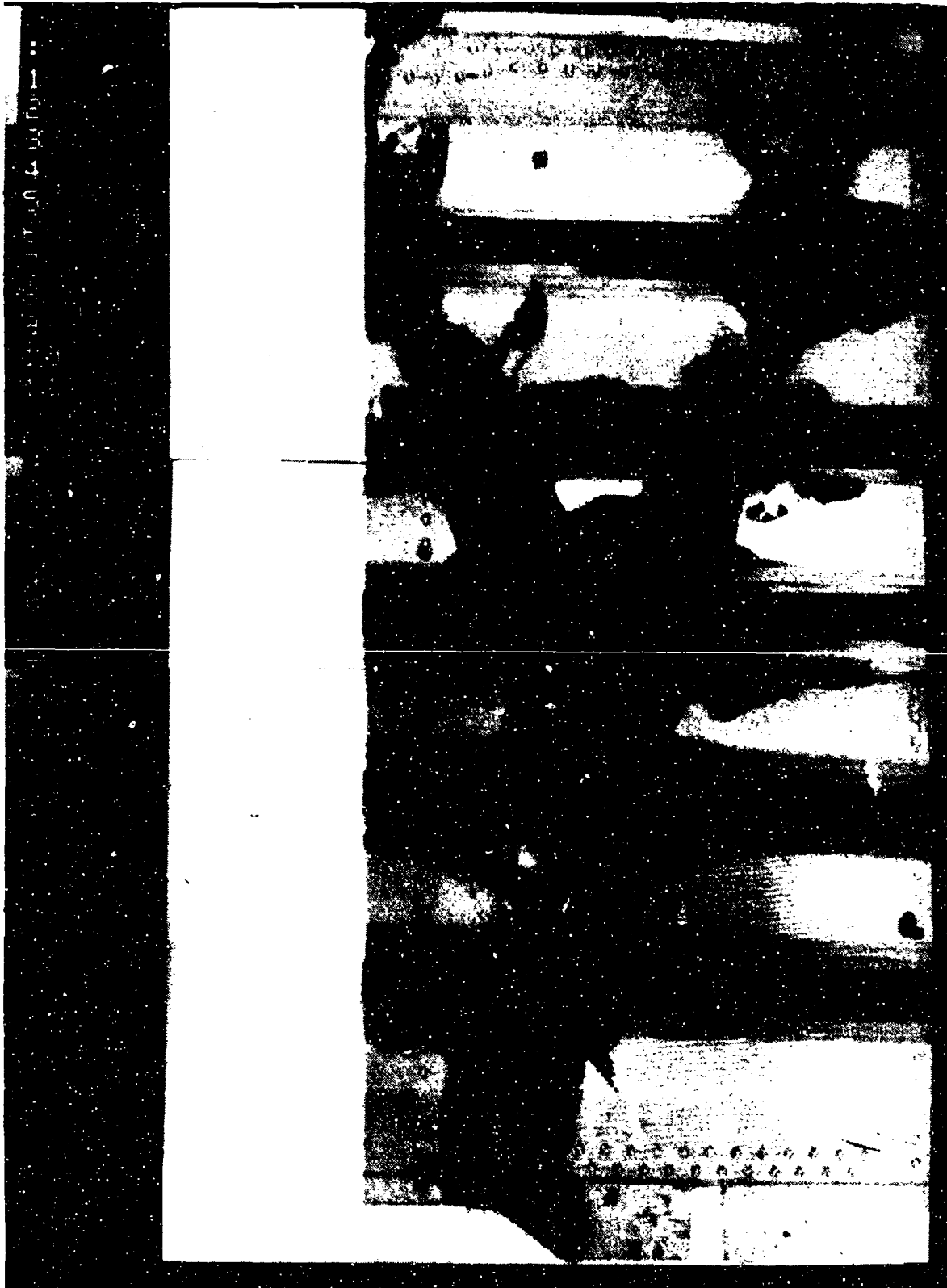


Figure 2-7. Ultrasonic C-Scan of Upper Skin Surface

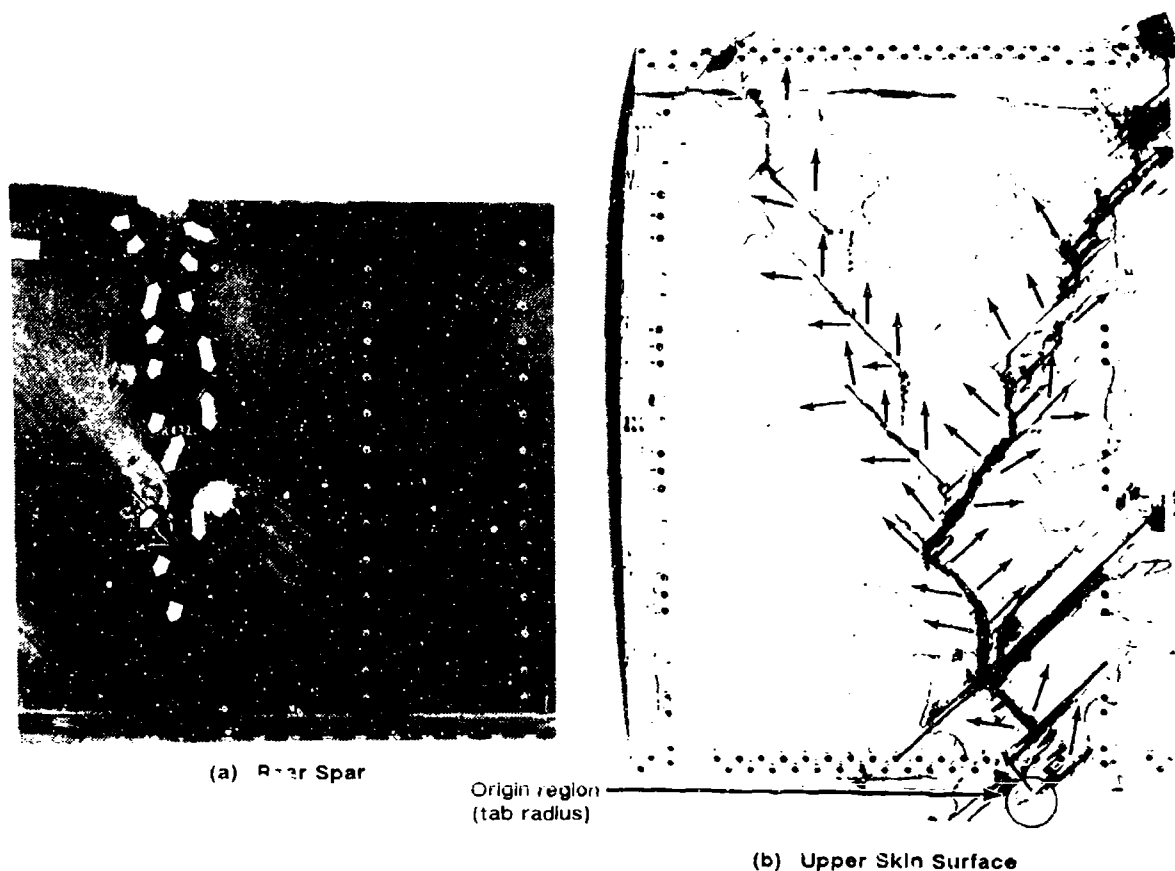


Figure 2-8. JVX Wing Test Box Crack Mapping Results

Similar fractographic analyses were performed on the lower skin and front spar, with crack mapping indicating that the fractures were a direct result of the progression of the cracking from the upper skin and the front spar.

At this point the question of the sequence of failure between the upper skin and the rear spar was asked. Experience with fracture analysis of large composite structures indicated that smaller, well defined origin regions tend to initiate at lower overall strain levels at locations such as notches or holes and therefore exhibit less damage at the origin zone. The larger, ill-defined origin zones tend to be indicative of overload, or rather, high overall strain fractures (with extensive damage); and are not usually associated with notch sensitivities or defect conditions. Using this basis for a rationale, it appeared that the upper skin surface which had the small origin region, may have initiated first, at the tab radius which served as a notch.

2.2.5 Stress Analysis

While the efforts discussed above were being performed, several levels of stress analyses were also performed. These involved the initial design review to check known test conditions against the design envelope, as well as comparing test strains from the strain gauges and coarse global

analyses with the overall strain allowables. The next stage was to take inputs from the materials characterization and the fractography analyses, and evaluate the strain criticality at the structural level. Through finite-element analyses, an unanticipated strain level was identified at the upper skin tab radius, with the notch k_t effect at the radius contributing to the strain level. Subsequently, two small scale replicate panels were fabricated, tested and subjected to complete failure analysis investigations. One panel was fabricated with, and one without, the tab and radii on the skin surface. Through these verification test panels, it was shown that by elimination of the tab, and thus the radii, a premature buckling mode that precipitated fracture could be prevented.

2.3 FAILURE ANALYSIS OF THE NASA HIMAT WING

Failure analysis of the wing was conducted by the Boeing Company.

2.3.1 Background History

Figure 2-9 presents the NASA HIMAT wing section in its as-received condition. This wing was built by Rockwell International for a highly maneuverable research vehicle to study future designs for the next generation of U.S. fighters. The composite wing is a 44 percent scale model, to lower overall program cost and risk. Following numerous unmanned test flights, the outboard sweeping section of the wing was removed and subjected to simulated flight spectrum mechanical testing in the laboratory. Information supplied at this stage in the investigation regarding construction was very limited; the outboard canard was found to be fabricated from aluminum alloy and the remaining portion of the wing was fabricated from a continuous fiber reinforced laminate. Failure, denoted as a loss of structural stiffness, occurred during the mechanical testing.

2.3.2 Nondestructive Evaluation

Nondestructive evaluation was performed on the entire wing to determine areas of damage or defect conditions caused from testing or manufacturing. A wide variety of NDE techniques were used, primarily to evaluate each technique and to more completely determine the construction of the wing. The following techniques were applied; visual inspection, radiography, through-transmission ultrasonics (C-scan), pulse-echo (B-scan), eddy current, and ultrasonic bond testing. Of these six, the key methods used to obtain data were visual inspection, TTU, and hand-held pulse echo.

Although no visible primary trans laminar fractures were identified, visual examinations revealed several delaminations along the inboard edge (up to 13 cm in length), disbonds (up to 3 cm in length), and surface delaminations (up to 13 cm by 8 cm). Blunt gouges were found at the center of two of the delaminations along the inboard edge of upper skin, appearing to be mechanically induced after part cure. This damage may have occurred during wing removal following flight testing. These gouges are shown in Figure 2-10. On the upper skin, an area was mechanically abraded, indicative of surface repair.

TTU analysis provided a through scan of the discontinuities along the upper and lower skins. The major delaminations and disbonds occurred along the inboard edge of the wing, with the exception of one donut-shaped delamination at the center of the wing. Figures 2-11 and 2-12 show

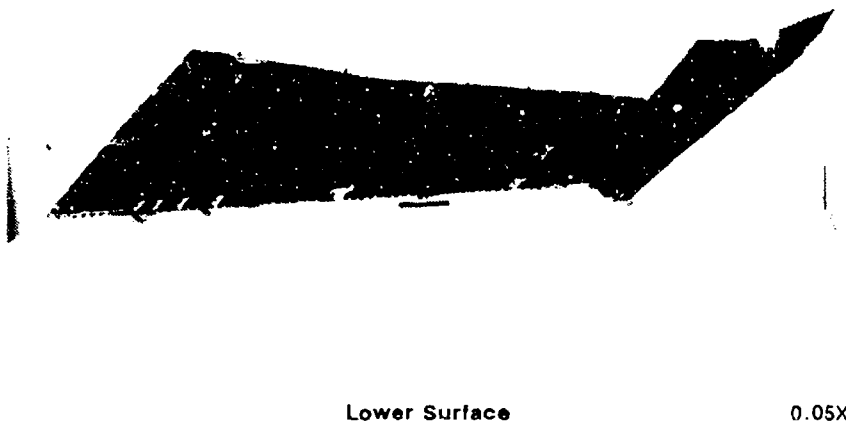
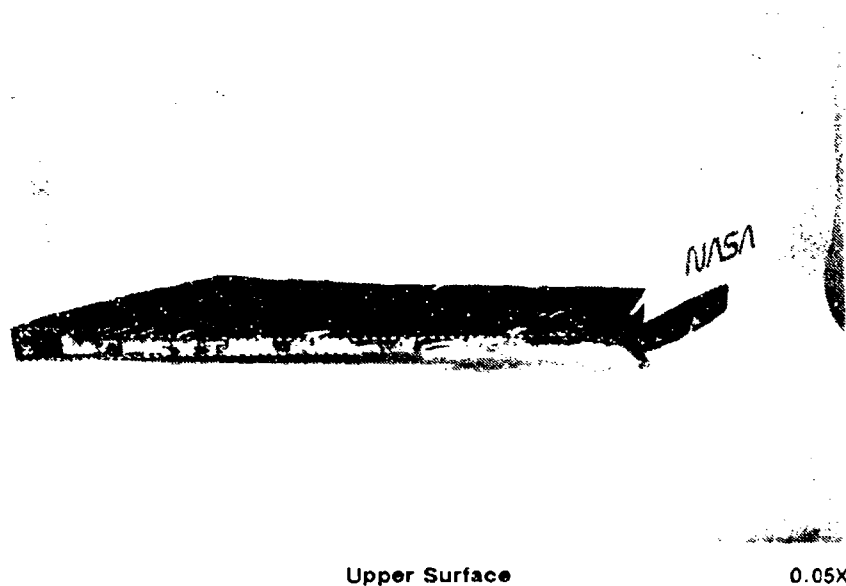
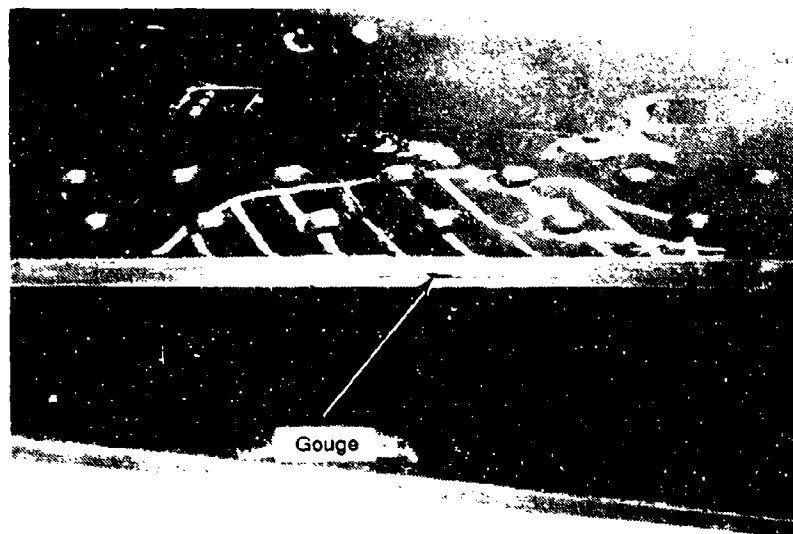


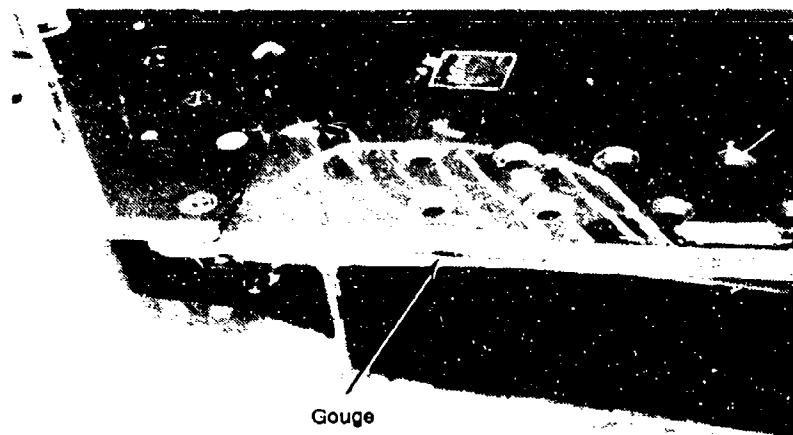
Figure 2-9. NASA HiMAT Test Wing in the As-Received Condition

the TTU hard copy printout. The areas indicated by alphabetical flagnotes were delaminations or disbonds which were crack mapped during subsequent fractographic examinations. However, the areas shown with numerical flagnotes were defects indicated by X-ray, such as core to skin disbonds, core crush, and water in the core cells.



(a) Section C

0.8X



(b) Section B

0.63X

Figure 2-10. Upper Skin Inboard Edge Damage

The hand-held pulse-echo inspections revealed the depth of each defect. The deepest delamination occurred 0.86 cm (0.34 inches) below the skin surface. These depth measurements became very useful when the handmilling cuts were made to remove the delamination regions. This allowed precise cutting, reducing the extent of damage to the remaining portion of the wing, and allowed a more successful repair.

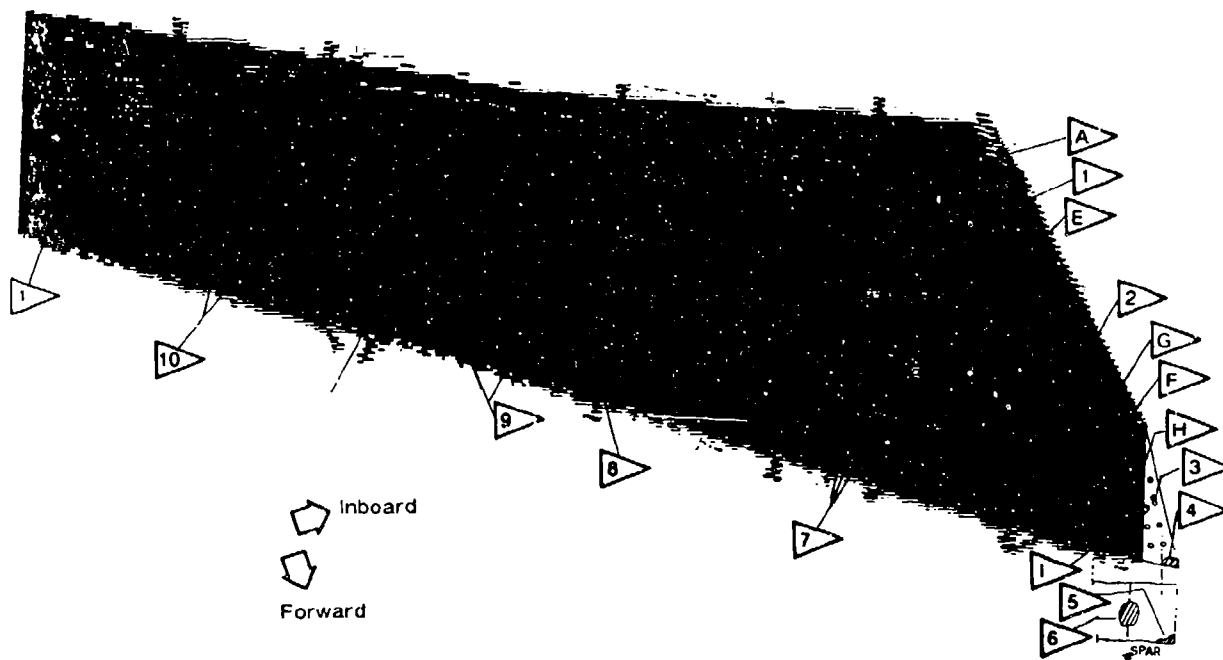


Figure 2-11. NDE Results of the Lower Surface

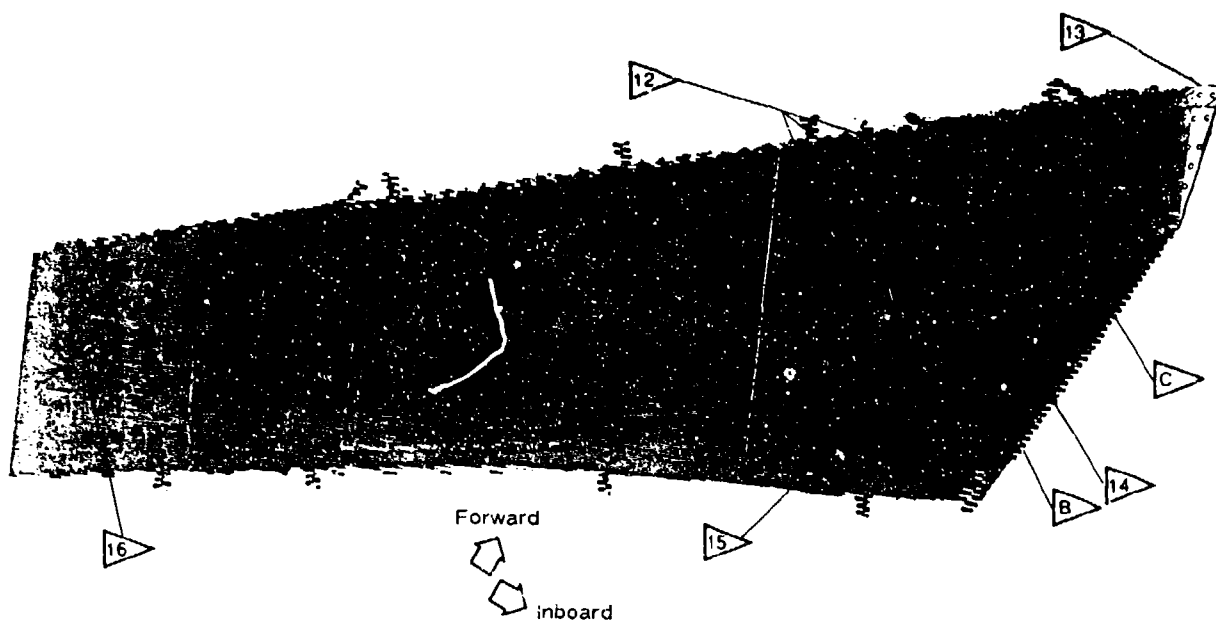


Figure 2-12. NDE Results of the Upper Surface

2.3.3 Materials Characterization

Following the nondestructive inspection, material characterization of the wing was performed to verify material composition, ply orientation, ply layup, and material processing/cure.

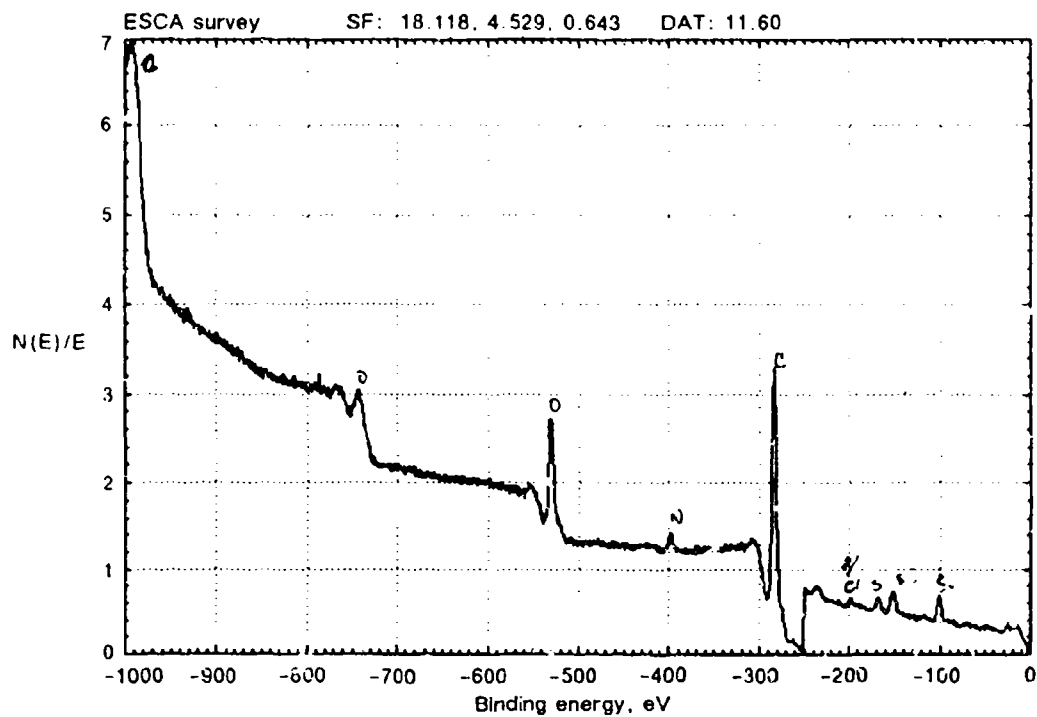
The materials used to construct the wing were found to be carbon, boron-tungsten, and fiberglass fibers in an epoxy resin. These material constituents were identified by the following techniques: scanning electron microscopy, optical microscopy, electron probe microanalysis, and electron scattering for chemical analysis (ESCA). The fibers were identified by SEM, ESCA (Figure 2-13), and optical microscopy (Figure 2-14). The novalac based epoxy resin was identified by infrared spectroscopy.

The ply orientation and number of plies were found to be consistent with engineering drawing specifications. Localized discontinuities such as resin-rich and resin-starved regions (Figure 2-15) were usually caused by misalignments of the extremely large boron fibers. A small amount of porosity was seen in the graphite/epoxy plies between the 0 and 90 degree plies. These discontinuities were not found to be associated with the delamination regions and therefore were not considered as contributory factors to the cause of part failure.

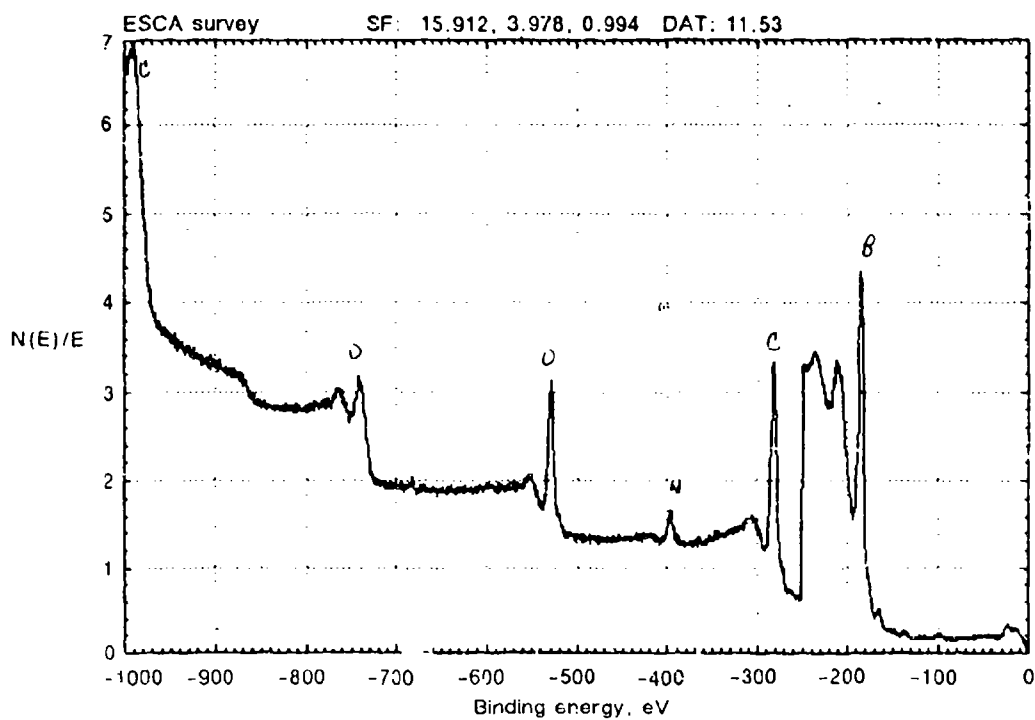
Using thermomechanical analysis (TMA) in the flexure mode, the Tg was found to be 212°C, consistent with specification requirements for a 177°C cure system.

2.3.4 Fractography

Since materials characterization tests revealed that the laminate was constructed per specification and drawing requirements, efforts were directed toward the determination of the fractographic features related to each of the delaminations identified by NDE. Using optical microscopy, each of the delaminations were crack mapped to determine the mode of fracture, the origin location, and any anomalous conditions associated with the origin. The fracture mode was primarily interlaminar or intralaminar Mode I tension, with origin locations at edge defects or fastener bores. Crack initiation was found to be due to a variety of causes, including mishandling, improper bonding of the honeycomb, and improper hole drilling. The delamination interfaces were primarily between the fiberglass and boron plies or between the 0 and 90 degree graphite plies, which are often considered the weaker interfaces in a laminate. Two delaminations at the edge of the upper skin surface exhibited features indicative of crack growth by cyclic loading, evident by the presence of macroscopic beach marks (Figure 2-16) or extensive rubbing damage of the mating fracture surfaces. Both of these fractures initiated at gouges at the inboard edge, possibly due to mechanical prying with blunt instruments during separation of the outboard section of the wing (following flight tests and prior to laboratory flight spectrum loading). No indications of cyclic crack growth (due to mechanical testing) were found on the other fractures. Table 2-1 illustrates the features identified for each of the delamination regions. Figure 2-17 presents several of the fracture surfaces with arrows defining the direction of crack growth.



(a) Carbon Fiber Identification



(b) Boron Fiber Identification

Figure 2-13. Fiber Identification by Surface Analysis

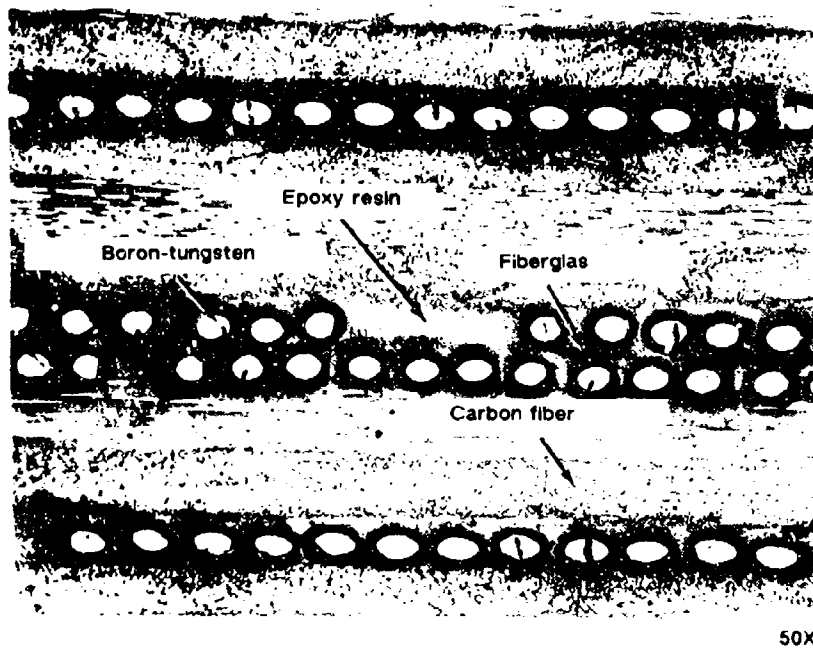


Figure 2-14. Photomicrograph of Zone B Cross-Section

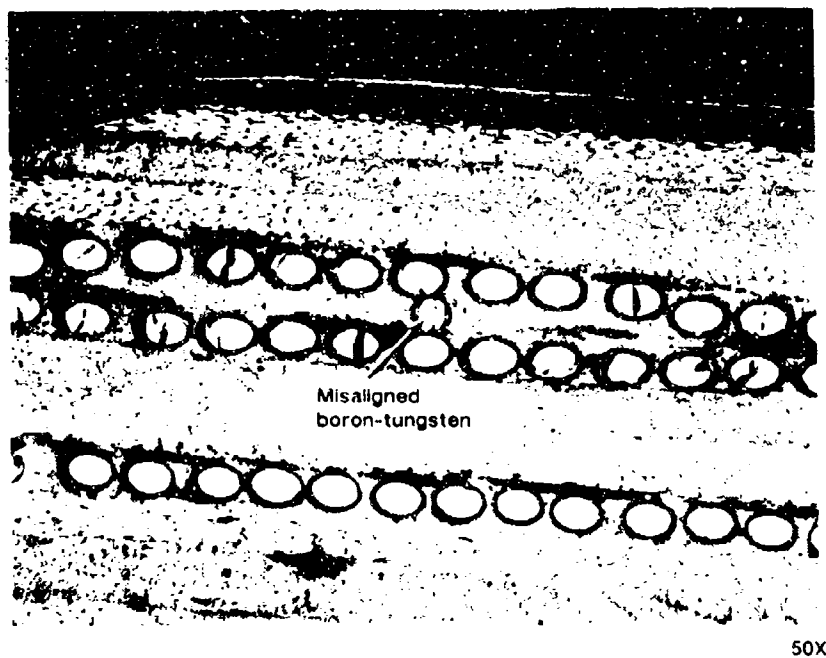


Figure 2-15. Cross-Section Illustrating Boron Fiber Misalignment Resulting in Resin-Rich Adjacent Regions

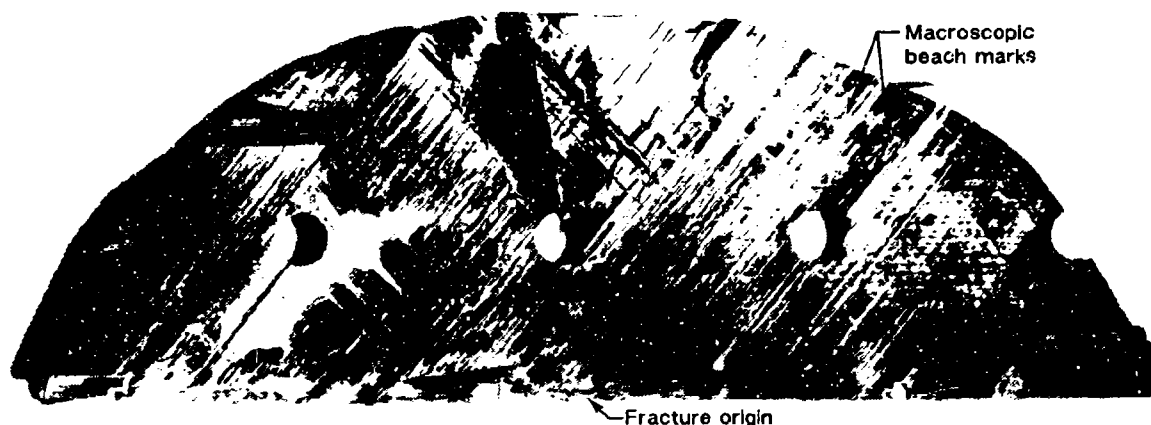
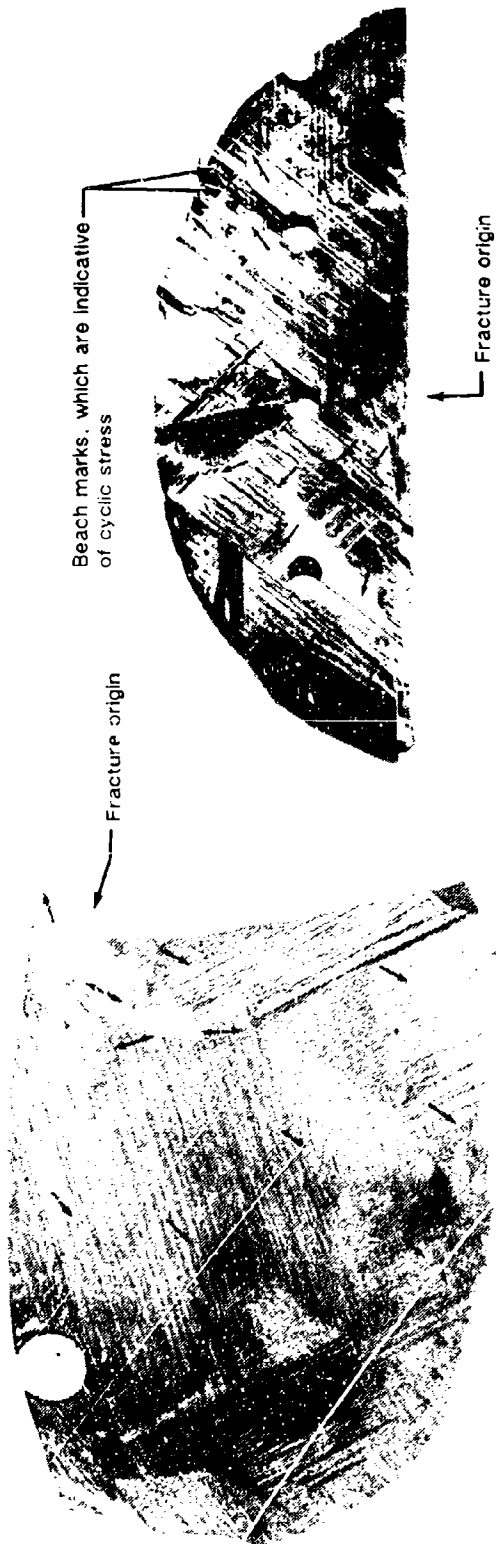


Figure 2-16. Photomicrograph of Beach Marks Indicative of Cyclic Crack Growth and Crack Propagation Direction

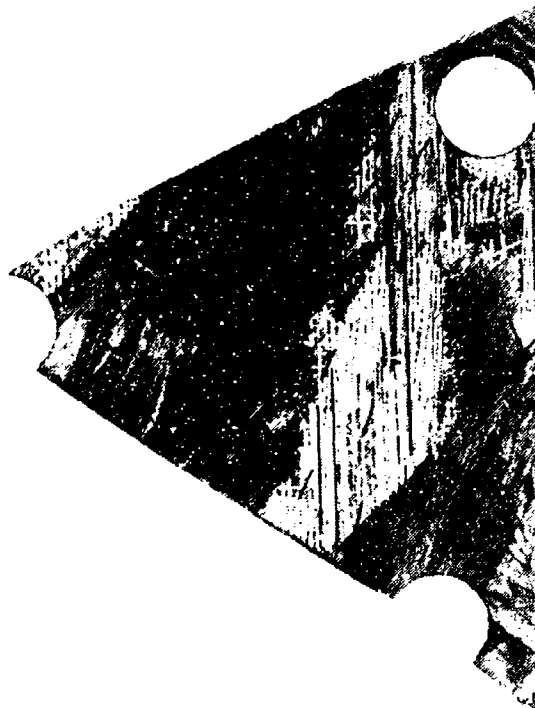
Table 2-1. Fractography Results From NASA HiMAT Wing

Delamination	Origin location	Fracture mode	Comments region
Section A	At sharp radius at edge of skin	Mode II shear at origin with mode I tension growth	Boron-fiberglass interface
Section B	Likely at an edge gouge	Not determinable	Abrasive rubbing prevented analyses
Section C	At edge gouge	Mode I tension	Radial crack growth with beach marks from cyclic loading
Section D	Not determined	Mode I tension	Donut-shaped defect
Section E	Fastener bore	Mode I tension	Boron-fiberglass interface
Sections F and G	At edge with no defect	Mode I tension	Crack arrested at fastener bore
Section H	Fastener bore	Mode I tension	Resin particulate from drilling-induced delamination
Section I	Fastener bore	Mode I tension	Porosity aided crack initiation of fabric graphite plies

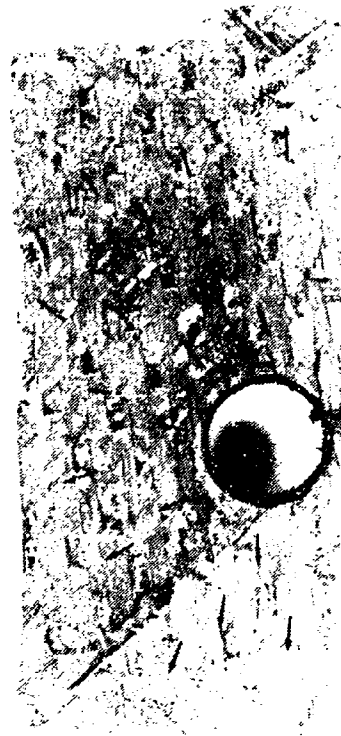


Section A

Section C



Section E



Section I

Figure 2-17. Crack Mapping Results From Selected Delamination Regions

2.3.5 Stress Analysis

Stress analysis was not performed. This was due to limited funding and because the majority of the delaminations were associated with defect conditions identified by the techniques described above.

2.4 FAILURE ANALYSIS OF A CARBON FIBER REINFORCED PLASTIC I-BEAM

Failure analysis of the I-beam was conducted by the Boeing Company.

2.4.1 Background History

Figure 2-18 shows the I-beam in its as-received condition. This component was fabricated by the personnel at the Air Force Wright Patterson Aeronautical Laboratories (AFWAL). Information regarding the component's layup, material composition, resin content, and cure temperature was provided by AFWAL. The component was tested in a four point bend test. The I-beam consisted of a tape laminate with vertical web and two horizontal caps, similar to stringers used to stiffen skins on aircraft wing construction. Small vertical stiffeners were secondarily bonded at several locations along the length to provide support of the cap flanges during loading. Efforts were aimed at determining the cause of failure with the quickest and lowest cost methods available. As a result, examinations such as fractography were performed without an SEM, relying on macroscopic and optical means of identifying the sequence and origin of fracture.

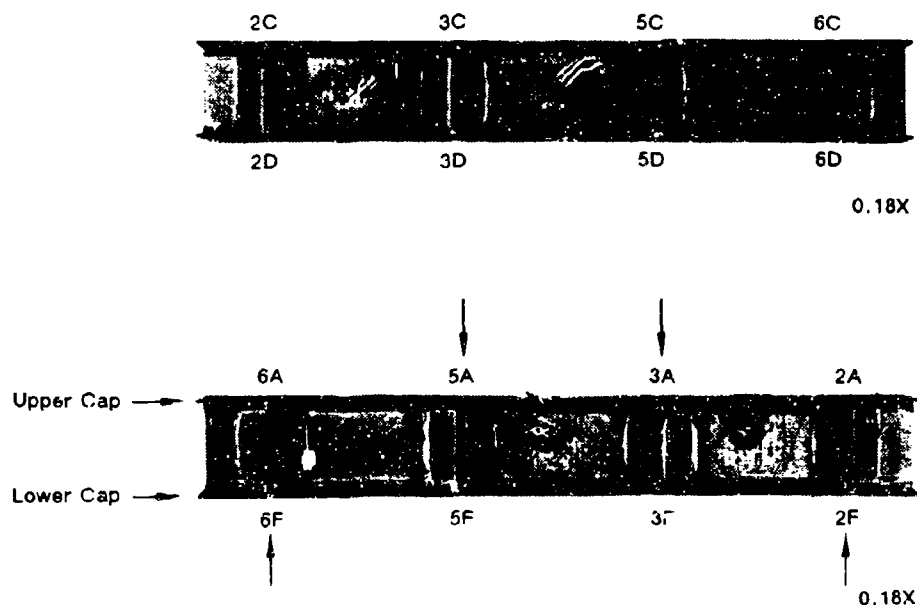


Figure 2-18. CFRP I-Beam in the As-Received Condition

2.4.2 Nondestructive Evaluation

NDE was performed on the I-beam to determine areas of damage or defects caused from testing or manufacturing. Visual inspection of the beam revealed bearing damage on the caps indicative of the loading points during mechanical testing. This allowed determination of the types of stress, (that is, compression, tension or shear) imparted on the various regions of the beam. For continuity throughout this discussion, the upper cap was compressively loaded and the lower cap was in tension during flexural loading. Delaminations were found at two locations in the upper cap, with remaining damage limited to brooming (localized buckling) of the small vertical stiffeners immediately below the two center loading points, most likely due to the compressive loading. These damage conditions are presented in Figures 2-19 and 2-20. TTU inspection required three scans to evaluate the entire beam. First, the vertical web section was inspected. Since no delaminations were identified, the beam was cut longitudinally along the web to allow the upper compression cap to be inspected. The upper cap was found to be delaminated in the identical regions which were visually identifiable (Figure 2-21). The upper cap was free of delaminations in the central region between the two loading points (an area of pure compression loading and no shear stress in the laminate plane).

2.4.3 Materials Characterization

Cross-sections were performed on the ends of the beam to evaluate the laminate quality and construction. Ply counts indicated that the beam was fabricated with the correct number and orientation of plies. The overall part quality was found to be poor; extensive porosity was located at the web-to-cap junction and lack of adequate tooling constraint during cure allowed deformation of the entire laminate thickness (Figure 2-22).

Fiber diameters were measured to identify the fiber type (carbon AS4). Infrared spectroscopy was used to identify the novalac based epoxy resin and the presence of sulphur compounds indicative of a diaminodiphenyl sulphone (DDS) hardener used in epoxy resin systems. Thermomechanical analysis (TMA) using the flexural method was employed to determine a Tg of 379°F, verifying a complete cure of a 177°C (350°F) cure system. The resin contents of the caps were determined by the density gradient column method. The resin content was 27 percent by weight, much less than that of the original prepreg which was approximately 34 percent. This was a definite concern since resin contents below 30 percent have been shown to significantly reduce the laminate strength, particularly for resin dominated fractures such as interlaminar shear and tension or compression buckling.

2.4.4 Fractography

The delaminations in the upper cap were removed by cutting to prevent further delamination. Visual macroscopic inspection of the surfaces revealed the presence of both shiny and milky appearing regions, indicative of tension and shear dominated delaminations, respectively. The fracture occurred at the interface between the 0 and 45 degree plies, most likely due to the stress gradient between the axial 0 degree ply (which carries the primary axial flexural loads) and the off-axis 45 degree ply. Crack mapping was performed with the optical microscope, with the localized

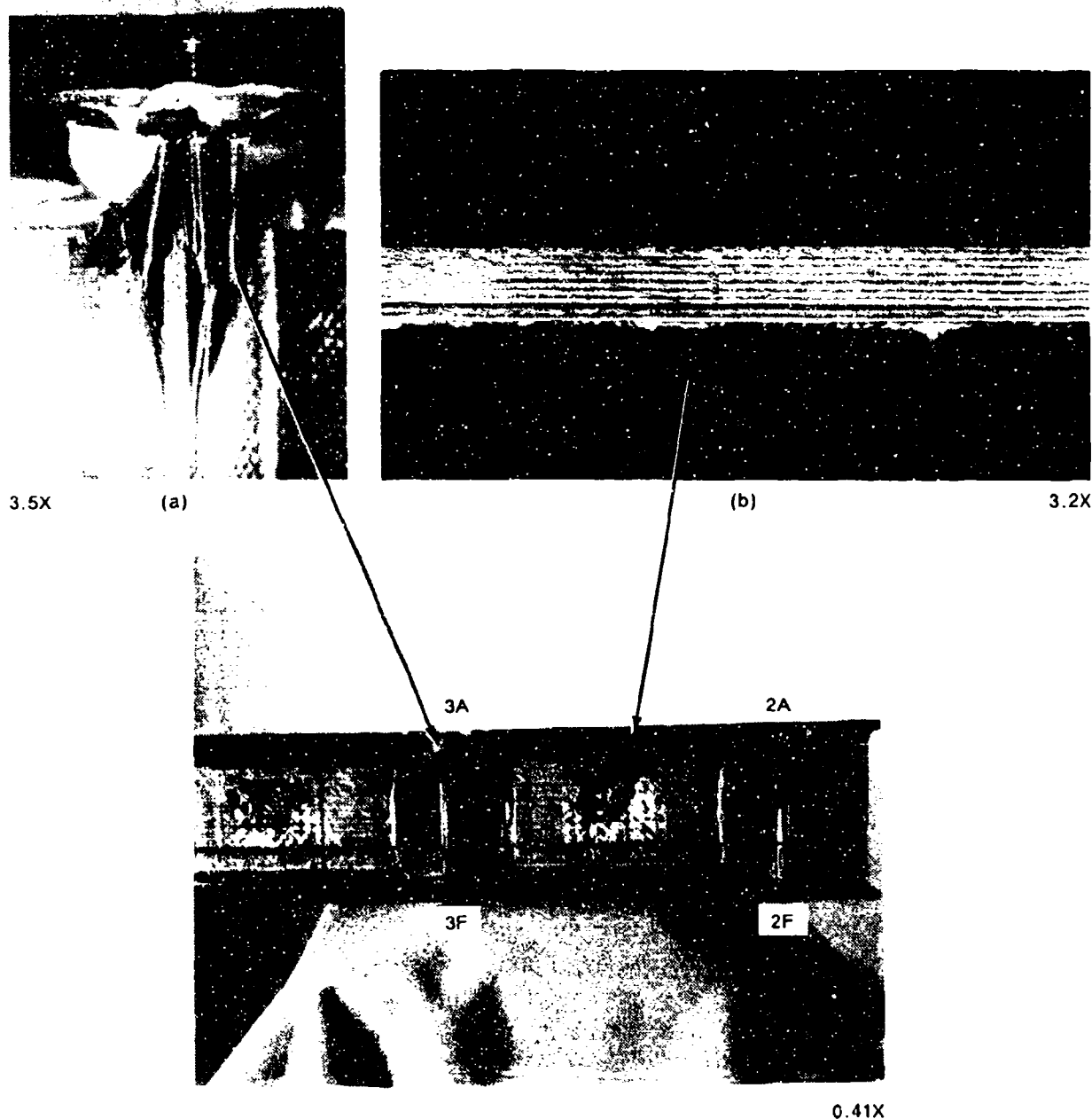


Figure 2-19. Regions of (a) Compression Buckling and (b) Delamination in the Upper Cap Section of the I-Beam

crack directions determined by examining the orientation of the hackles in the shear dominated regions and the river marks in the tension dominated regions. Cracking was found to initiate by shear at the web-to-cap junction, under the loading contact points. Cracking continued along the central region of the cap (where extensive porosity was evident) by mixed mode, although primarily tension toward the ends of the beam, as shown in Figure 2-23.

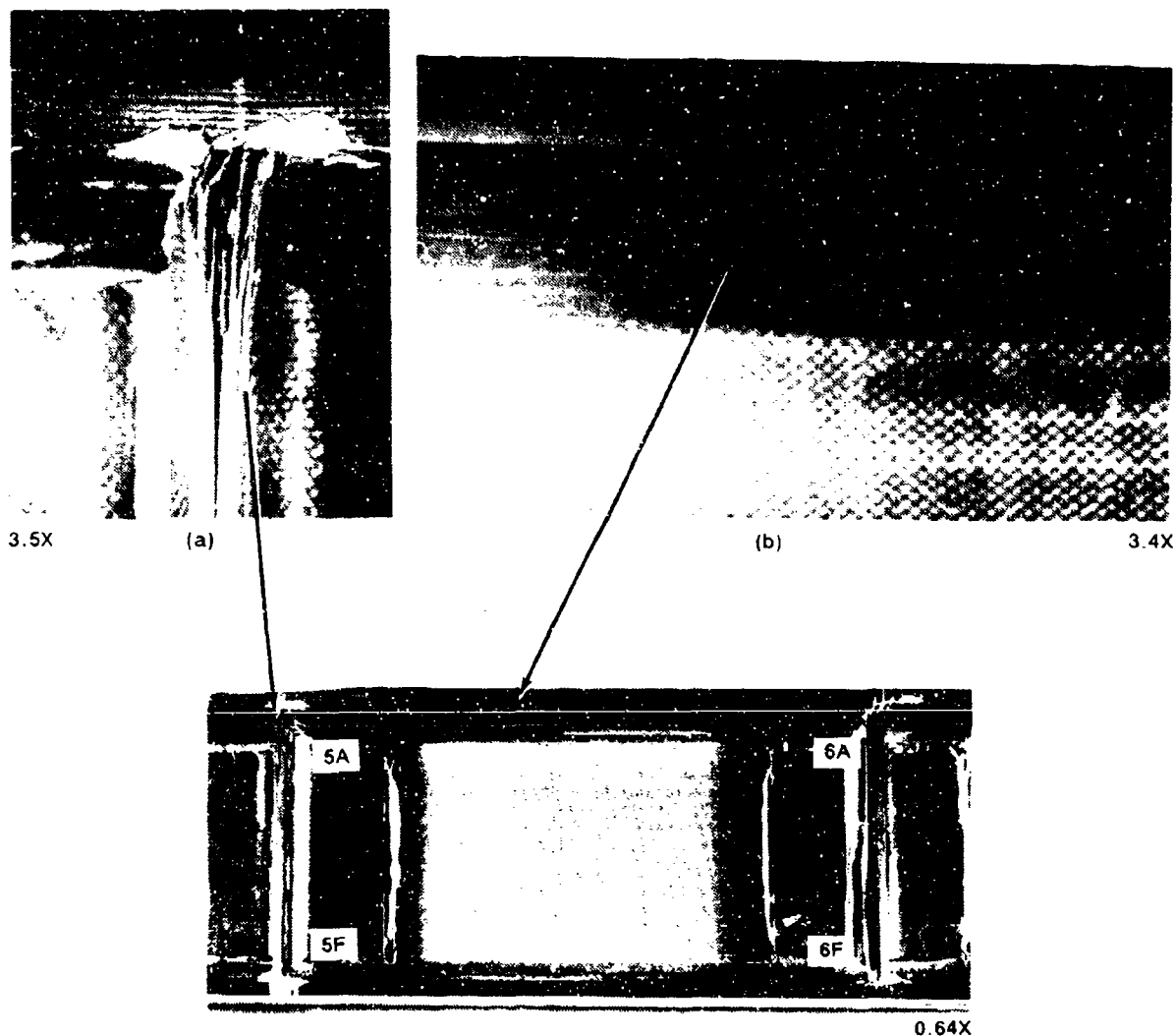


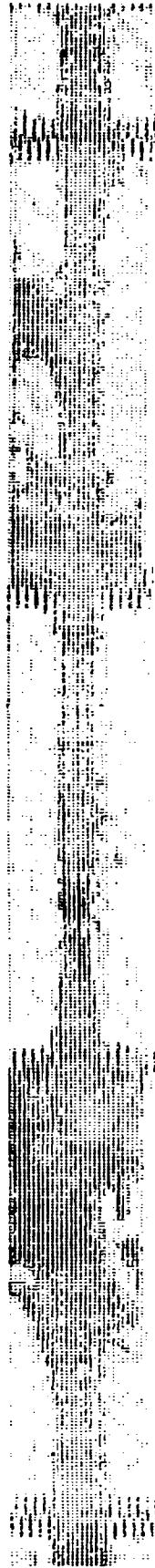
Figure 2-20. Regions of (a) Compression Buckling and (b) Delamination in the Upper Cap Section of the I-Beam

2.4.5 Stress Analysis

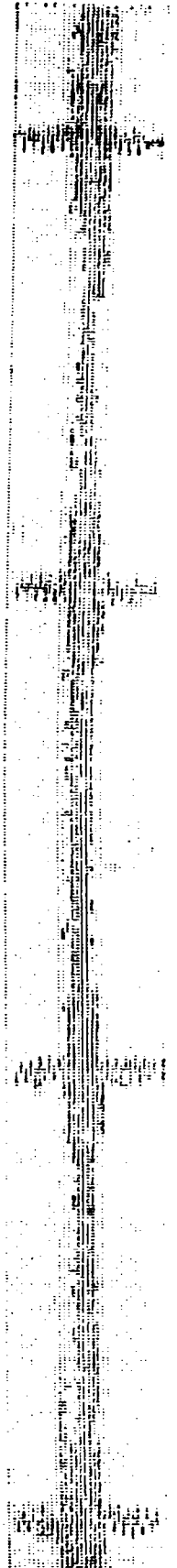
Although no calculations were performed, simple beam flexure theory identified the presence of an interlaminar shear stress gradient in the upper cap, being most concentrated immediately under the central bearing points and reducing in stress toward the beam ends. This gradient accounts for crack initiation by interlaminar shear at the load point, aided by the reduced strength in the cap due to extensive porosity.

CD

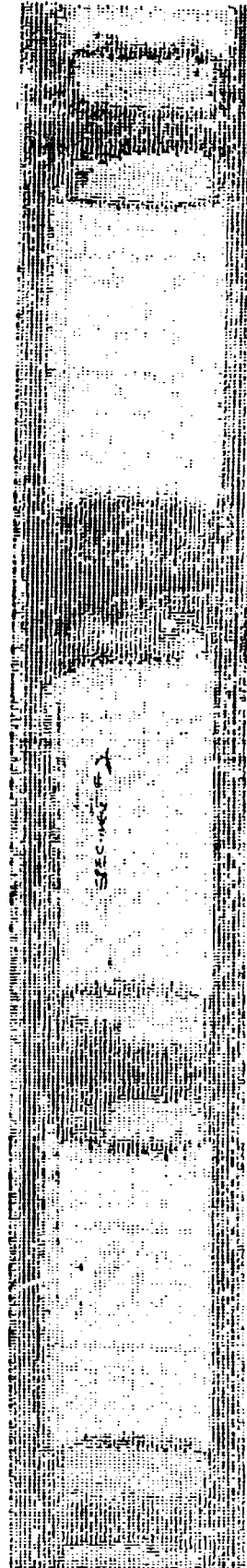
CD



Upper Cap



Lower Cap



Web Region

Figure 2-21. TTU C-Scans of the I-Beam Subcomponents



Figure 2-22. Extensive Porosity and Laminate Deformity in the Web-to-Cap Junction



Figure 2-23. Results of Fractographic Crack Mapping of an Upper Cap Delamination

2.5 FAILURE ANALYSIS OF A BALLISTICALLY DAMAGED COMPOSITE TEST PANEL

Failure analysis of the ballistically damaged composite test panel was conducted by the Boeing Company.

2.5.1 Background History

Figure 2-24 shows the fractured test panel in its as-received condition. The rectangular panel, with a dimension of 43 by 36 inches, appeared to have been fastened to one or more fixed structures during testing. Due to limited background information, the emphasis was placed on the visual examination. At the time of the part's receipt, it was speculated that the part had been fractured via impact loading. This speculation was made due to the appearance of the damage which was typical of that observed in impact loaded structures.

2.5.2 Visual Examination

As shown in Figure 2-25, the damage appeared to have been caused by an object penetrating through the panel from the interior surface (Figure 2-25a), as evidenced by the brooming fibers on the exterior surface (Figure 2-25b). These damage features are commonly observed in an impacted specimen.

In conjunction with stress analysis, visual examination was performed using fastener hole damage as evidence to determine the loading condition experienced by the panel during the test. The key evidence was the depth and elongation of the hole. In general, hole elongation indicates shear-type loading in which the head and the shank of the fastener tilt at an angle to the hole. Figure 2-26 illustrates the damage of a typical shear loaded fastener hole. The damage seen in the countersunk region of the fastener hole was created by the fastener head which dug into the laminate due to the test load. In contrast, tension loaded fastener holes did not show any sign of elongation, retaining their circular shape (Figure 2-27). The fastener head dug beyond the countersunk region causing severe delamination near the inner edge of the hole. Figure 2-28 shows the mapping of the fastener hole damage. From the mapping, it was determined that Region A of the panel was loaded under tension and shear. However, Region B seemed to have been securely fastened to a fixed structure as evidenced by the lack of fastener hole damage in that portion of the panel.

The fastener hole damage also provided information to verify the proper use of the fasteners or the fastener holes for the particular load conditions applied. Two commonly used fasteners were placed into an undamaged fastener hole to determine which had been used (Figure 2-29). The tensile fastener, which has a slightly larger head diameter than the (intermediate) shear fastener, fitted flush into the undamaged hole. However, when the fasteners were placed into one of the fastener holes damaged from tensile loading (Figure 2-30) it was evident that the shear fastener was used. The tensile fastener head was too large for this particular fastener hole damage, but the shear fastener fitted almost perfectly into the damaged hole. The above macroscopic analysis suggests that the tensile fasteners were used for Region B and shear fasteners were used for Region A.

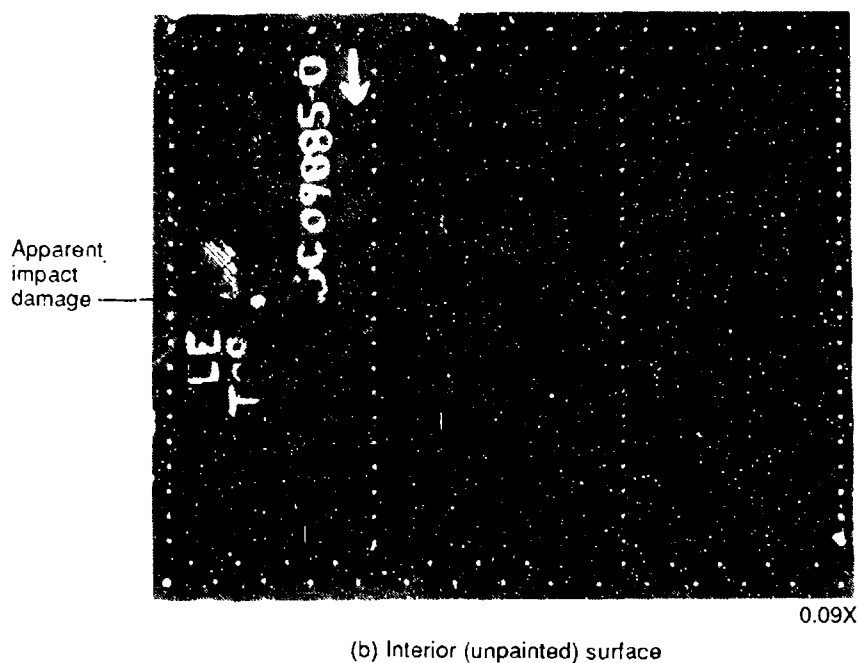
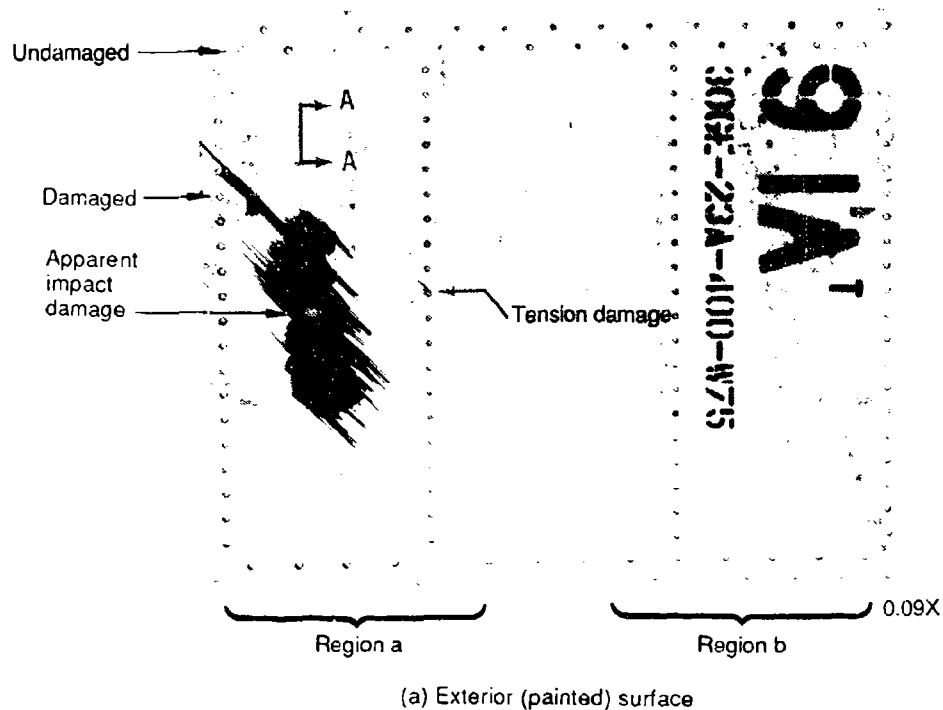
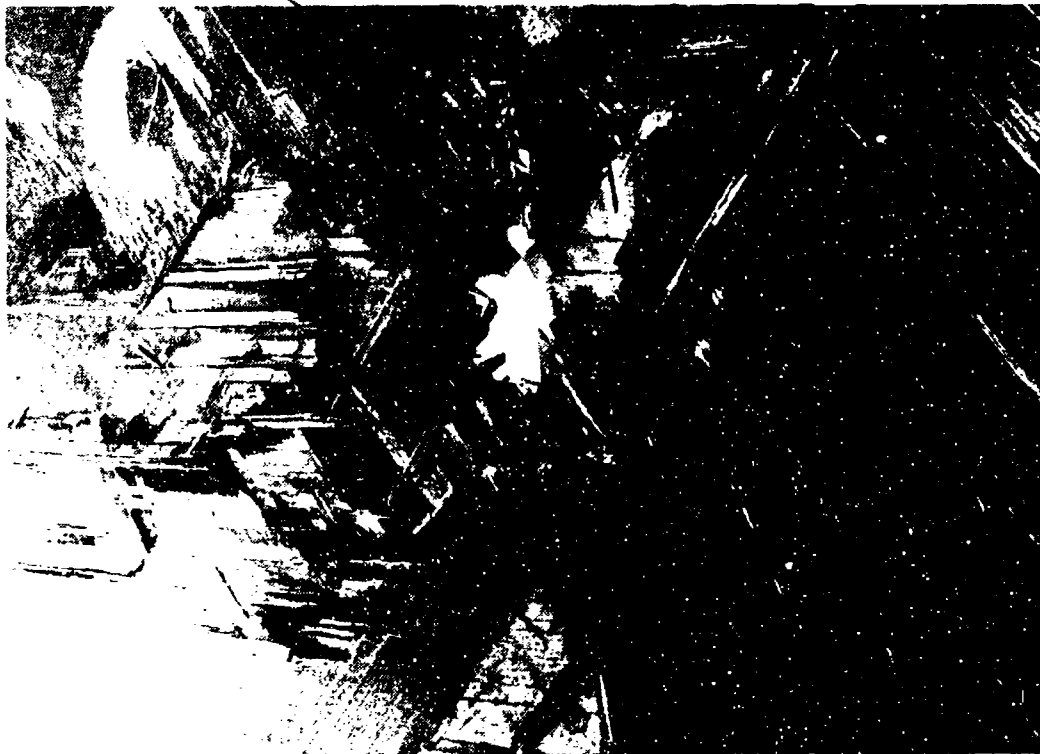


Figure 2-24. Photomicrographs of the Component As-Received



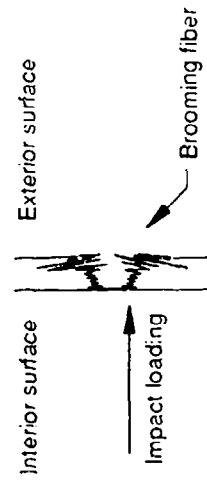
(a) Damage on the interior surface

Note the depression at the impact site which indicates the direction of the penetration

Brooming fiber



(b) Damage on the exterior surface



(c) Clarification schematic

Figure 2-25. Apparent Impact Damage

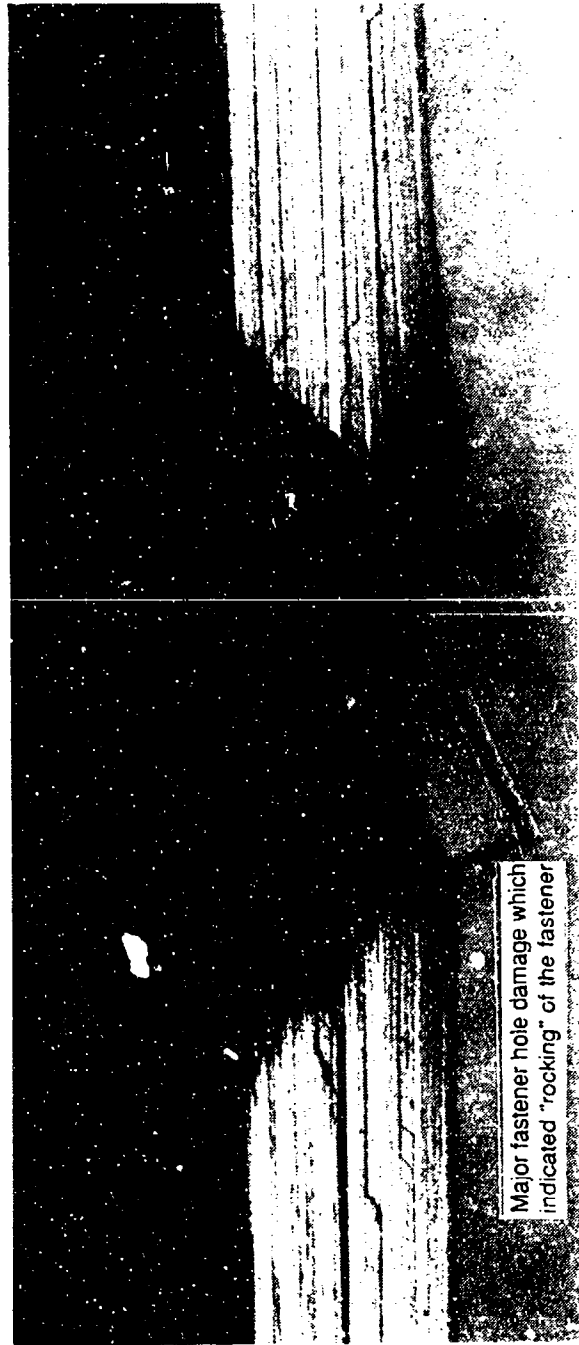
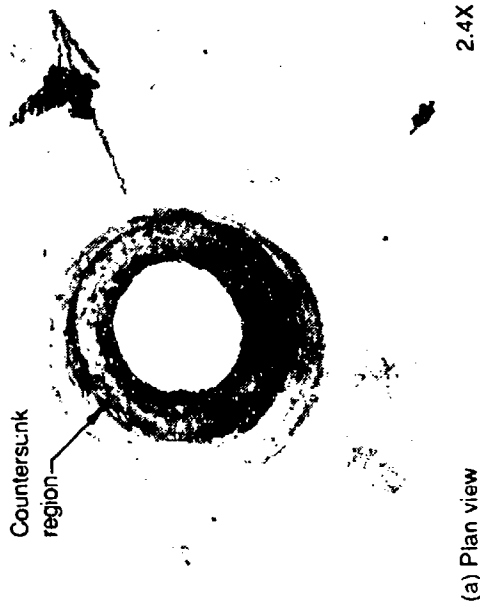


Figure 2-26. Damage in Fastener Hole Loaded Under Shear



(a) Plan view

2.4X



(b) Cross-sectional view

8X

Figure 2-27. Damage in Fastener Hole Loaded Under Tension

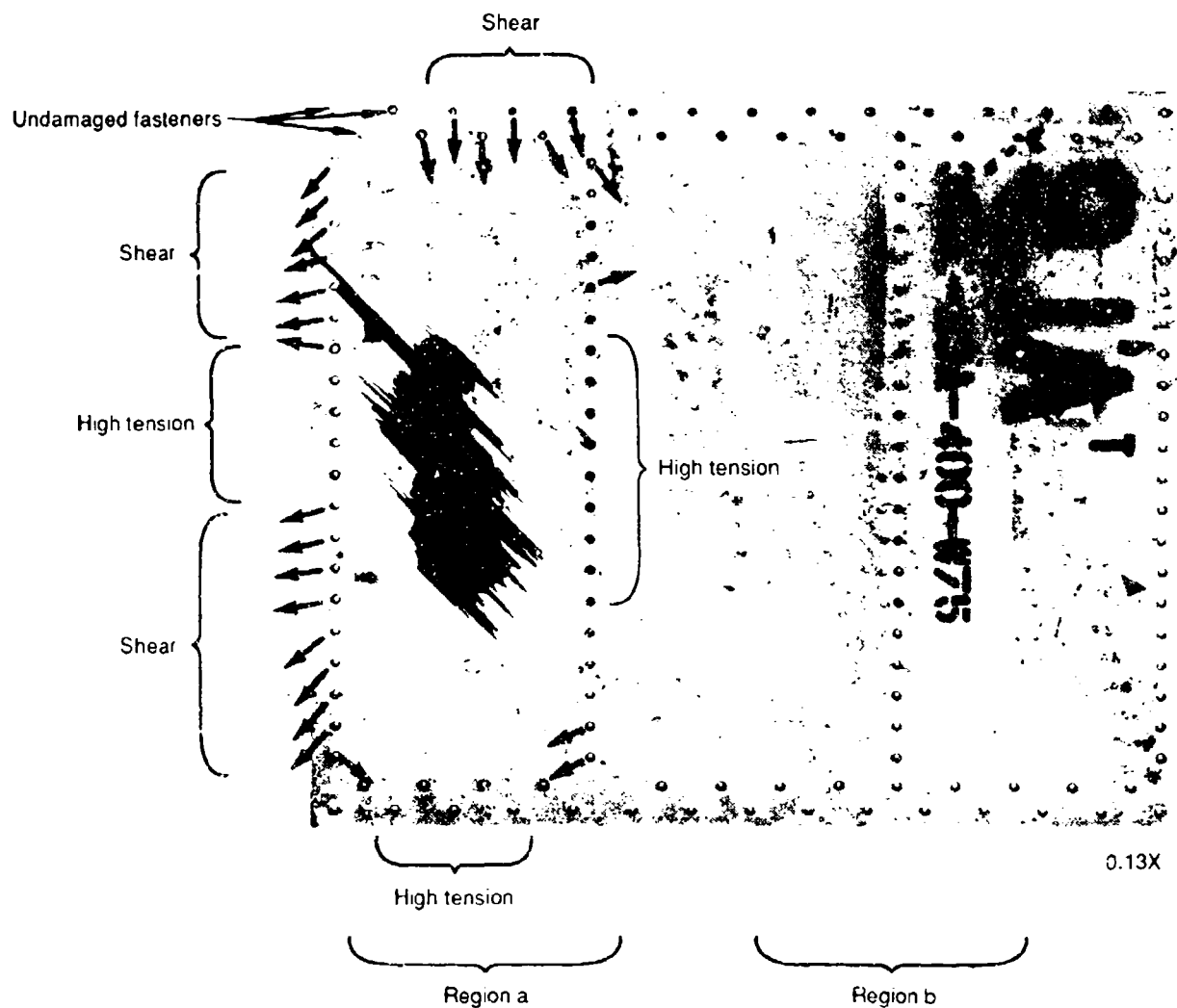


Figure 2-28. Mapping of the Fastener Hole Damage



(a) Tensile fastener

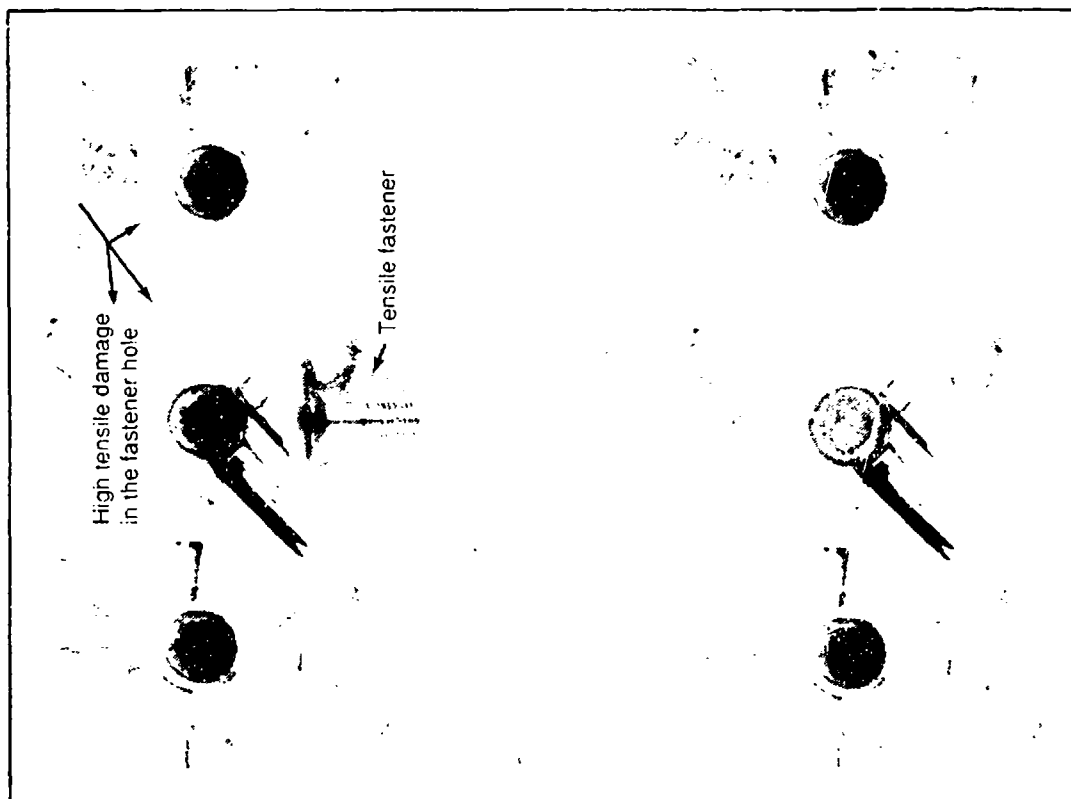
2.7X



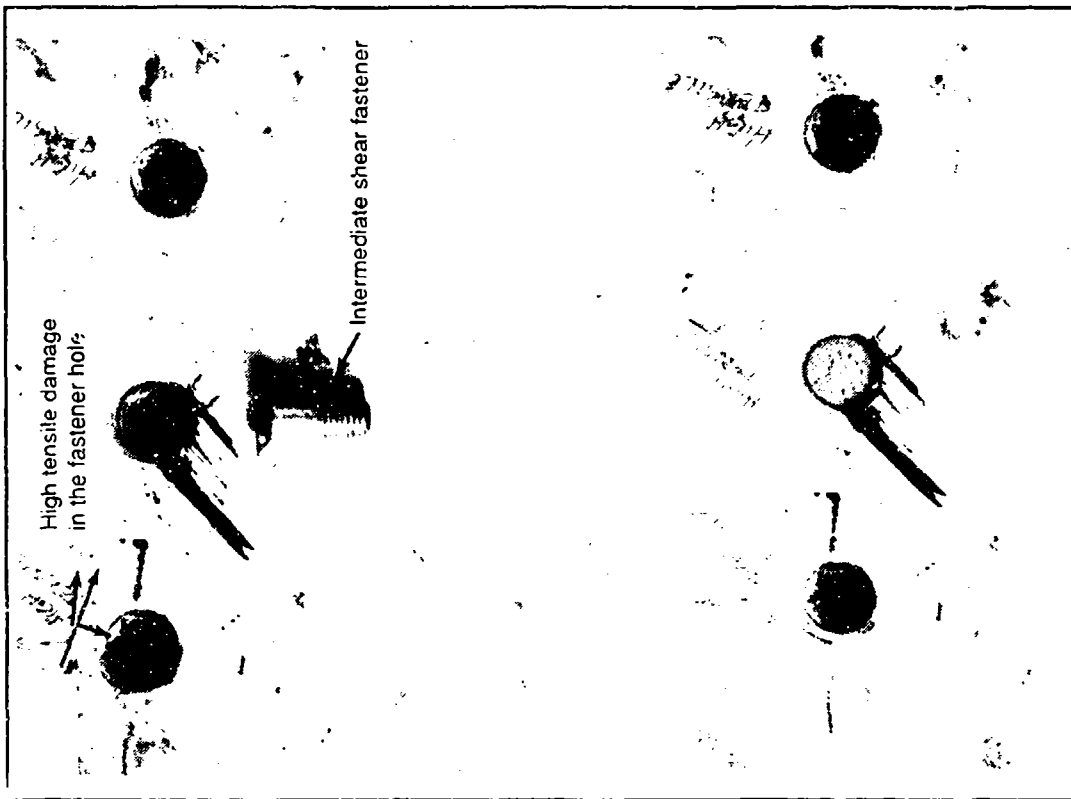
(b) Shear fastener

2.7X

Figure 2-29. Difference in Fastener Fit in the Undamaged Fastener Hole



a. Tensile fastener (fits loosely in fastener hole) 0.9X



b. Shear (intermediate) fastener (fits snugly in fastener hole) 0.9X

Figure 2-30. Macrophotographs Showing the Fit of the Fastener in the Damaged Holes

2.5.3 Nondestructive Evaluation

To determine the extent of the damage, through-transmission ultrasonic inspection (C-scan) was performed. The dark-shaded regions in the vicinity of the fastener holes and at the apparent impact site indicate the damaged region. These regions are shaded due to higher attenuation from the anomalous regions. Most of the damage occurred on one half of the panel, Region A, as shown in Figure 2-31.

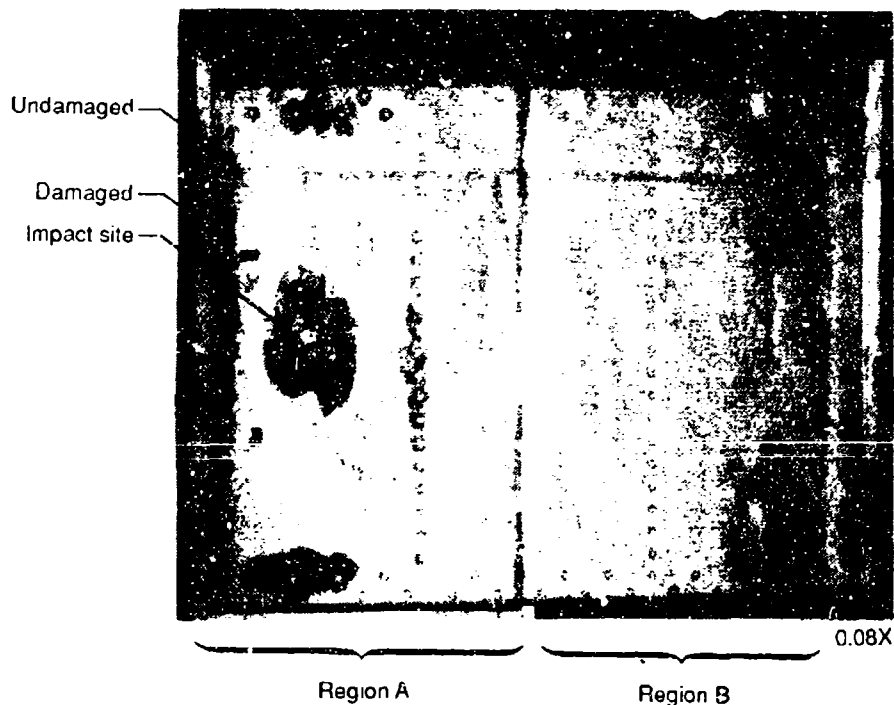
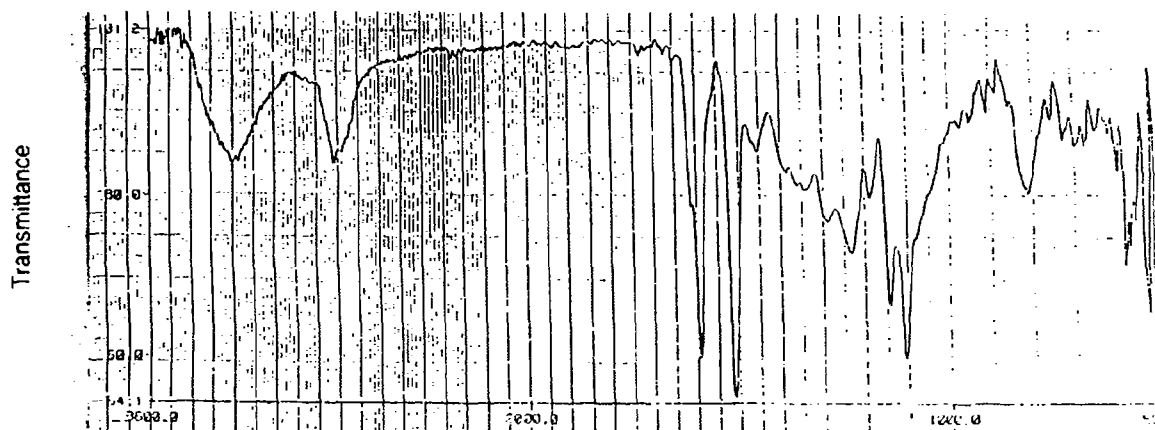


Figure 2-31. Through Transmission Ultrasonic (TTU) Scan of Component

2.5.4 Materials Characterization

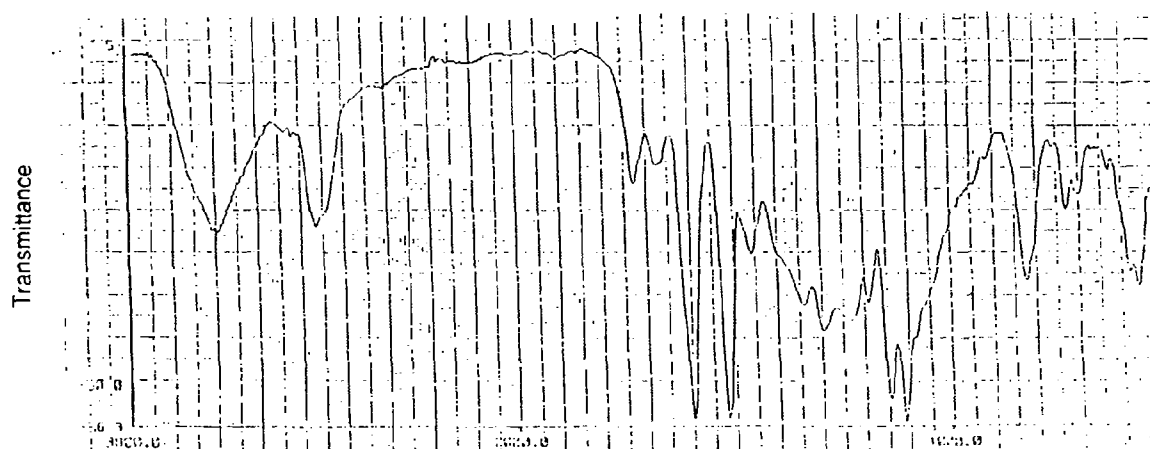
To characterize the material system, thermal/chemical analysis, electron microprobe analysis, and optical microscopy were performed.

A Fourier transform infrared (IR) spectrometer was used to determine the resin used to fabricate the component. Two samples from the panel were analyzed. Figure 2-32 shows the infrared (IR) spectrum obtained from the test sample. The general resin type was determined to be a 350°F cure conventional epoxy system by the method of fingerprinting using the limited in-house database of IR spectra. Figures 2-32b and c show the IR spectra of Hercules 3501-6 and Hexcel F263 prepreg materials respectively; these spectra were used for fingerprinting those obtained from the sample.



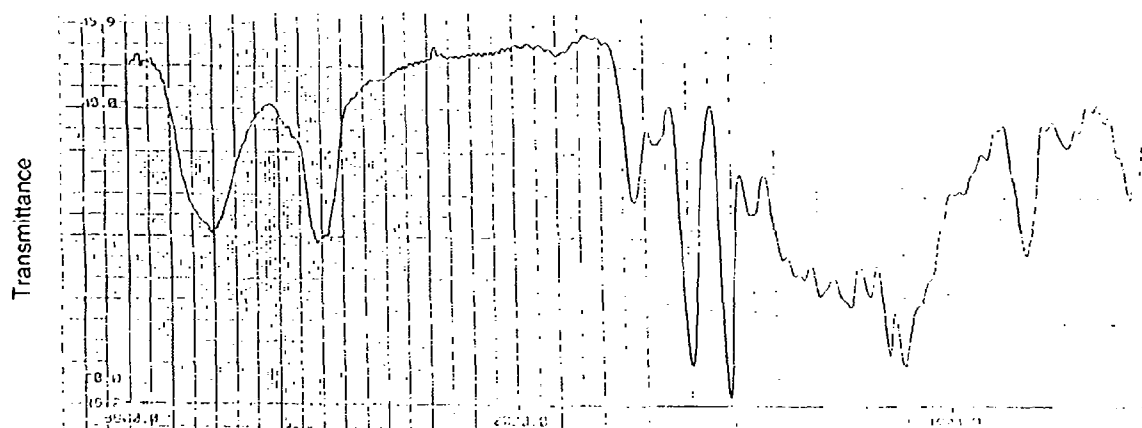
(a) Sample No. 1

Wavenumber



(b) Hercules 3501-6

Wavenumber



(c) Hexcel F263

Wavenumber

Figure 2-32. Infrared Spectroscopy Results

Differential scanning calorimetry (DSC) showed no exothermic peaks, indicating that the material was fully cured (Figure 2-33). A decomposition at 378°C was also observed. Thermomechanical analysis (TMA) showed the average glass transition temperature (T_g) to be 210°C (410°F, Figure 2-34). Thermogravimetric analysis (TGA) indicated the composite decomposed at approximately 357°C (675°F, Figure 2-35)

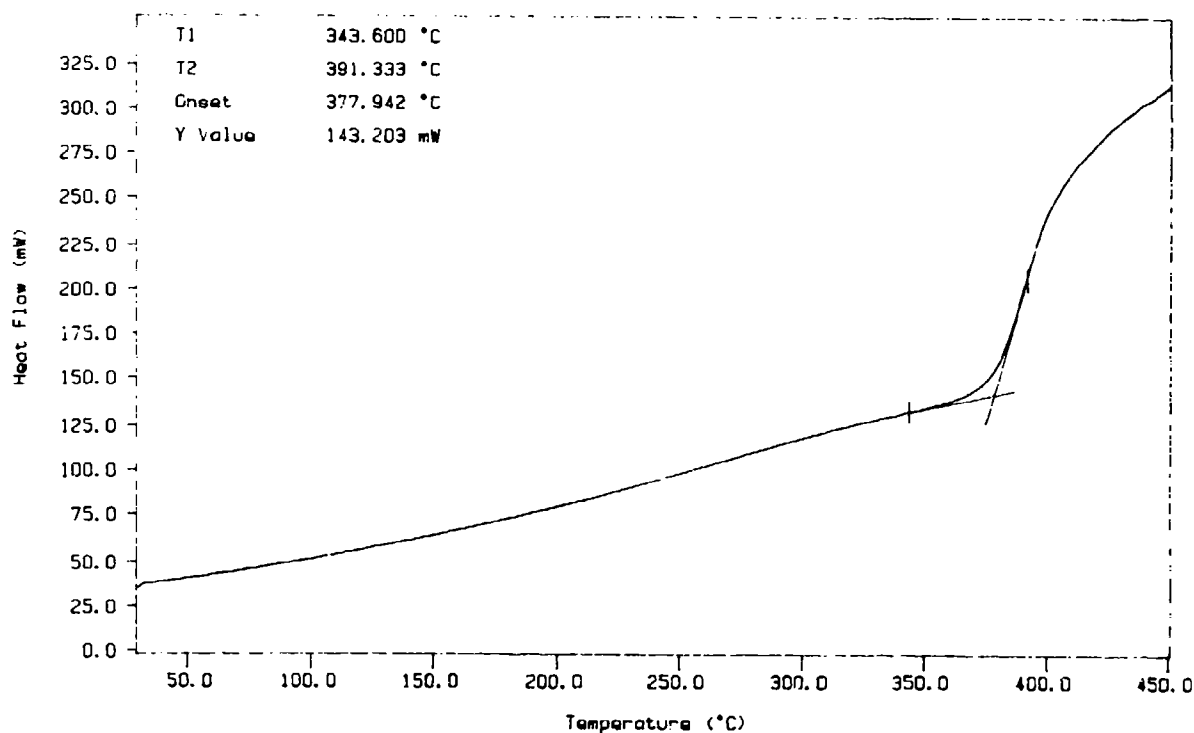
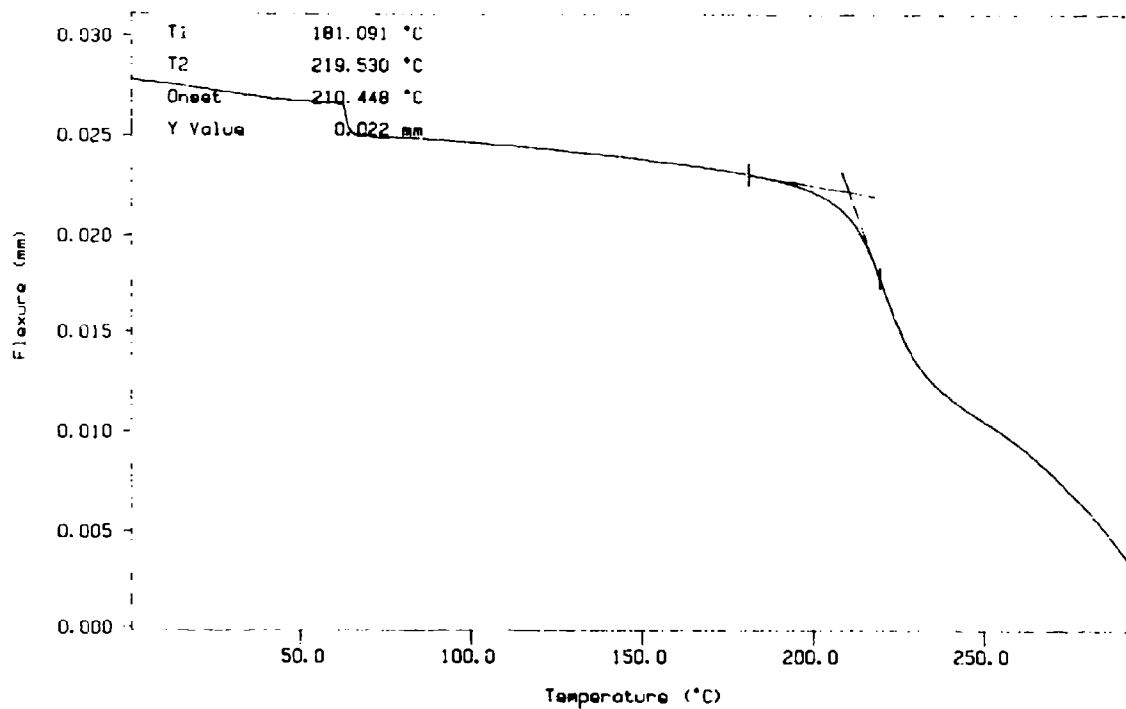


Figure 2-33. DSC Thermogram

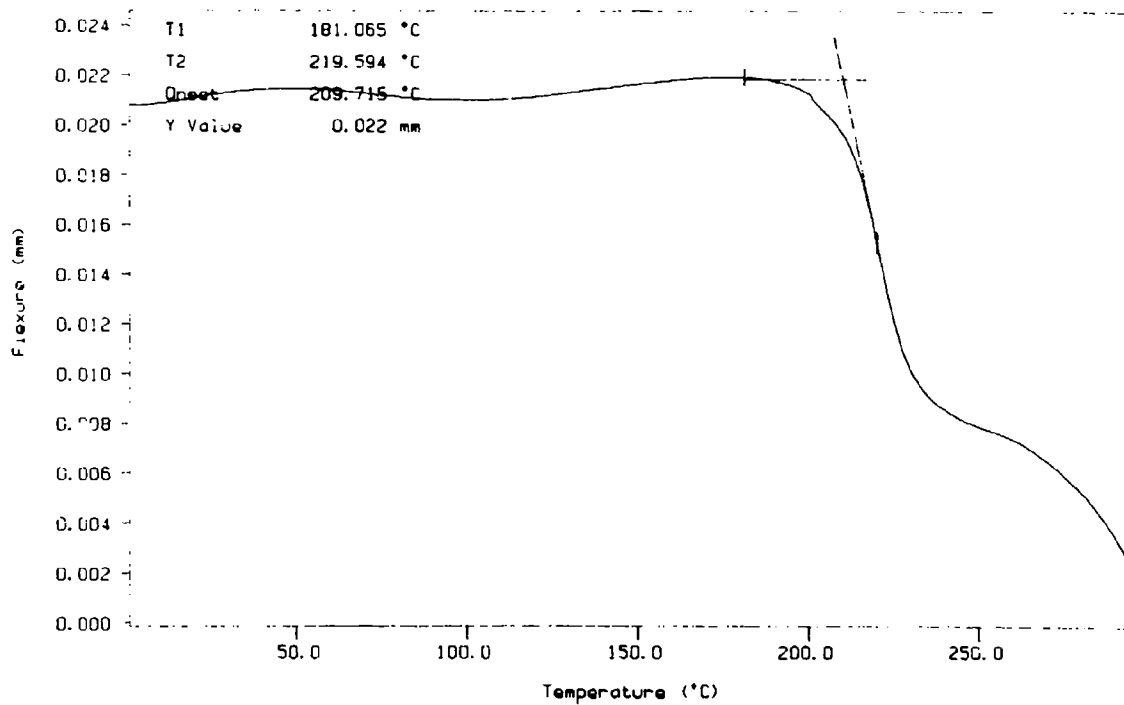
Acid digestion was performed using nitric acid to determine the resin content. The average weight percent of resin content (three samples) was 29.3 percent as shown in Table 2-2. Because of the lack of background information, it was impossible to tell whether the resin content was out of specification. However, from the fracture appearance it was determined that the resin content was not the primary cause of the fracture (since no major voids were observed near the fracture).

Figure 2-36 shows the wavelength dispersive X-ray (WDX) scan of the sample. The WDX scan indicated that the fiber used was carbon which is characterized by a $K\alpha$ peak at 44.700Å and 0.277 KeV. The WDX technique was used instead of EDX (energy dispersive X-ray) because WDX allows the detection of lighter elements such as carbon and oxygen.

Evaluation of an area away from the fracture showed that the quality of the laminate was good (with little porosity) and the ply stacking sequence was symmetrical (Figure 2-37). Due to the severity of the fiber damage near the apparent impact site, it was impossible to perform an evaluation of the cross-section.



a. TMA of sample 1 $T_g = 210.448^\circ\text{C}$



b. TMA of sample 2 $T_g = 209.715^\circ\text{C}$

Figure 2-34. TMA Thermograms Showing an Average Glass Transition Temperature of 210 °C

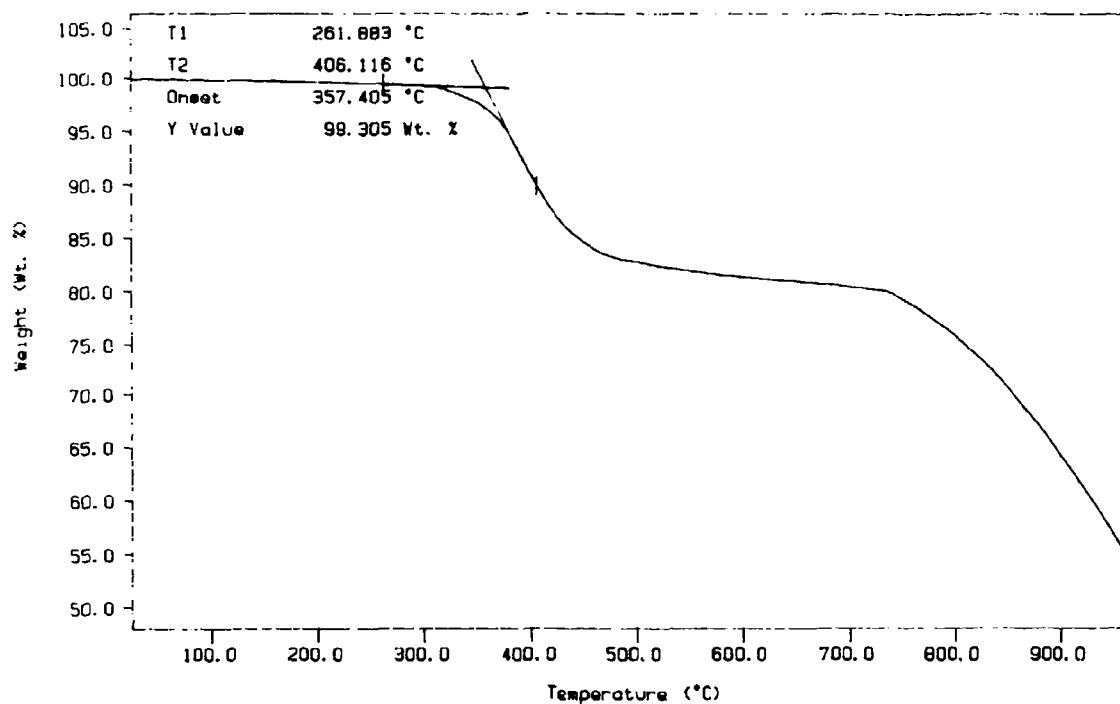


Figure 2-35. TGA Thermogram

Table 2-2. Resin Content Determined by Acid Digestion

Sample No.	Composite weight (grams)	Fiber weight (grams)	Resin content (% by weight)
A	1.6451	1.1691	28.9
B	1.3565	0.9571	29.4
C	1.7080	1.2028	29.6
Average:	1.5699	1.1097	29.3

2.5.5 Fractography

Fractography of this component was largely macroscopic. The damaged region resembled an area typically observed in an impact loaded structure. The fracture exhibited complex mixed-mode features involving both tension and shear. Further microscopic analysis was not performed because the macrofractography of the fractured panel provided sufficient evidence to determine the crack direction, fracture mode, and origin.

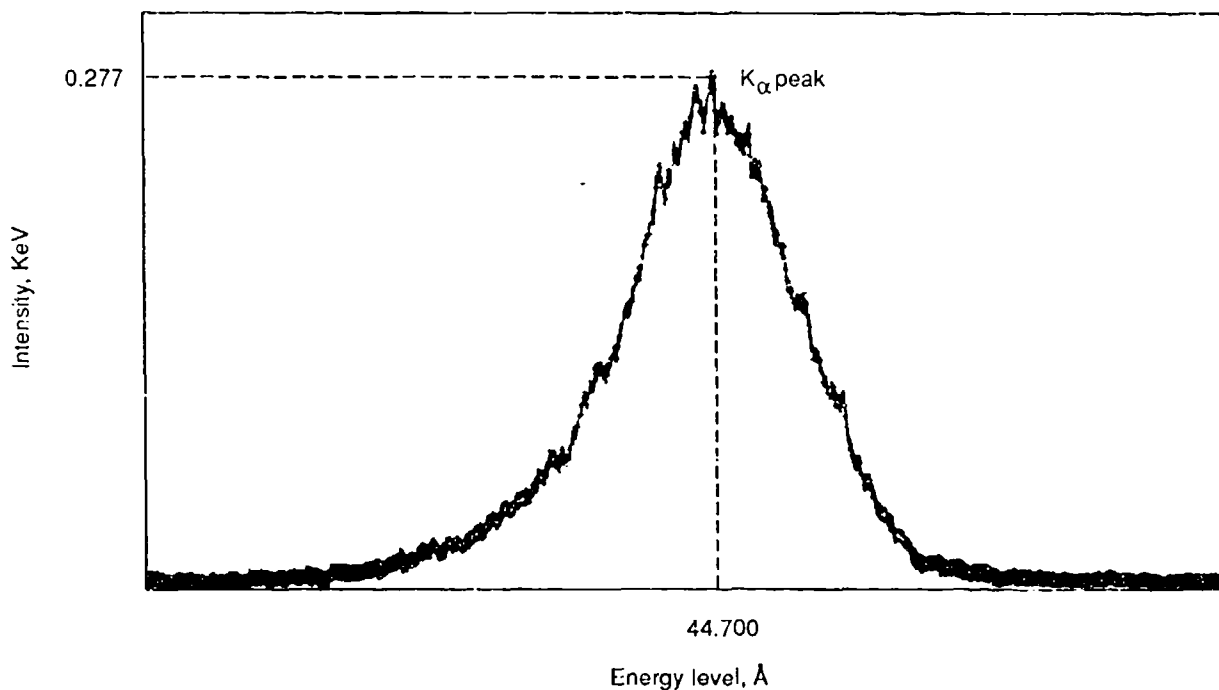


Figure 2-36. Wavelength Dispersive X-Ray (WDX) Scan of the Fiber

2.5.6 Stress Analysis

Stress analysis was performed in conjunction with visual examination to determine the state of loading of the fractured panel.

2.5.7 Summary

The fastener hole damage indicated that Region A of the test panel was subjected to tensile and shear loading. Region B showed no sign of damage suggesting that it was fixed to some type of structure. The major damage on the panel appeared to have been caused by impact loading in which a projectile penetrated through the panel from the interior surface. Materials characterization revealed that the resin system used in the fabrication of this component was a 350°F cure conventional epoxy system reinforced with carbon fibers. This material system exhibited an average resin content of 29.3 percent by weight and was fully cured.

The cross-sectional evaluation away from the fracture revealed that the laminate quality and its symmetrical stacking response were good; little porosity was found. Further microscopic analysis was not performed because the macrofractography of the fractured panel provided sufficient evidence to determine the crack direction, fracture mode and origin.

2.5.8 Conclusions/Recommendations

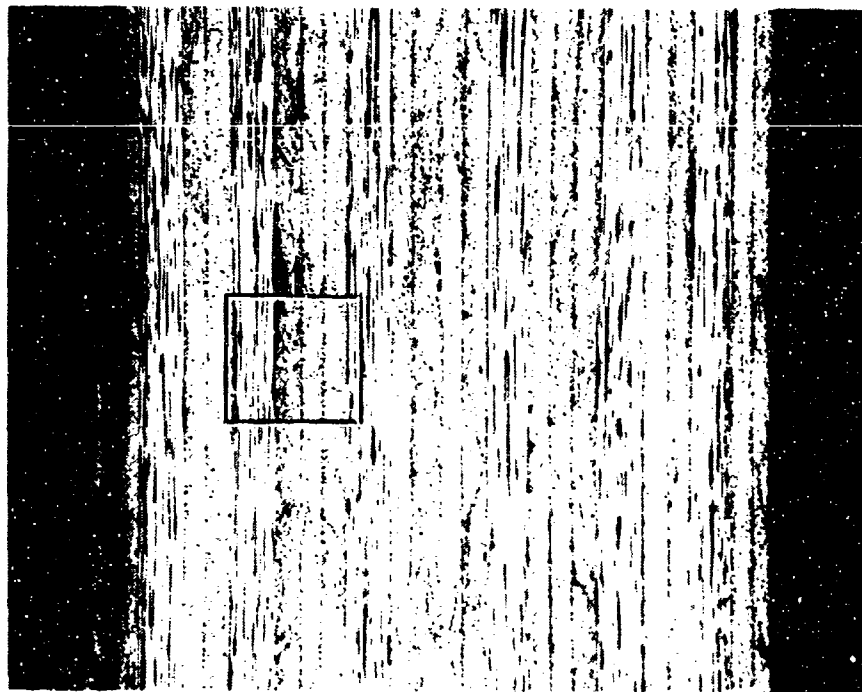
The fastener hole damage observed in certain locations on the test panel indicated that some of fasteners were not designed for the particular application. The fasteners on the end of Region A

Ply stacking
sequence:

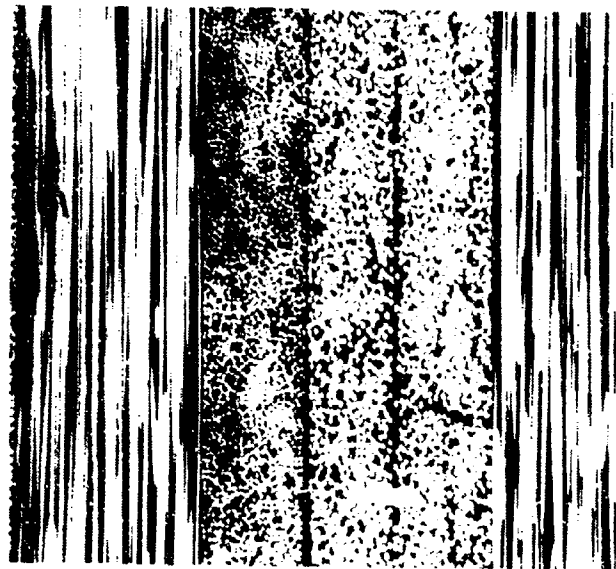
45
45
90
90
45
45
90
90
0
45
45
90
90
45
45

Total number
of plies is 30

S



25X



100X

Figure 2-37. Cross-Sectional View of the Panel

experienced a substantial amount of shear loading compared to the rest of the panel. The recommendation would be to examine the hole damage and make appropriate changes in the fasteners (i.e., change to shear or tension) to accommodate the load conditions experienced during the initial testing. Due to the fact that the mechanical test was unknown, recommendation for design improvement is difficult.

Material anomalies such as contamination or poor processing were not related to the cause of the fracture. The cause of fracture appeared to be impact loading due to the penetration of a projectile (see editorial note in Section 2.12.1).

2.6 FAILURE ANALYSIS OF A MAIN LANDING GEAR STRUT

Failure analysis of the strut was conducted by the General Electric Company.

2.6.1 Background History

The component was a Helio H-800 main landing gear strut, which had prematurely fractured at the wide end of the strut. The component was an E-glass/epoxy composite with a 0/90 layup. The strut was oriented on the aircraft approximately 40 degrees with respect to the vertical and was subjected to axial and shear stresses, as well as a bending moment, induced by the weight of the aircraft.

2.6.2 Visual Examination

The main fracture was located at the wide end of the strut at the point where the taper begins (see Figure 2-38). This translaminar fracture revealed both tensile and compressive fracture characteristics, typical of fracture under a bending load (Figures 2-39 and 2-40). Tensile fracture was indicated by multiplanar fracture with individual fibers or bundles observed, whereas compressive fracture was indicated by planar fracture. Translaminar fracture occurred at an angle such that it propagated through the boltholes on the lower surface and adjacent to the boltholes on the upper surface (see Figures 2-38 through 2-41). The edge of the aircraft mounting plate was located near the fracture location. The tensile and compressive portions of this fracture were consistent with the bending moment produced as installed in the aircraft (see Figure 2-42). Three separate delaminations were observed in this strut. One delamination was observed in the small piece at approximately the mid-thickness of the strut, between the tensile and compressive portions of the fracture (neutral axis). Two delaminations were observed on the large (long) piece which divided the strut thickness approximately into thirds.

2.6.3 Nondestructive Evaluation

Nondestructive evaluation was not performed on this component because the damage was considered to be readily apparent upon visual inspection.

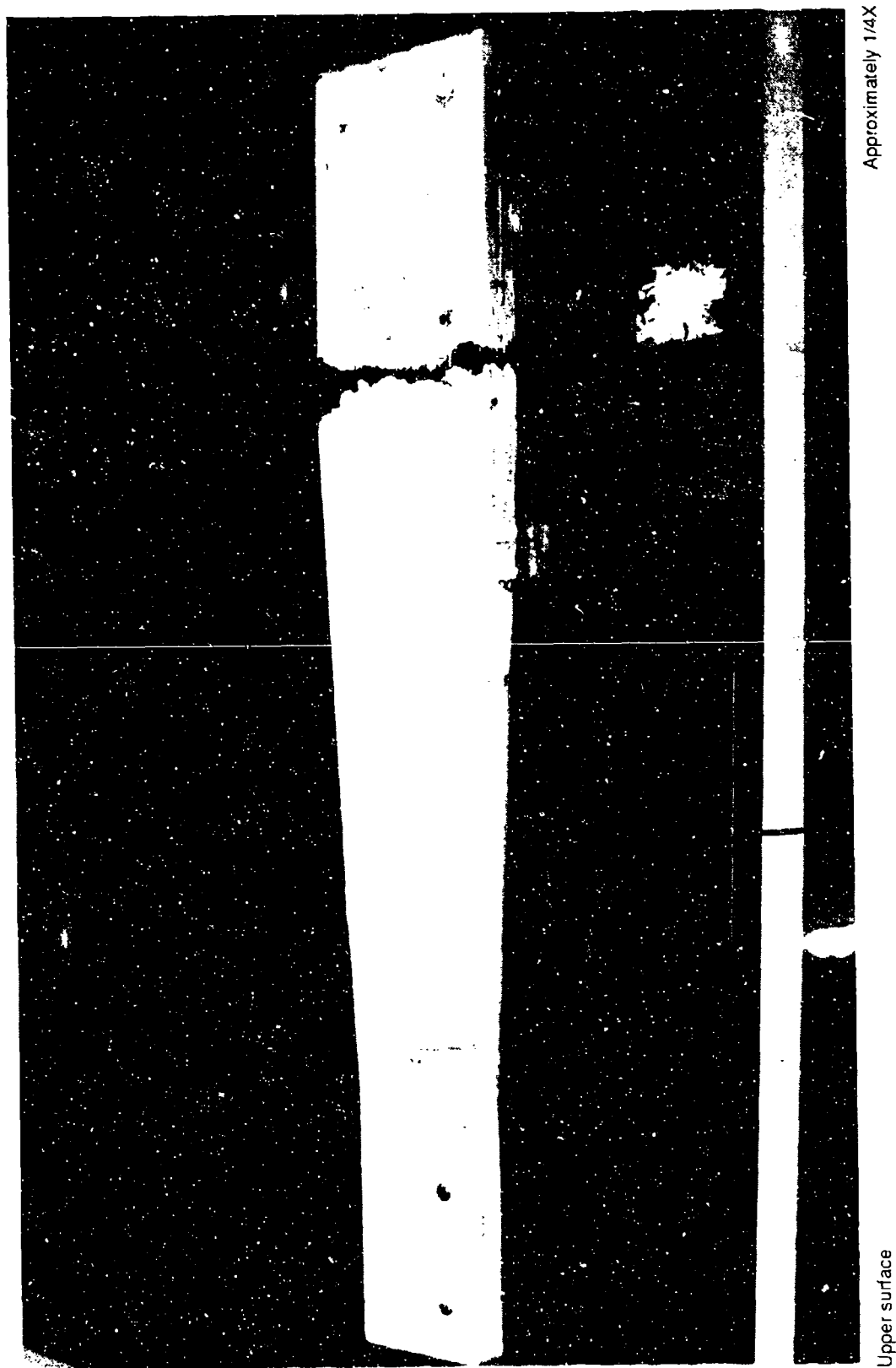
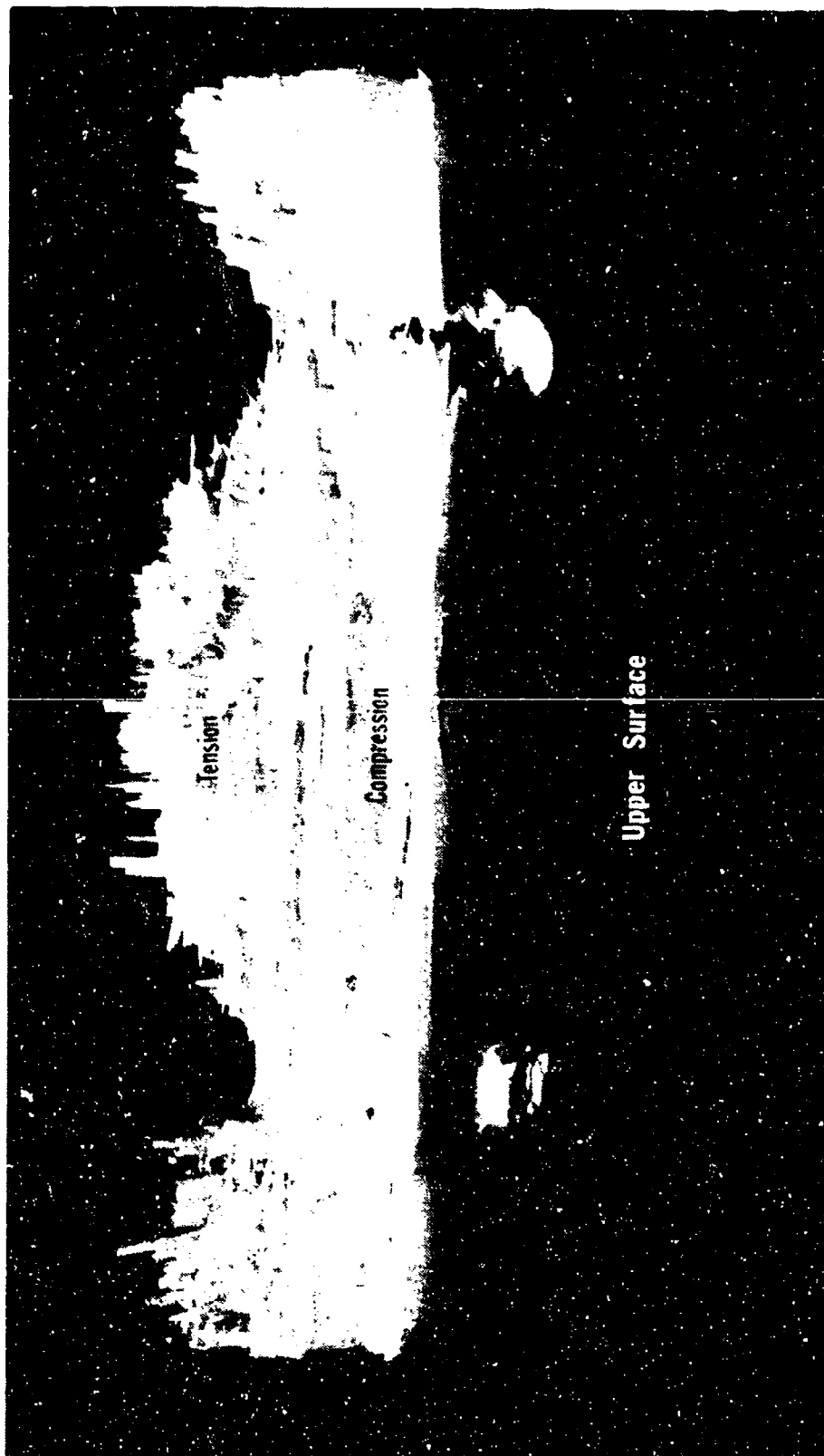


Figure 2-38. Macro photograph of the Upper Surface of the Landing Strut As-Received



Fracture surface--small piece

1:3X

Figure 2-39. Macro photograph of the Translaminar Fracture Surface on the Small (Fixed Piece) of the Strut
 Note: Tension fracture is multiphase and shows individual fibers or bundles; compression fracture is planar.

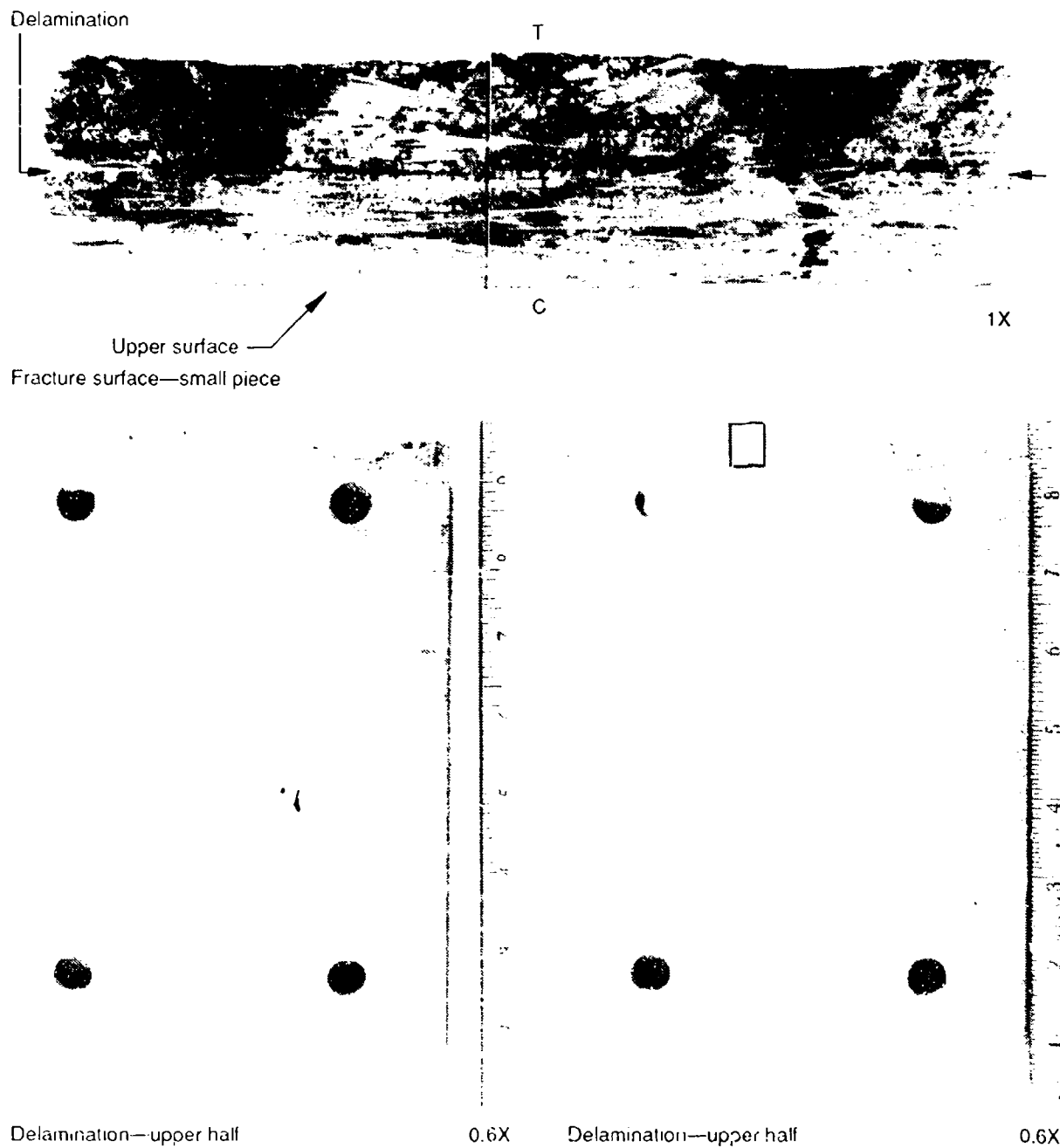
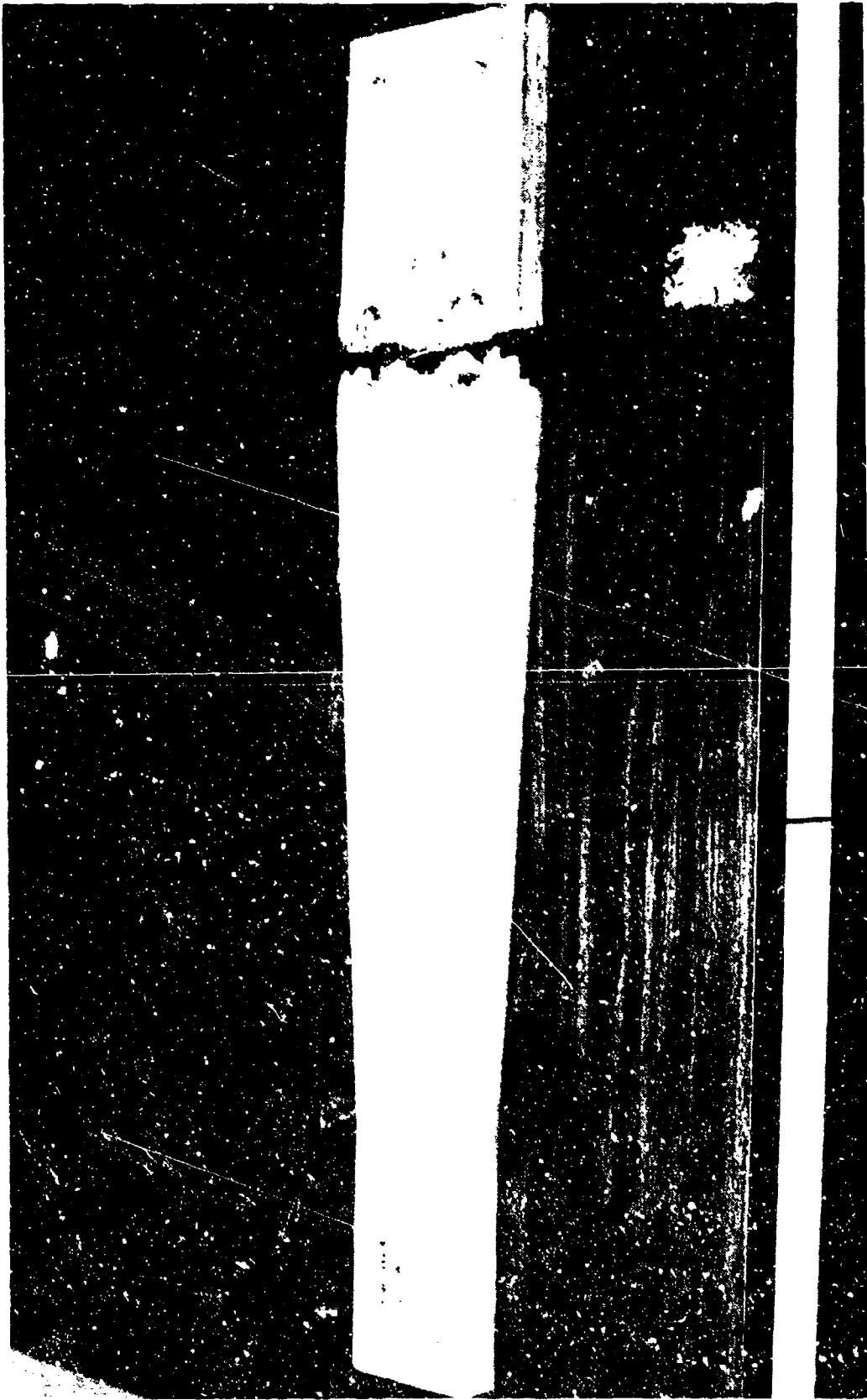


Figure 2-40. Macrophotographs of the Top of the Small Piece Fracture Surface Showing Delamination, Upper Surface, Tension Fracture (T) and Compression Fracture (C)

The lower macrophotographs show the mating delamination surfaces after laboratory separation of the delamination. The area shown by the small box is magnified in Figure 2-46.

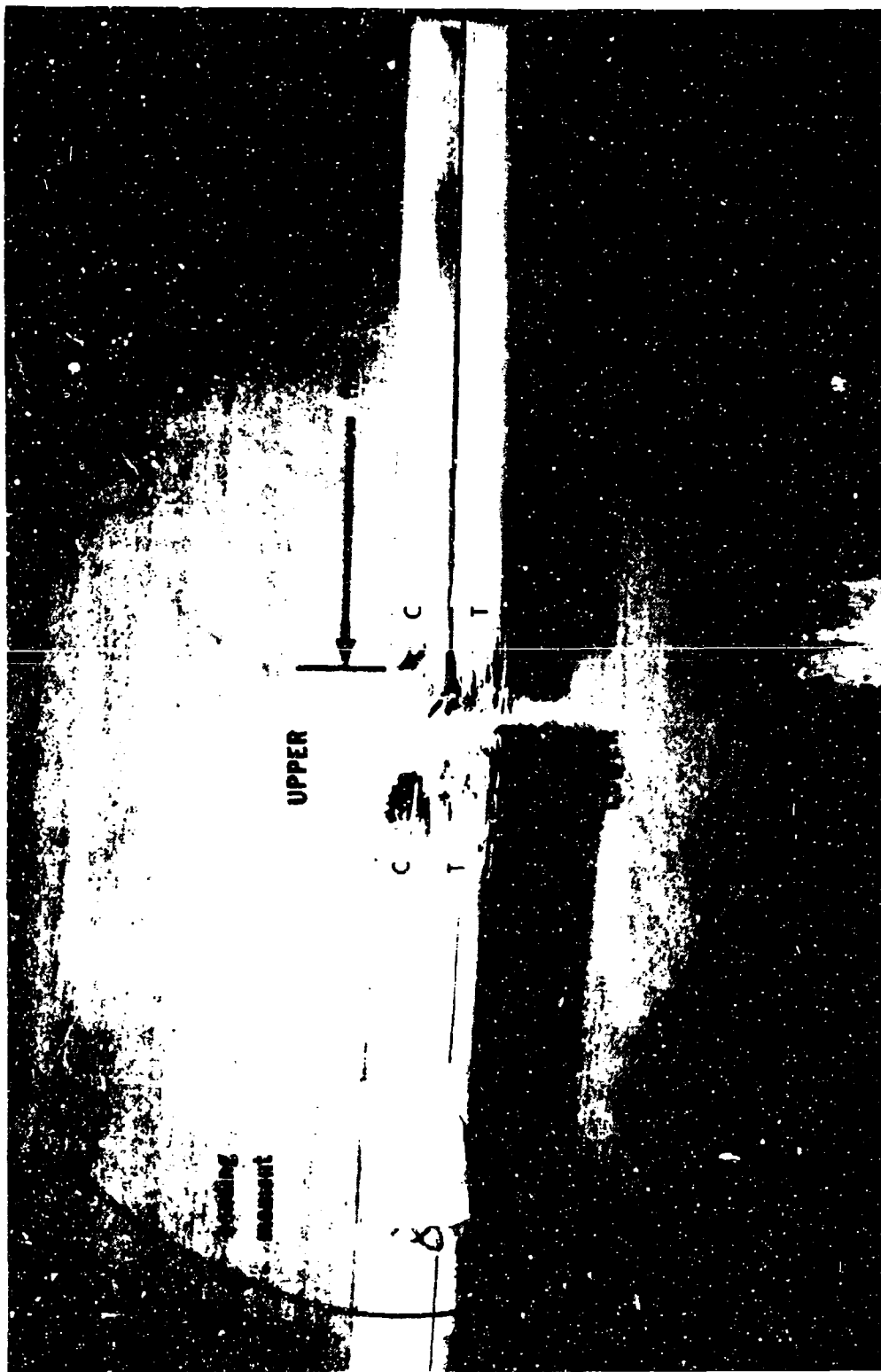


Lower surface

Approximately 1/4X

Figure 2-41. Macro photograph of the Lower Surface of the Strut As-Received

Note: The trans laminar fracture occurred at the bolt holes on the surface.



Side view—delaminations

0.6X

Figure 2-42. Macro photograph of Side of Strut Showing Delaminations

Neither portion of this strut was completely separated by delaminations. The figure shows the apparent loading conditions which led to failure. The loading moment was the greatest at the edge of the fixed portion of the strut, the failure location. As anticipated from this loading condition, the upper surface failed in compression (C) and the lower surface failed in tension (T).

2.6.4 Material Characterization

Nearly identical results were obtained from the glass transition temperature measurements by TMA and DSC (see Figure 2-43). These values were 133°C (271°F) and 135°C (275°F), respectively. These are typical values for a 121°C (250°F) epoxy resin. A metallographic section was taken through a bulged area (see Figures 2-44 and 2-45), found adjacent to a bolthole, which was apparently the result of constraint by the bolt. This section revealed microbuckling of fibers in a crack-like formation extending from the delamination toward the lower surface. Fiber and matrix details were difficult to discern from the prepared section, but the overall condition of the laminate appeared to be good.

2.6.5 Fractography

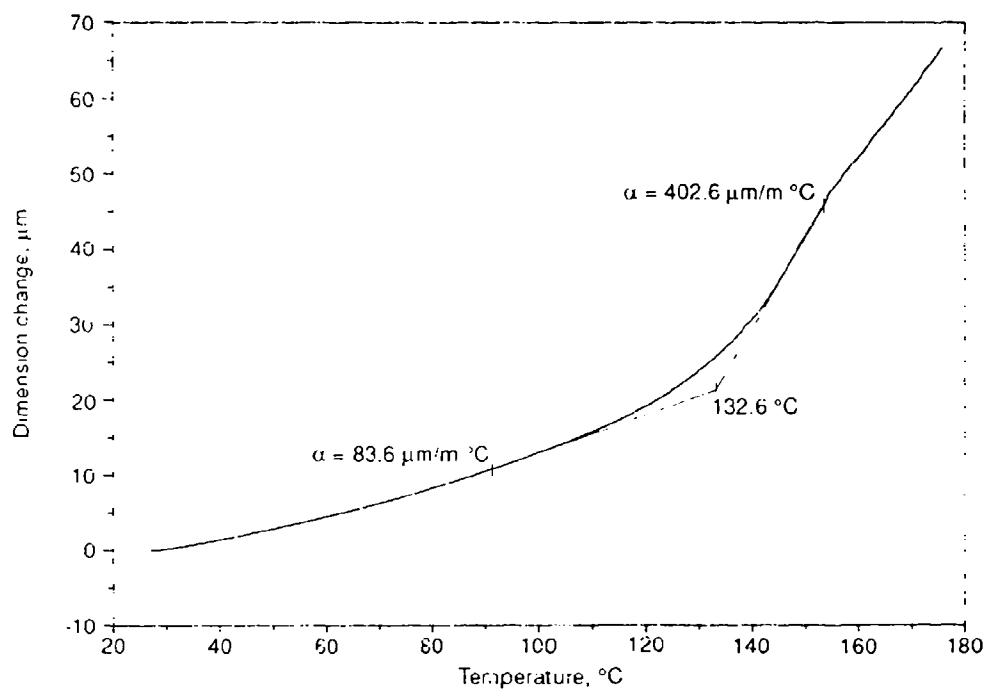
SEM examination was performed on the single delamination of the small piece. Evidence of shear fracture (scallop and hackles) was observed on the laboratory-exposed surface of this delamination (see Figures 2-46 and 2-47). The propagation direction was oriented axially along the length of the strut, but the exact direction could not be determined. Examination of the tensile half of the translaminar fracture revealed radial patterns on fiber end fractures (see Figure 2-48). The resultant direction of crack-propagation, determined by mapping the directions in which the lines radiate in the individual fiber fractures, was from the lower surface (tension) toward the delamination. Examination of the compressive half of the translaminar fracture revealed buckled fibers displaying chop marks (see Figure 2-49), typical of compressive failures. Although SEM examination of the translaminar fracture was conducted around the bolthole region, the non-conducting surfaces encountered produced images which were not of sufficient quality to include in this report. SEM examination of the translaminar fracture was difficult to perform, due to the extreme depth of this fracture. This prevented adequate application of gold (even after multiple sputter applications) to get a uniformly covered surface. Therefore, charging of uncoated areas during SEM examination made the location of suitably informative, fiber fractures difficult to perform.

2.6.6 Stress Analysis

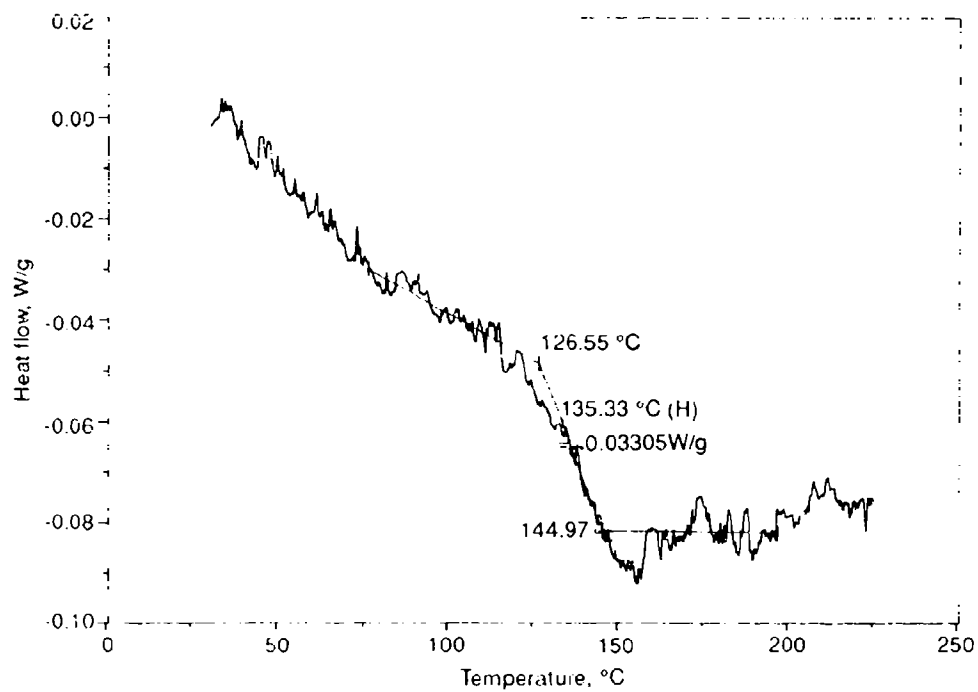
Preliminary stress analysis was performed in conjunction with visual examination to determine the state of loading of the strut.

2.6.7 Conclusions/Recommendations

All evidence observed during this investigation indicates failure of the strut due to a bending moment applied at the aircraft attachment plate (fracture location). The moment induced tensile and compressive fractures at the lower and upper surfaces, respectively, as well as the delaminations observed due to the acting shear plane. Since no material defects or anomalies were observed during this evaluation, the fracture apparently occurred due to overload, perhaps during hard landing. Due to the fact that tensile fiber radial patterns indicated propagation from the tensile surface toward the delaminations and since the observed delaminations are discontinuous, it is inferred that initiation of the translaminar fracture occurred prior to delamination.



(a) TMA



(b) DSC

Figure 2-43. TMA and DSC Thermograms of Strut

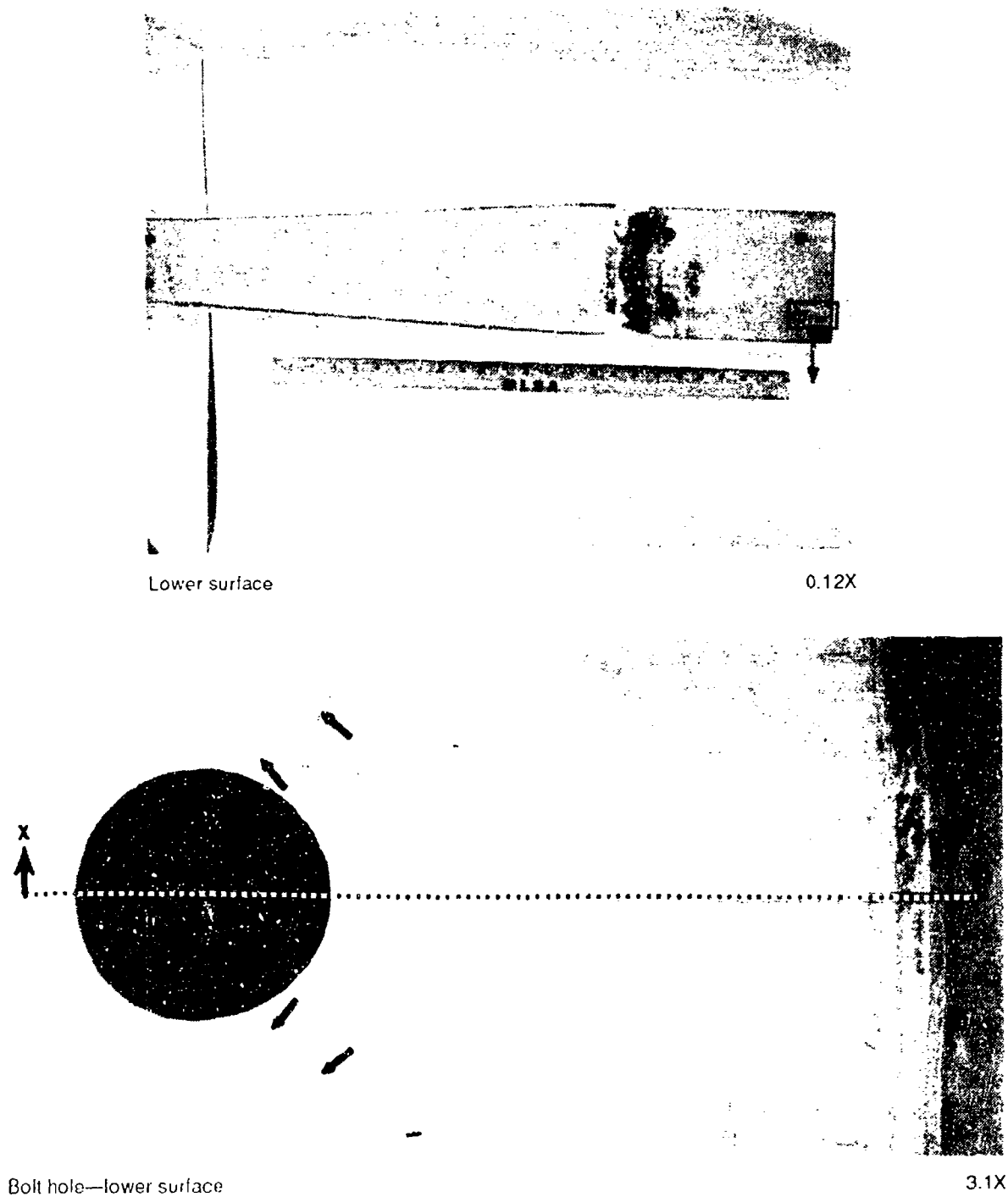
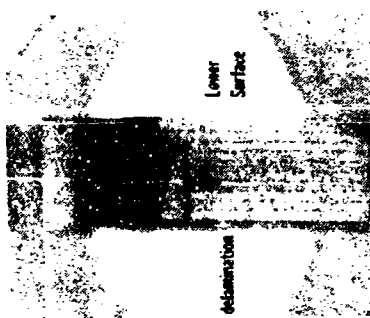


Figure 2-44. Macrophotographs of the Lower Surface of Strut

The figure shows the location and the orientation of section X X, magnified in Figure 2-45. The local bulging at the end of the strut (emphasized by the segmented line) occurred as a result of a restraint from the bolt. Cracks labeled by the small arrows were also generated by this loading condition.



Section X-X 15X

A



Section X-X

B

40X

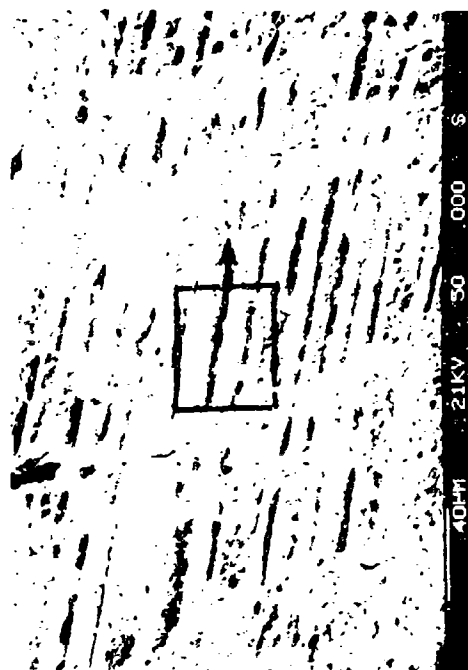
Figure 2-45. Macrophotograph (A) and Photomicrograph (B) of Section X-X Taken Through the Bolt Hole and End

The segmented black lines outline a region of fiber microbuckling damage induced by the local restraint of the bolt on this side of the bolt hole.

The delamination and bolt hole surfaces of this section are outlined by the segmented dashed lines.



Delamination—50 degree tilt 11X



50 degree tilt 375X

Legend: S scallop



50 degree tilt 2,000X

Figure 2-46. SEM Fractographs of Delamination at the Translaminar Fracture Surface of the Small Piece
Scallops indicate shear fracture. The orientation of these scallops indicates propagation of the delamination axially along the strut.



Delamination—50 degree tilt 400X



Delamination—50 degree tilt 400X

Legend: H hackle



50 degree tilt 2,000X



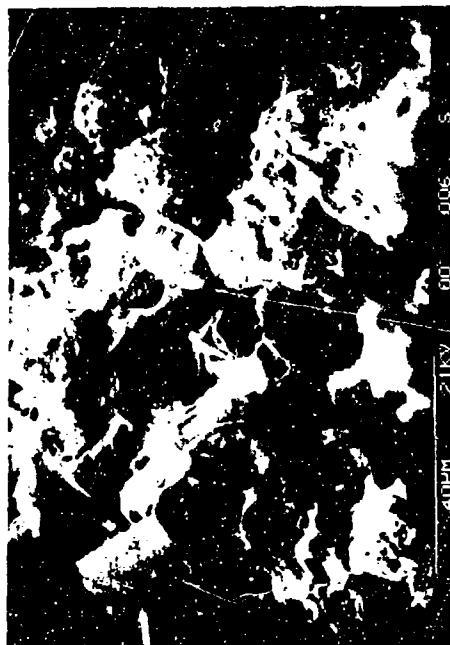
50 degree tilt 2,000X

Figure 2-47. SEM Fractographs of Delamination Adjacent to Translaminar Fracture
Hackles indicate shear fracture and propagation of the delamination axially along the strut.



Tensile fracture—0 degree tilt 975X

Delamination
 ↑
 ↓
 Lower surface



0 degree tilt 950X



0 degree tilt 1000X

Figure 2-48. SEM Fractographs of the Tensile Half of the Translaminar Fracture Surface

Small arrows show crack propagation direction indicated by individual fiber end fractures. The overall crack propagation direction indicated by these fibers is toward the delamination from the lower (tensile) surface.



Compressive fracture—0 degree tilt

400X

0 degree tilt



1,400X

Legend:

- C compression
- T tension

Upper surface



Delamination

Figure 2-49. SEM Fractographs of the Compressive Half of the Translaminar Fracture
 These fractographs exhibit compressively loaded fiber fractures, as indicated by the presence of both tensile and compressive fracture morphology.

More specific conclusions could be drawn concerning the loading of this component during fracture if some record of aircraft/component field service had been provided. Although this information was not provided, indication of some field service of this component was observed in the distortion at the boltholes (see editorial note in Section 2.12.2).

2.7 FAILURE ANALYSIS OF A VERTICAL RUDDER

2.7.1 Abstract

Failure analysis was performed by Northrop Corporation on a vertical stabilizer assembly that had failed during repair. The failure analysis logic network (FALN) was used to determine the failure location, and to establish the cause for failure of the part. It was determined that failure occurred due to blown core caused by an attempt to repair the rudder with moisture in the honeycomb.

2.7.2 Background

Two rudder assemblies, identified as P/N 76301-68G240001-1003 and P/N 68A240001-1013, A221070 were submitted to Northrop by the Air Force for evaluation. The parts were reported to be stabilizers from F-15 aircraft, and one of the parts reportedly had failed during repair. The service records or flight histories of the components were unavailable. To assist in the investigation, engineering drawings showing the details of the parts were provided by the Air Force.

2.7.3 Analysis of Failure

Figure 2-50 shows the FALN used to perform the investigation. The sequence consisted of initial visual examination and macroscopic documentation of the part, followed by NDE evaluation to establish the failure regions. The fracture regions associated with the failure were revealed by ply sectioning to expose fracture surfaces. Scanning electron microscope (SEM) examination was carried out on the fracture surfaces to establish the fracture mode. Based on the results, additional NDE tests were determined to be necessary. This was followed by material testing (QC tests), with final engineering analysis to establish the cause for failure.

2.7.3.1 Visual Examination

Initial examination of the parts in the as-received condition showed that the rudder labeled P/N 76301-68G240001-1003 was relatively intact, whereas P/N 68A240001-1013, A221070 was the part that had been repaired. Further testing was accordingly concentrated on the latter part. Figure 2-51 shows photographs of the repaired part in the as-received condition. As shown, one of the skins (arbitrarily labeled as the inboard side) had a repair patch close to the leading edge of the assembly. The outboard skin had a localized region of damage as determined by simple coin tap tests, in a region immediately opposite the patch.

Steps Used In Failure Analysis

- ① Visual Examination and Macroscopic Documentation of Part
- ② AUSS C-Scan of Part For Damage Locations
- ③ 2-D, 3-D UT-Scans For Detail In Damage Areas
- ④ Ply-Sectioning To Expose Fracture In Failed Areas
- ⑤ SEM Fractography
- ⑥ X-Ray of Core
- ⑦ QC Tests
- ⑧ Analysis of Results



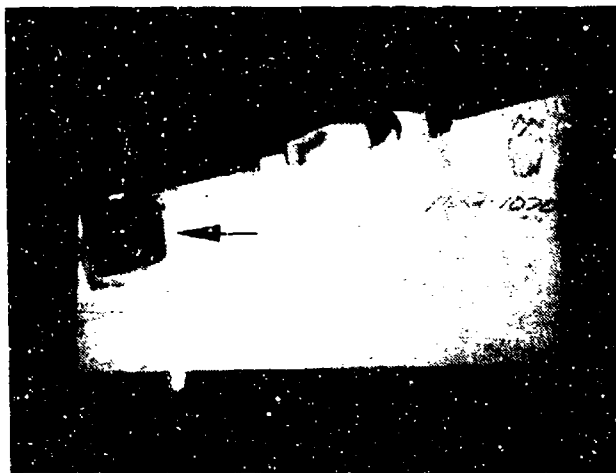
Cause For Failure

Figure 2-50. FALN Sequence Used in Investigation of Rudder Failure

2.7.3.2 Ultrasonic Testing of Rudder Assembly

Initial nondestructive testing of the rudder consisted of conventional through-transmission ultrasonic (TTU) testing of the assembly. Figure 2-52 is a photograph showing a composite of the TTU plot. C-scan testing revealed indications in the outboard skin close to the leading edge.

Detailed 2-D and 3-D pulse echo ultrasonic imaging was concentrated on the repair and the outboard skin in the area associated with C-scan ultrasonic indications. Figure 2-53 shows a B-scan of the repair on the inboard skin. No disbonds or delaminations could be detected in the repaired area. Figure 2-54 shows 2-D and 3-D pulse-echo images of the damaged region in the outboard skin. As shown in Figure 2-54a and 2-54b, damage in the outboard skin consisted of a large circular delamination approximately 5 inches in diameter and at a distance of $2/3t$ (t = skin thickness) from the top surface. In addition, as shown in Figure 2-54, there were two smaller delaminations closer to the top surface, and extensive porosity in the damaged region.



(a)



(b)

Figure 2-51. As-Received Photographs of Rudder

(a) Inboard Side

Note patch at arrow

(b) Outboard Side

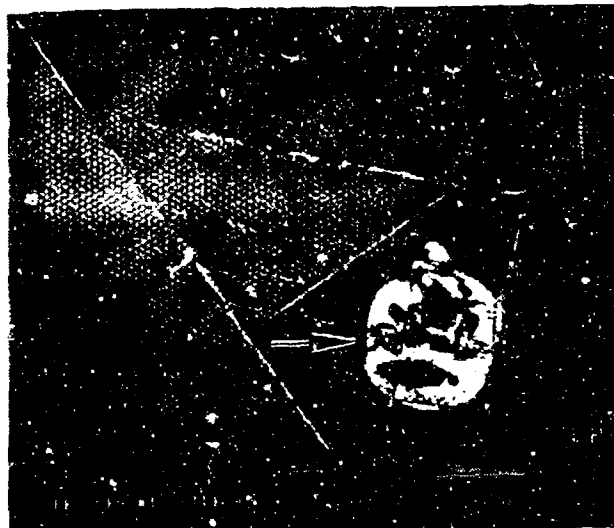
Note damage at arrows



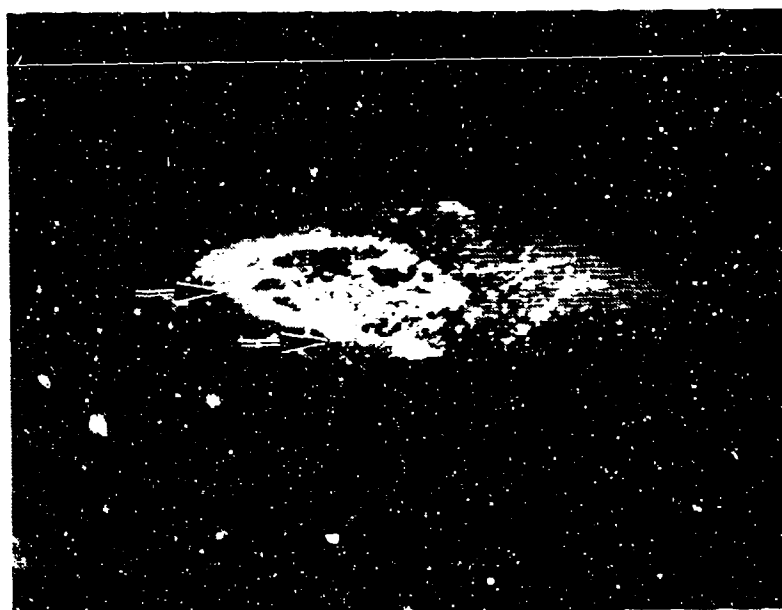
Figure 2-52. Composite TTU Plot of Rudder



Figure 2-53. B-Scan of Repair Region on Inboard Skin
Note: Crustiness in repaired area



(a)



(b)

Figure 2-54. Pulse Echo Images of Damaged Region
 (a) 2-D B-Scan Shows Primary Delamination (Arrow)
 (b) 3-D B-Scan Shows Multiple Delaminations (Arrows) and Porosity

2.7.3.3 Fractographic Examination

In order to perform fractographic examination, a rectangular coupon was sectioned from the rudder containing the damaged region in the outboard skin, and the repaired region in the inboard skin. The coupon was obtained by sectioning the rudder well away from the regions of interest using a flood-cooled carbide saw. The defect surface associated with the primary delamination was exposed by means of a controlled saw cut and gentle peel loads in the laboratory. Figure 2-55 shows macrophotographs of the coupon after exposing the fracture. As shown in Figure 2-55a and 2-55b, the fracture surface associated with the delamination was highly reflective and had a colored ridge of epoxy traversing the surface, approximately 3 inches away from the center of the delamination. Also of interest was the observation that the damage indications were not due to core disbond (see Figure 2-55c).

Figures 2-56 and 2-57 show SEM photographs of fracture features observed in the delamination region and in regions adjacent to the delamination. In the region of the delamination, the fracture surface exhibited a "resin-starved" condition, with very little evidence of fracture. As shown in Figure 2-56, stray hackles could be observed; however these were associated with very fine porosity. The epoxy ridge shown in Figure 2-55 was also associated with fine porosity (see Figure 2-57b). The laboratory fracture regions, in contrast, were associated with peel fracture characteristics in the form of river patterns in fractured epoxy (Figure 2-57c).

In summary, SEM examination indicated:

1. Very little evidence of fracture in the defect region
2. The defect appeared resin-starved and associated with extensive porosity
3. Laboratory overload occurred by peel.

2.7.3.4 Porosity

The occurrence of porosity in the defect was considered unusual and suggested that it may have occurred prior to the delamination event. Consequently, X-ray examination was carried out on the rudder assembly. Radiographic examination revealed a "blown-core" condition in the rudder as is illustrated in Figure 2-58.

2.7.3.5 Microstructure

Limited cross-sections of the rudder were examined using materialographic sectioning techniques. Figure 2-59 presents the typical microstructural features observed in the outboard skin. No abnormalities were noted in the cross-section other than porosity. The boron/epoxy (B/Ep) plies and glass tracers appeared to be in accordance with the call-outs in the drawings provided.

2.7.4 Summary

The occurrence of a blown core condition indicated that moisture had played a role in the failure event. It was concluded that failure occurred when repair was attempted with wet core. During repair, the moisture turned into steam, and caused localized delaminations in the outboard skin.

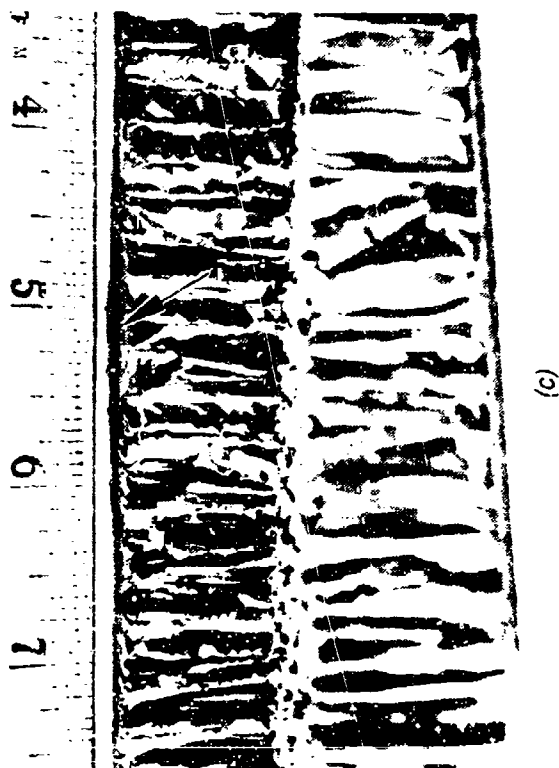
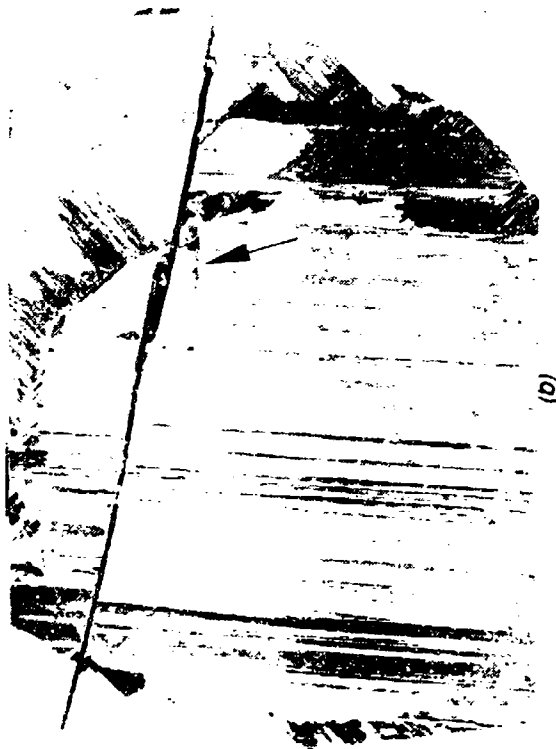


Figure 2-55. Macrophotographs of Delamination Fracture in Coupon From Damaged Area

(a) Bottom View of Top Skin

Note epoxy ridge in delamination (at arrow)

(b) Top View of Core

Note epoxy ridge in delamination (at arrow)

(c) Lateral View of Assembly Showing Absence of Core Disbond

Note damage (at arrow)

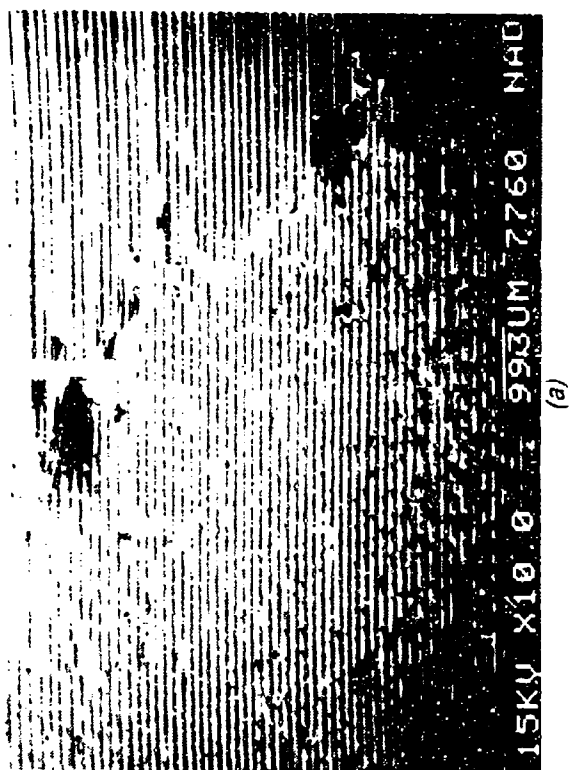


Figure 2-56. SEM Photographs of Delaminated Surface
 (a) Low Magnification
 (b) Intermediate Magnification Showing
 Resin-Starved Condition (Arrow)
 (c) High Magnification Showing Porosity (Arrow)

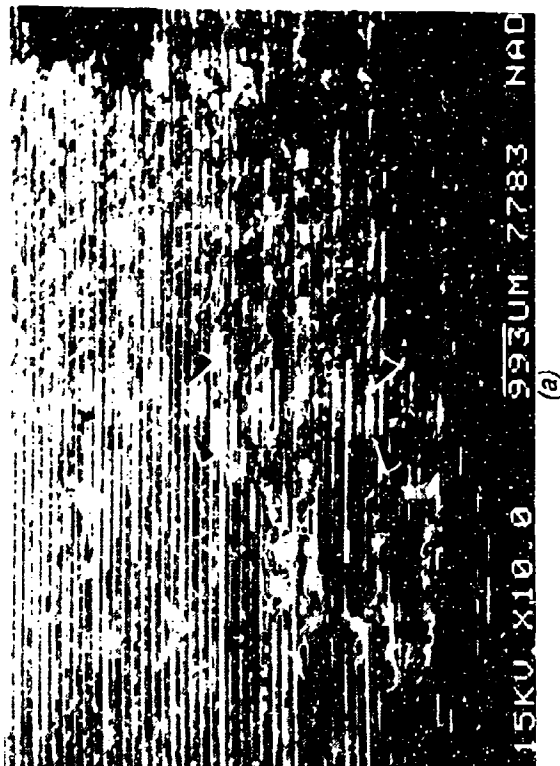
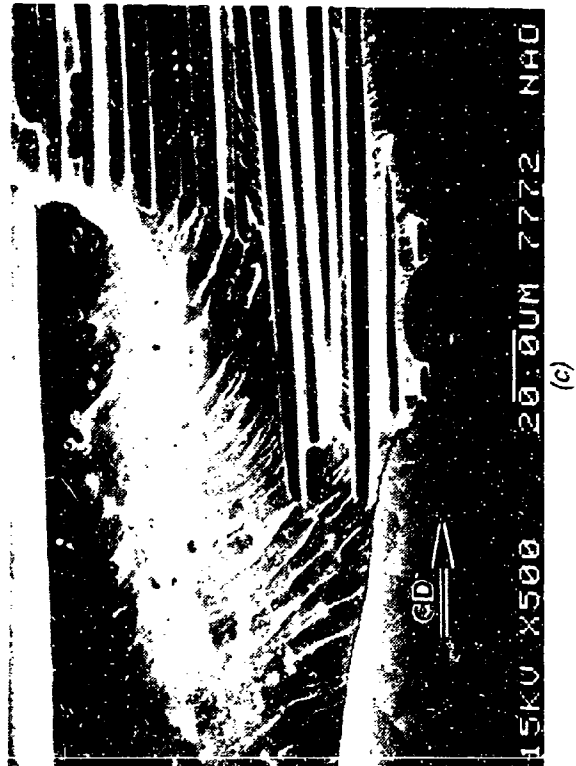


Figure 2-57. SEM Photographs Showing Fracture Details in Delamination
 (a) Low Magnification Showing Epoxy Ridge (Arrows)
 (b) Porosity in Epoxy Ridge (Arrow)
 (c) Peel Fracture in Laboratory Overload Region

CD = Crack-propagation direction



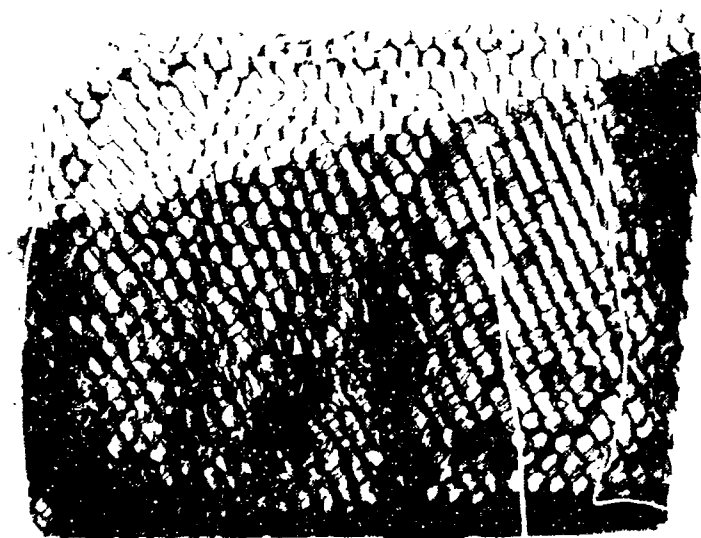


Figure 2-58. X-Ray Radiograph Shows Blown-Core in Rudder

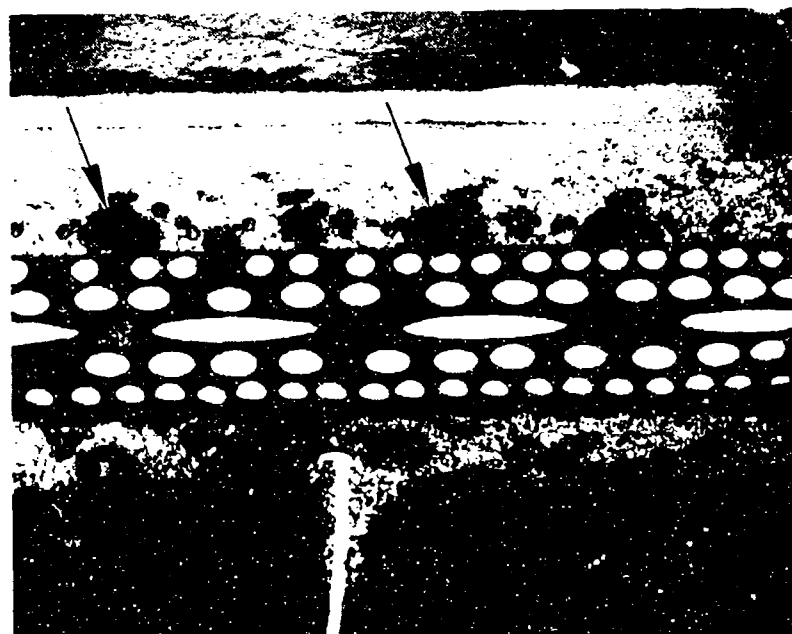


Figure 2-59. Photograph of Cross-Section Taken Through Rudder Skin
 Note Porosity in Skin at Arrows

2.8 FAILURE ANALYSIS OF A HORIZONTAL STABILIZER TORQUE BOX ASSEMBLY

2.8.1 Abstract

Failure analysis was performed by Northrop Corporation on a horizontal stabilizer torque box assembly that had failed. The failure analysis logic network (FALN) was used to determine the failure location, and to establish the cause for failure of the part. It was determined that failure occurred due to impact damage.

2.8.2 Background

Two horizontal stabilizers, identified as P/N 7630168A89G054-2003 and P/N 7630168A210053-1015 were submitted to Northrop by the the Air Force for evaluation. The parts were reported to be from F-15 aircraft. No service records or flight histories of the components were available.

2.8.3 Analysis of Failure

Figure 2-60 shows the FALN used to perform the investigation. The sequence consisted of initial visual examination and macroscopic documentation of the part, followed by NDE evaluation to establish the failure regions. Based on initial NDE tests, one of the two parts was selected for more detailed evaluation. This part was subjected to extensive NDE tests to reveal damage locations. The fracture regions associated with the failure were revealed by ply sectioning to expose fracture surfaces. Scanning electron microscopic (SEM) examination was carried out on the fracture surfaces to establish the fracture mode. Based on the results obtained, the cause for failure was established.

2.8.3.1 Visual Examination

Figure 2-61 shows photographs of the parts in the as-received condition. P/N 7630168A89G054-2003 (hereafter referred to as stabilizer #1) had the outboard tip missing (Figure 2-61a), whereas P/N 7630168A210053-1015 (hereafter referred to as stabilizer #2) had extensive damage on the outboard flight surface (Figure 2-61b). The overall appearance of damage on stabilizer #1 suggested that the damage may have been a post-failure event. The appearance of the outboard skin damage on stabilizer #2 suggested foreign object or impact damage. Based on discussions with the Air Force, further evaluation was concentrated on stabilizer #2.

2.8.3.2 Ultrasonic Testing of Stabilizer Assembly

Initial nondestructive testing of the part consisted of conventional through-transmission ultrasonic (TTU) C-scan testing of the assembly. Figure 2-62 shows photographs of the C-scan plots. Damage in stabilizer #2 consisted of two zones, 1) damage at the outboard end of the stabilizer adjacent to the trailing edge (Figure 2-62a), and 2) mid-section damage extending approximately 9 inches span-wise, and approximately 10 inches chord-wise, starting from the trailing edge (Figure 2-62b).

Steps Used In Failure Analysis

- ❶ Visual Examination and Macroscopic Documentation of Parts
- ❷ AUSS C-Scans of Parts For Damage Locations
- ❸ Selection of Component For Failure Analysis
- ❹ 2-D, 3-D UT-Scans For Detail In Damage Areas
- ❺ Ply-Sectioning To Expose Fracture In Failed Areas
- ❻ SEM Fractography
- ❼ Analysis of Results



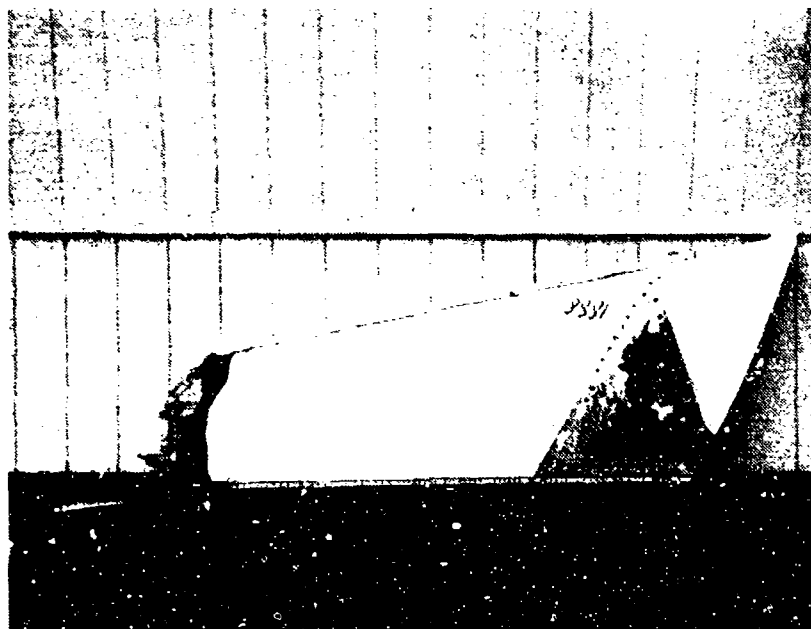
Cause For Failure

Figure 2-60. FALN Sequence Used to Evaluate Horizontal Stabilizer Torque Box Assembly Failure

Detailed 2-D and 3-D pulse echo ultrasonic imaging was concentrated on these two zones of damage. Figure 2-63 shows pulse-echo images of the damage at the outboard end. Orthogonal cross-sections of the 2-D image (Figure 2-63a) revealed that the damage in this zone (hereafter referred to as zone A) consisted of two principal regions of delamination (Figure 2-63b) with one close to the outer skin, and the second closer to the back face of the skin. Damage in the mid-section location (hereafter referred to as zone B) started at or very close to the top face, and extended across the flight surface and into the interior (Figure 2-64).

2.8.3.3 Fractographic Examination

Guided by the NDE tests, sections were excised from the stabilizer for detailed fractographic examination. Two rectangular coupons were sectioned from the stabilizer containing the damaged regions. The coupons were obtained by sectioning well away from the regions of interest using a flood-cooled carbide saw. The defect fracture surfaces associated with zones A and B were exposed by means of controlled saw cuts and gentle lifting of the delaminated layers.

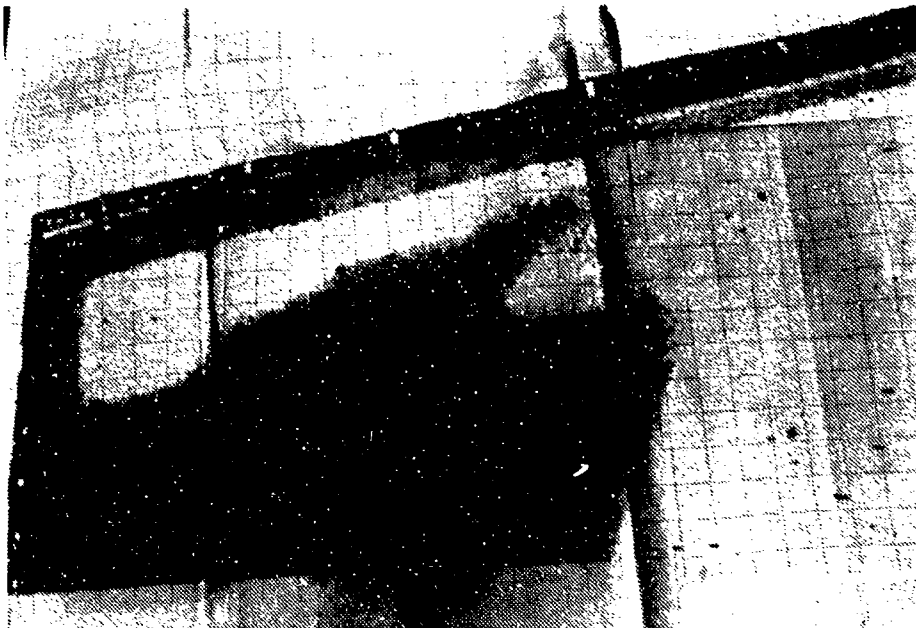


(a)



(b)

Figure 2-61. As-Received Photographs of Horizontal Stabilizers
 (a) Outboard Tip Missing on Stabilizer #1, P/N 7630168A890054-2003
 (b) Skin Damage on Stabilizer #2, P/N 7630168A210053-1015
 Note damaged zones A and B



(a)

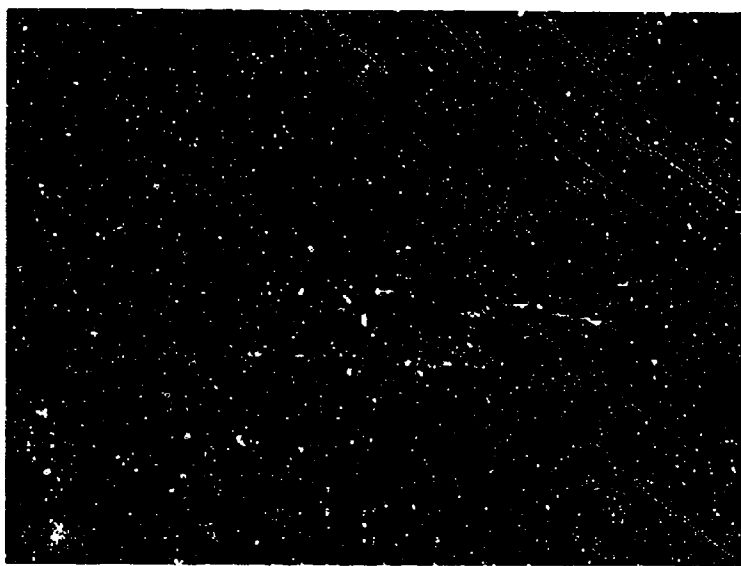


(b)

Figure 2-62. TTJ C-Scans of Horizontal Stabilizer
 (a) Damage on Outboard Location Near Trailing Edge (Zone A in Figure 2-61b)
 (b) Mid-Spar Damage (Zone B in Figure 2-61b)



(a)



(b)

Figure 2-63. Pulse-Echo Images of Damage at the Outboard End of the Stabilizer (Zone A)
 (a) 2-D Image Showing Delamination
 (b) Orthogonal Section Showing Two Zones of Delamination



(a)



(b)

Figure 2-64 Pulse-Echo Images of Damage at the Mid-Section of the Stabilizer (Zone B)
(a) 2-D Image
(b) 3-D Image

Figure 2-65 shows macrophotographs of damage in zone A. Figure 2-65a shows the fracture with the outer (top) ply of the skin removed. Several features were of interest. The overall fracture had a shiny appearance, with extensive occurrence of rubble. The laminate surface had a wrinkled appearance, and this was determined to be due to localized buckling of plies (see Figure 2-65a). Figures 2-65b and 2-65c show photographs of the defect surface with the second and third plies removed. It was determined that in each layer there was a fan-shaped region of buckled plies and extensive rubble.

Figures 2-66 and 2-67 show SEM photographs of fracture features observed in the first and second layers of the delamination in zone A close to the outer surface. In each layer, the delaminations are associated with a central zone of compression debris (Figure 2-66a), believed to be the local point of impact. The delamination was characterized by fine river patterns in the fractured epoxy (Figure 2-66b) that propagated radially outward from the impact site, and suggested that delamination had occurred due to peel.

Figure 2-67 shows SEM photographs of the delamination in zone A with the second layer removed. Again peel fracture characteristics were observed. Stray regions were also associated with "bare" boron fibers (Figure 2-67a), however, it was felt that these were unrelated to the failure event.

SEM examination of the damage in zone B again revealed features indicative of failure due to impact. Figure 2-68 is a macrophotograph of the section with the outer skin removed. The fracture surface was characterized by two local points of impact (only one of which is shown), cracks in cross-ply and extensive rubble.

Figure 2-69 shows SEM photographs of the delaminated layer in zone B. Again mapping of the rivers indicated local fracture propagating by peel radially across the surface with key-holing (Figure 2-69a) and an abundance of compression debris.

2.8.3.4 Microstructure/Material Tests

No microstructural or chemical tests were performed because it was concluded that the failures were unrelated to microstructural defects. In addition, no engineering drawings with material call-outs were available.

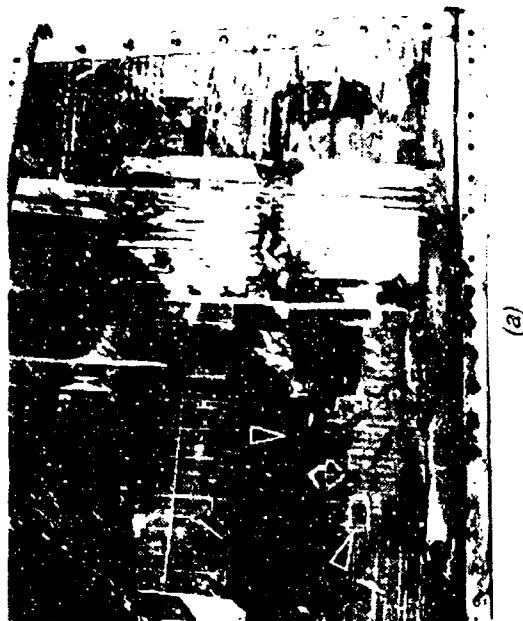
2.8.4 Summary

NDE tests, visual and SEM fractographic tests established that the failure of the stabilizer was caused by foreign object or impact damage. No stress calculations were performed since load histories were unavailable.

2.9 FAILURE ANALYSIS OF A CYLINDRICAL SPECIMEN

2.9.1 Abstract

Failure analysis was performed by Northrop Corporation on a cylindrical specimen supplied by the Air Force. It was determined that failure occurred due to torsional overload.



(a)



(b)



(c)

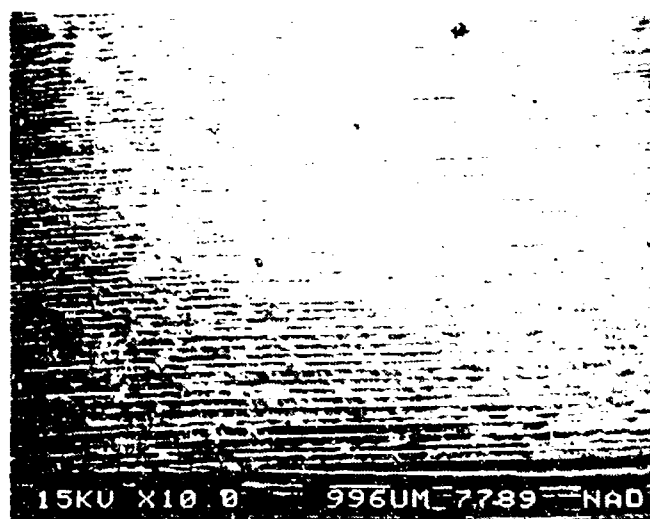
Figure 2-65. Evaluation of Skin Damage in Zone A After Ply Removal

(a) Top Layer Removed

Note buckled plies and wrinkling at arrows

(b) Second Layer Removed

(c) Third Layer Removed

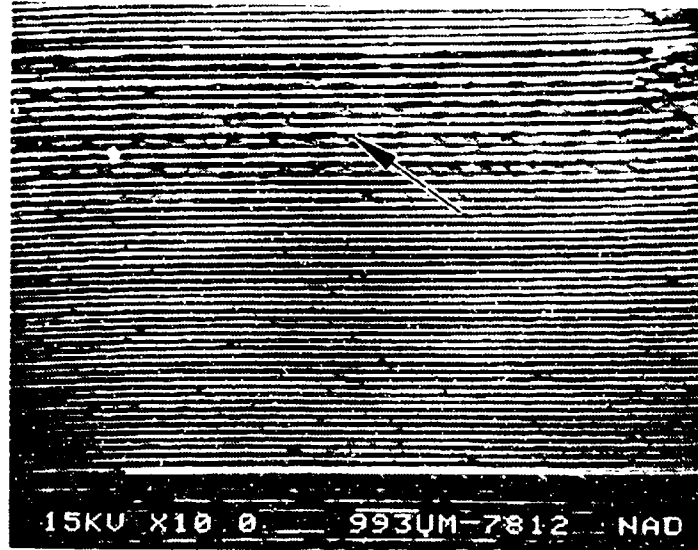


(a)

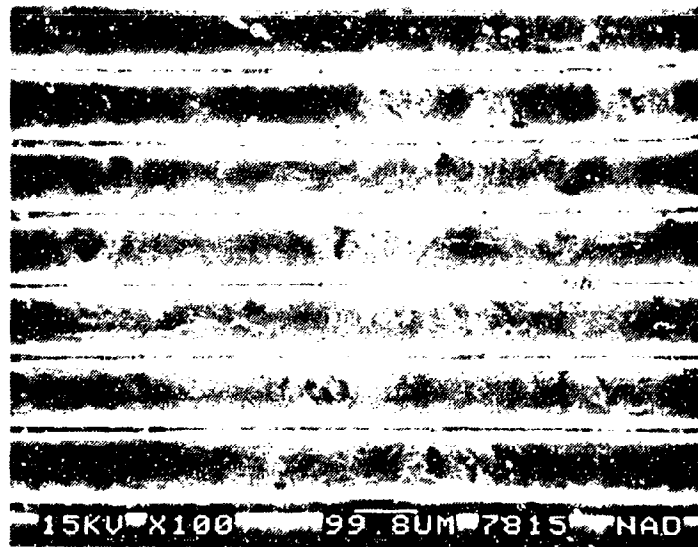


(b)

Figure 2-66. SEM Photographs of Delamination in Zone A (Top Layer Removed)
 (a) Low Magnification Showing Component Debris
 (b) High Magnification Showing Peel Characteristics in Delamination
 Note debris at arrow



(a)



(b)

Figure 2-67. SEM Photographs of Delamination in Zone A (Second Layer Removed)
 (a) Central Region of Resin Starved Fibers (Arrow)
 (b) High Magnification Photograph Showing Detail in Central Region



Figure 2-68. Macrophotograph of Zone B Damage With Top Layer Removed
Note impact at I and cracks at C

2.9.2 Background

A simple component in the form of a hollow cylindrical specimen was submitted to Northrop for evaluation. Background information provided by the Air Force indicated that the specimen was fabricated from Kevlar/bismaleimide and subsequently tested to failure. No background information on the tests performed was provided.

2.9.3 Analysis of Failure

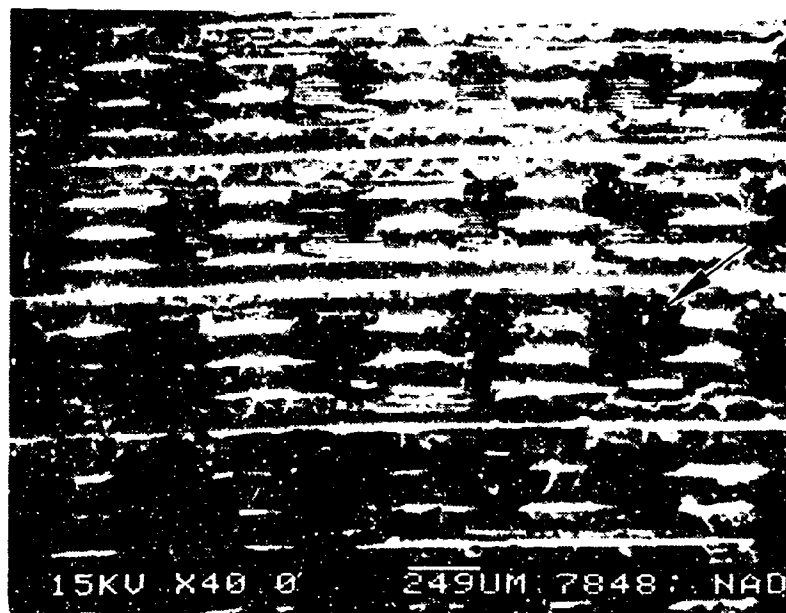
The failure analysis sequence consisted of initial visual examination and macroscopic documentation of the part. NDE of the part failed to reveal any interior defects. The regions of visible fracture were removed using ply-removal methods, and examined using scanning electron microscopic (SEM) techniques. SEM examination established failure due to torsional overload leading to an in-plane shear stress condition in the failed plies.

2.9.3.1 Visual Examination

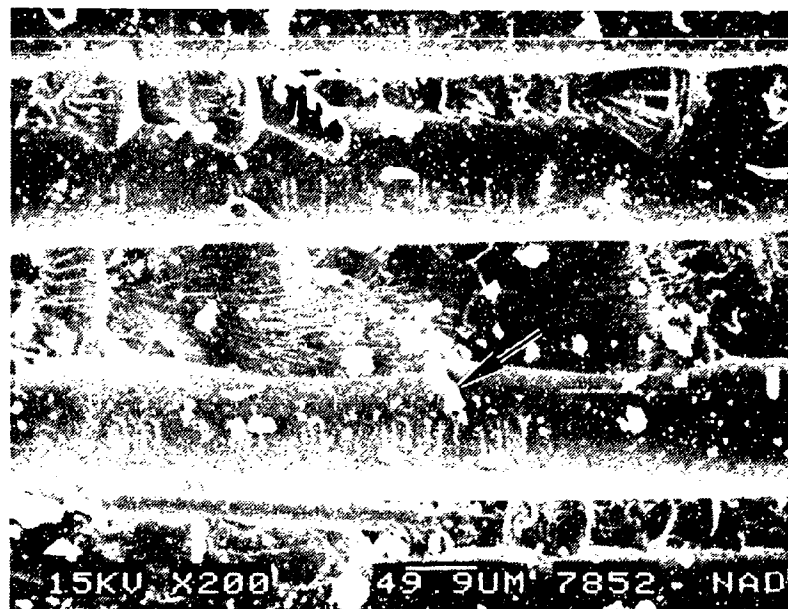
Figure 2-70a shows the component in the as-received condition. Visual examination of the component revealed that the part was filament wound and that it exhibited a surface condition in the form of a diagonal bulge (shown in Figures 2-70b and 2-70c) present around the outer periphery of the gage section of the cylinder.

2.9.3.2 NDE Tests

Conventional ultrasonic testing of the component was unsuccessful because of the non-availability of a transducer with a cylindrical contour. X-ray radiography was carried out and revealed indications in the area of the bulge previously detected by visual examination. No other areas of damage were detected in the hollow cylinder.



(a)

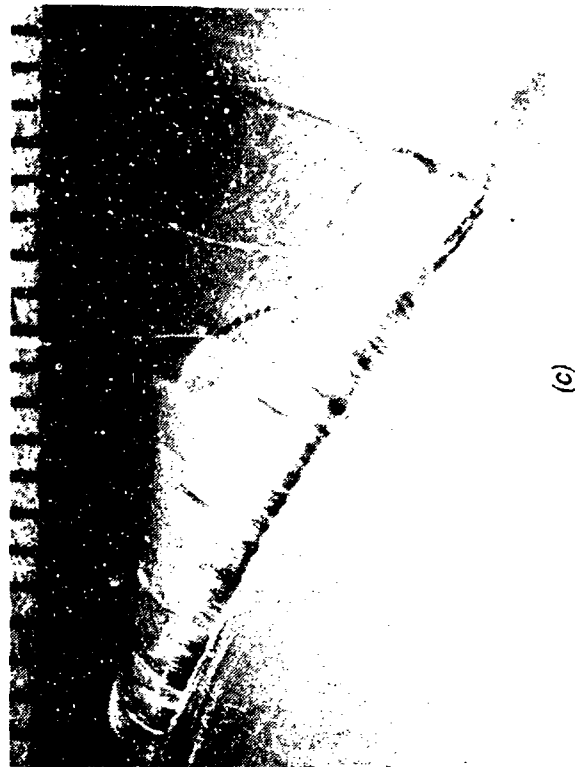


(b)

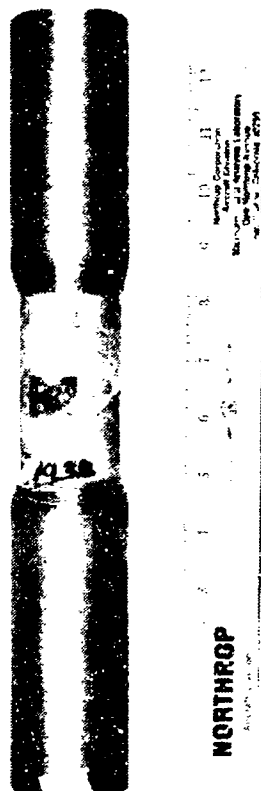
Figure 2-69. SEM Photographs of Zone B Delamination (Top Layer Removed)
 (a) Low Magnification Showing Key-Holing (Arrow)
 (b) High Magnification Showing Compression Debris (Arrow)



(b)



(c)



(a)

Figure 2-70. As-Received Documentation of Failed Cylindrical Specimen
 (a) Overall Specimen
 (b), (c) Surface Bulge on Periphery of Cylinder

2.9.3.3 Fractographic Examination

Figure 2-71 presents a photograph of the cylinder after sectioning with a diamond wheel. Sectioning was guided by the NDE and visual observations, and precautions were taken to ensure that sectioning was well away from the damage. The fragments have been arbitrarily labeled as A, B, and C, in Figure 2-71, with fragment B containing the region of damage.

Figure 2-72 presents photographs of fragment B as viewed from various angles. Examination of the inner surface of the fragment revealed internal displacements (Figure 2-72a) which correspond to the external bulge. The contour of the interior defect was identical to that present on the exterior, indicating that these areas of damage had possibly been caused by the same load event.

SEM examination was carried out on the outer and inner surfaces of the cylinder. Figures 2-73, 2-74, and 2-75 present SEM photographs of fracture present on the outer and inner surfaces. As shown in Figure 2-73a, the region of damage on the outer surface consisted of localized displacement of fiber bundles, splitting of fibers, and defibrillation of fiber ends. Figure 2-74 presents SEM photographs of the outer surface with the cluster of fibrils removed. As can be seen in Figure 2-74a, the fractured resin exhibited hackles, and the fibers appeared to be bending under shear loads (Figure 2-74b). Such fracture characteristics are typical of failure due to localized in-plane shear stresses caused by torsional loads. Figure 2-75 presents SEM photographs of the inner surface of the cylinder. The failure in this region was also characterized by fiber splits, and bending of fiber ends.

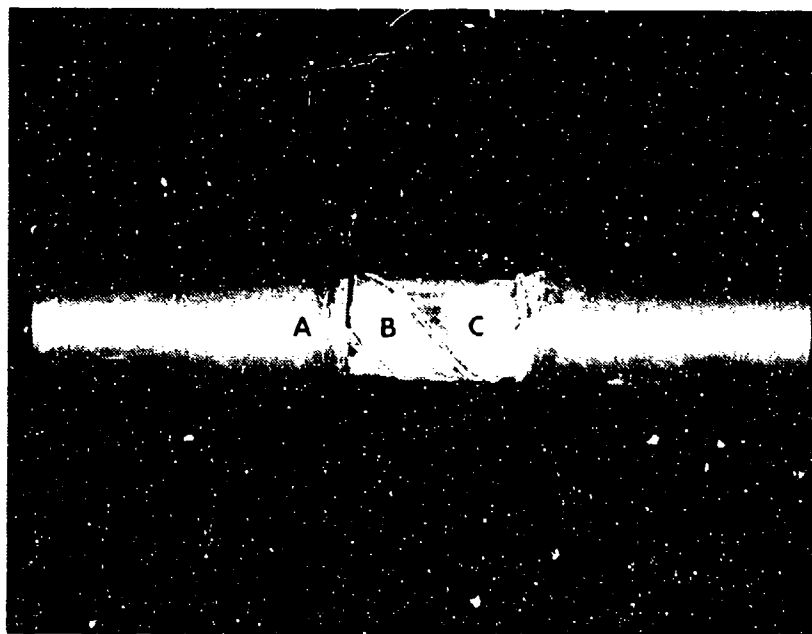


Figure 2-71. Photograph of Cylindrical Specimen After Sectioning to Expose Internal Damage

Note: The fragments have been labeled as A, B, and C.



(a)

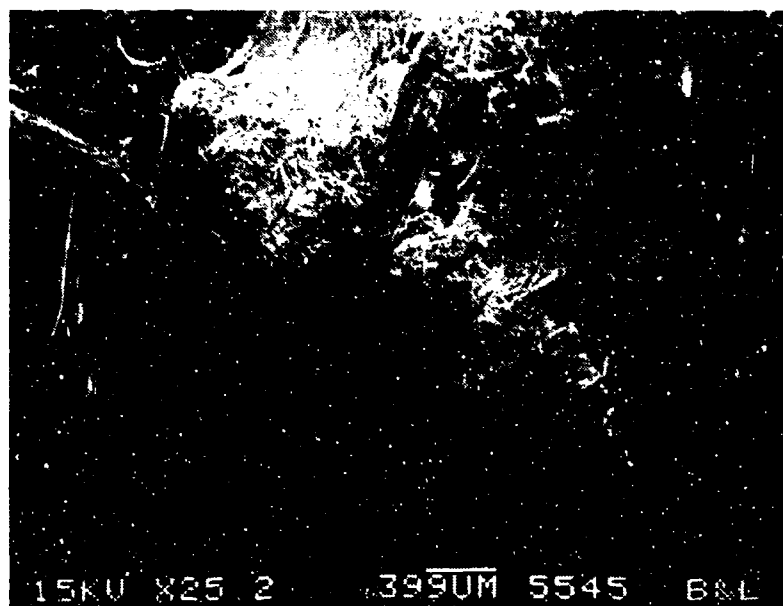


(b)

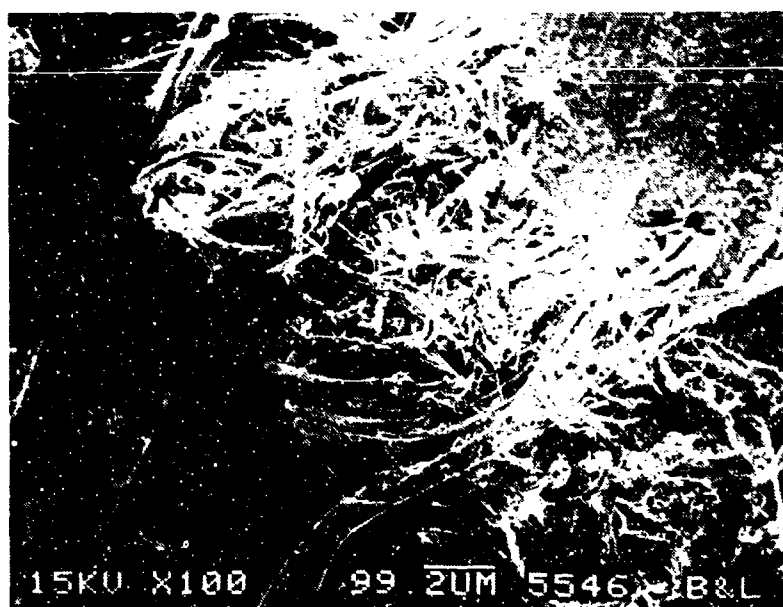


(c)

Figure 2-72 Photographs Showing Damage in Fragment B of Cylinder
 (a) 1X Photo Shows Interior Damage
 (b) 2X Photo of Interior Damage (Bulge at Arrow)
 (c) 2X Photo Showing Mating Damage on Exterior

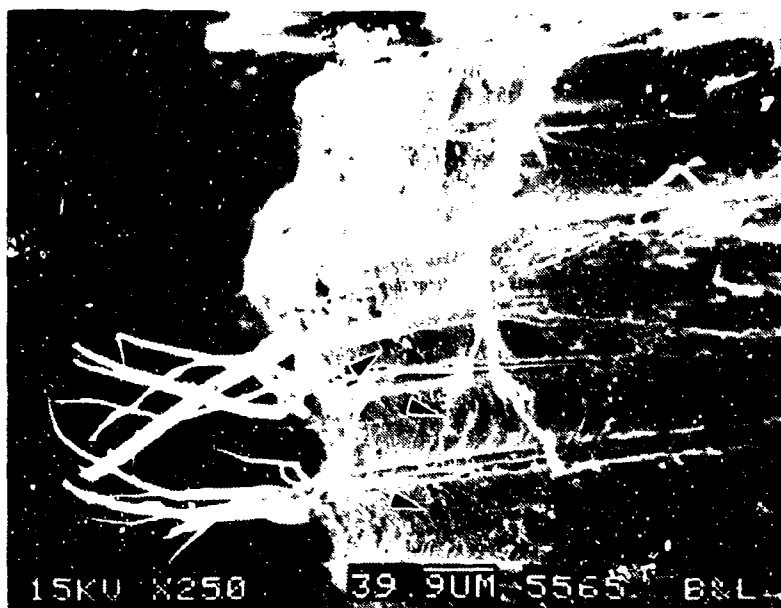


(a)

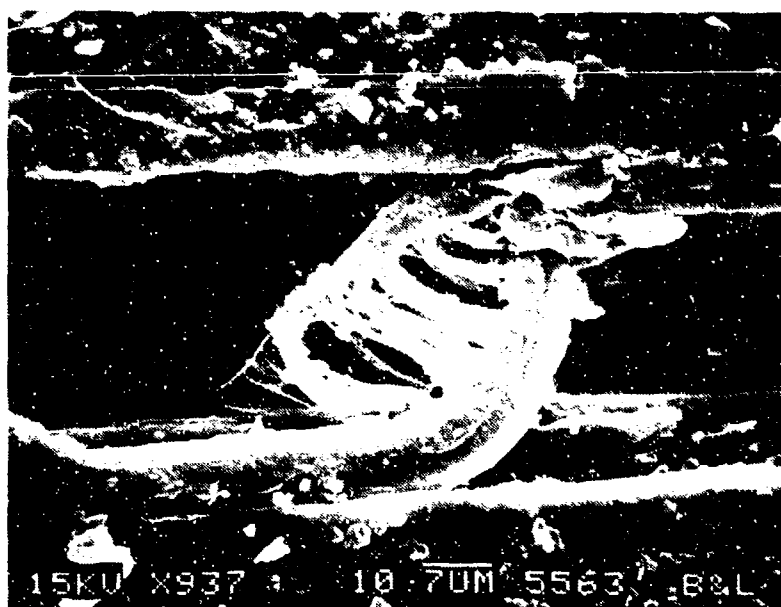


(b)

Figure 2-73. SEM Photographs of Damage on Outer Surface of Cylinder
 (a) Low Magnification Showing Displacement of Fiber Bundles, Splits and Defibrillation of Fiber Ends
 (b) High Magnification Photograph Showing Fibril Clusters

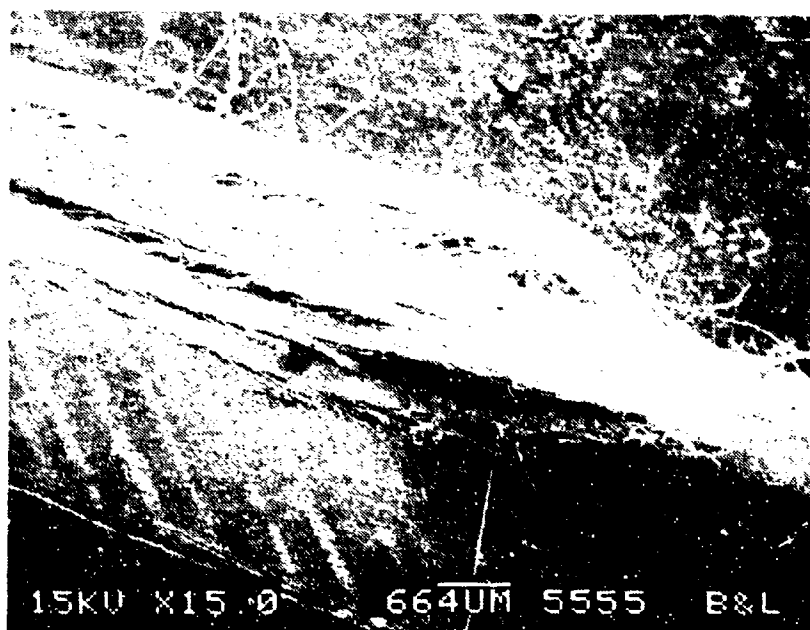


(a)

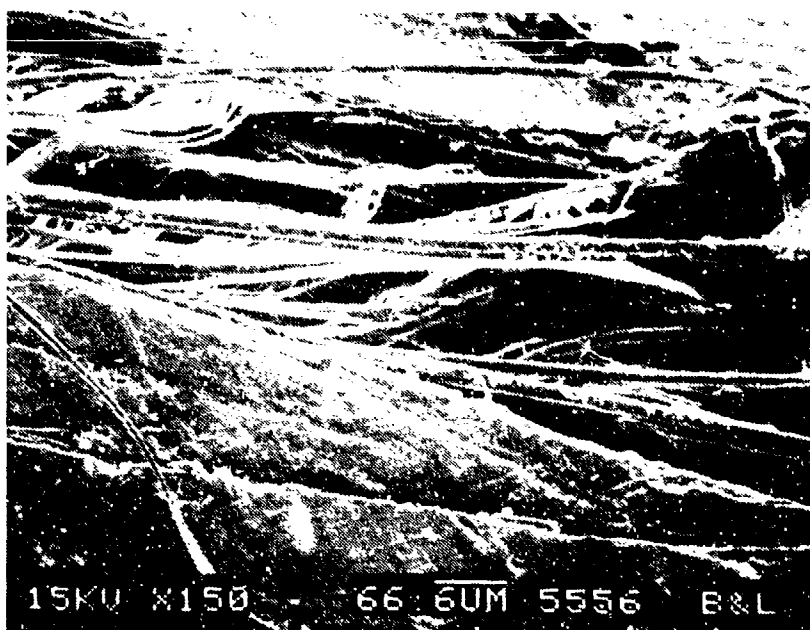


(b)

Figure 2-74. SEM Photographs of Outer Surface Damage With Clusters of Fibrils Removed
 (a) Hackles (Arrows) in Resin
 (b) Localized Bending of Fibers



(a)



(b)

Figure 2-75. SEM Photographs of Damage on Inner Surface of Cylinder
 (a) Low Magnification Showing Splitting
 (b) High Magnification Showing Splits and Bending of Fibers

2.9.3.4 Material Tests

Radial sections were taken through the cylinder in the region of the defect, and the sections were oriented so that the fractures were in profile. Figure 2-76 shows optical micrographs of the cross-sections taken through the failed regions. In these areas, no material defects such as porosity or contaminants were detected. Chemical identification of the resin was not carried out due to lack of material specifications. However, the general appearance of the fracture locations and morphologies suggested that failure was not related to material discrepancies.

2.9.3.5 Stress Analysis

Elementary stress analysis indicated that torsional loading of the cylinder would lead to localized in-plane shear conditions in elements of the cylinder. This would lead to delaminations caused by in-plane shear stresses. Bending of the fiber bundles would occur due to the critically resolved tensile components associated with the torsional loads.

2.9.4 Summary

Failure of the hollow cylinder occurred under torsional overload. The localized failures were caused by in-plane shear stresses associated with the torsional loads.

2.10 FAILURE ANALYSIS OF A COMPOUND PLATE AND FASTENER ASSEMBLY

2.10.1 Abstract

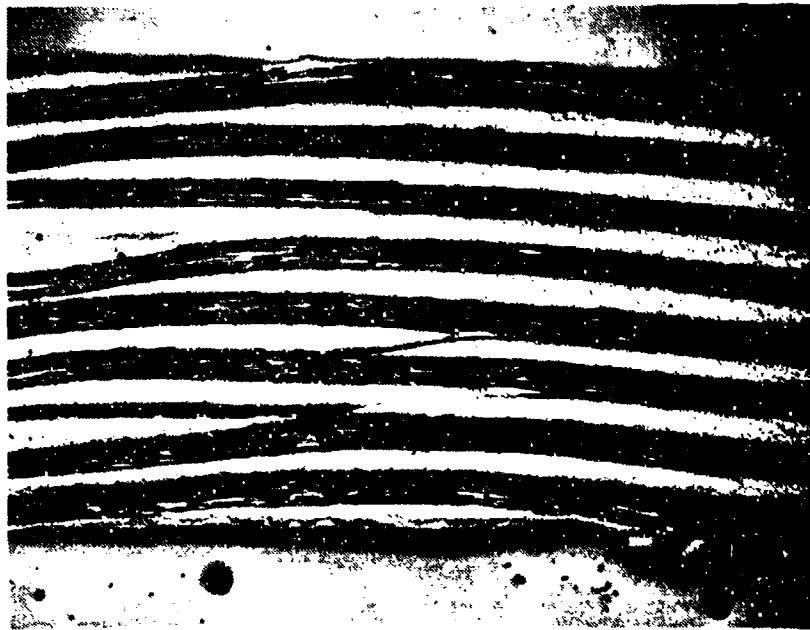
Failure analysis was performed by Northrop Corporation on a bolted joint structure in the form of a compound honeycomb plate and fastener assembly. It was concluded that failure occurred due to overheating. Adhesive failure occurred in the honeycomb section leading to core separation. The effect of core separation and/or thermal stresses induced by overheating led to tension and bending loads at the bolted joint, and resulted in delamination of the plate.

2.10.2 Background

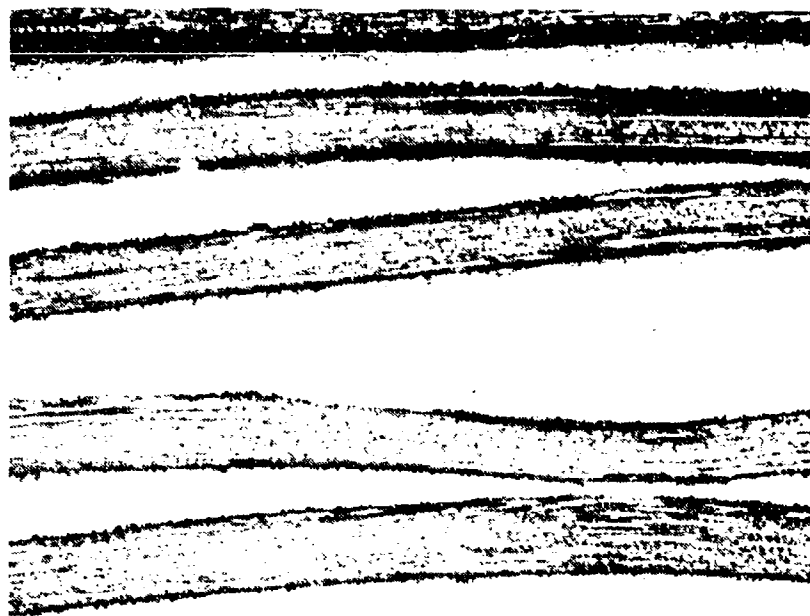
A compound honeycomb plate and fastener assembly was submitted to Northrop by the Air Force for evaluation. Background information supplied by the Air Force indicated that the component was from a larger part originally manufactured from a glass/bismaleimide laminate bonded to a honeycomb core structure. No other background information was available.

2.10.3 Analysis of Failure

The failure analysis sequence consisted of initial visual examination and macroscopic documentation of the part. Based on initial tests, NDE examination and detailed fractographic examination were carried out. Scanning electron microscope (SEM) examination of the failed surfaces played a key role in establishing the failure mode.



(a)



(b)

Figure 2-76. Optical Photomicrographs of Cross-Section Taken Through Defects in Cylinder
(a) Magnification = 20X
(b) Magnification = 50X

2.10.3.1 Visual Examination

Examination of the component in the as-received condition revealed a charred or burnt odor suggesting that the part may have been heat damaged. Figure 2-77 shows photographs of the part as-received. A lateral view of the assembly is shown in Figure 2-77a and the upper surface of the plate is shown in Figure 2-77b.

During initial examination, the lower face plate separated from the honeycomb core. The mating halves of the fragments are shown in Figures 2-77c and 2-77d. The remnants of the honeycomb can also be seen in these photographs. It was observed that the honeycomb had a dull brown color suggesting a glass honeycomb. The regions labeled A, B, C and D in Figure 2-77c are areas where detailed SEM examination was performed on the delaminated section.

2.10.3.2 NDE Tests

Several zones of delaminated fracture were apparent by visual evaluation. X-ray testing of the assembly failed to reveal any additional regions of delamination.

2.10.3.3 Fractographic Examination

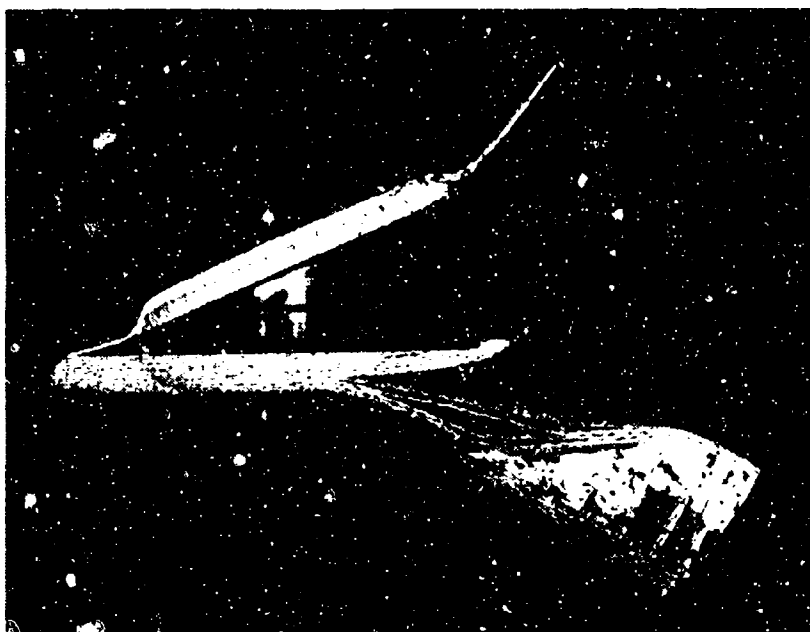
Fractographic evaluation was carried out on delaminated regions of the top and bottom surfaces of the plate. Figures 2-78, 2-79, and 2-80 present SEM photographs of fracture characteristics observed in the honeycomb section at the bottom surface. In the vicinity of the hole (Region A), the surface delamination was associated with mixed cohesive and adhesive failure (Figure 2-78a). The fractured adherend in the adhesively failed regions exhibited peel fracture characteristics (Figure 2-78a). A mapping of the river patterns in the vicinity of the bolt-hole indicated that fracture had initiated at the hole and was radiating outward and away toward the honeycomb (see Figure 2-77d). Holes and voids were observed in the resin (see Figure 2-78b), which along with the appearance and smell of the component suggested that overheating had occurred.

Figure 2-79 presents SEM photographs away from the hole (Region B). On a macroscopic scale, the fracture had a glazed appearance. SEM examination revealed a melted and resolidified surface, associated with porosity and mud-flat type cracking (Figure 2-79b). It is believed that the cracking occurred during the cooling phase after overheating of the assembly.

Figure 2-80 presents photographs of the fracture observed in Region C; namely the honeycomb area. The fracture was characterized predominantly by adhesive failure (Figure 2-80a) and heat damage to the adherend (Figure 2-80b).

SEM examination was also carried out on a cross-section of the plate bolt-hole (Region D). The fracture features observed are shown in Figure 2-81. The cross-section revealed fracture characteristics indicative of bearing loads, namely compression of the fibers (Figure 2-81a) and debris. Also of interest was the extensive porosity present in the epoxy (Figure 2-81b).

The top surface of the compound plate was also examined. The section was extremely brittle and delaminated upon gentle handling with a tweezer (Figure 2-82). Evaluation of the fragment, which appeared to be ceramic in nature, revealed evidence of overheating as suggested by the bent contour (Figure 2-83a) and voids observed during SEM examination (Figure 2-83b).

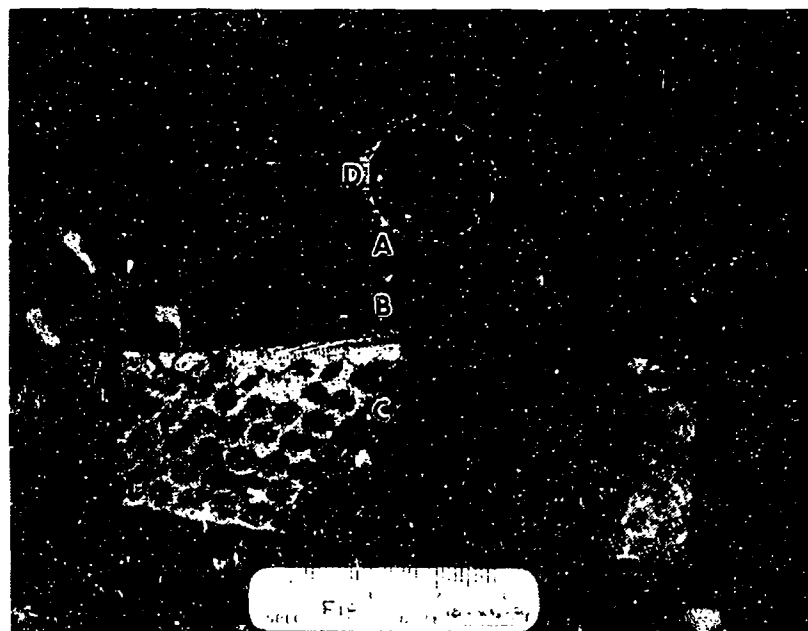


(a)

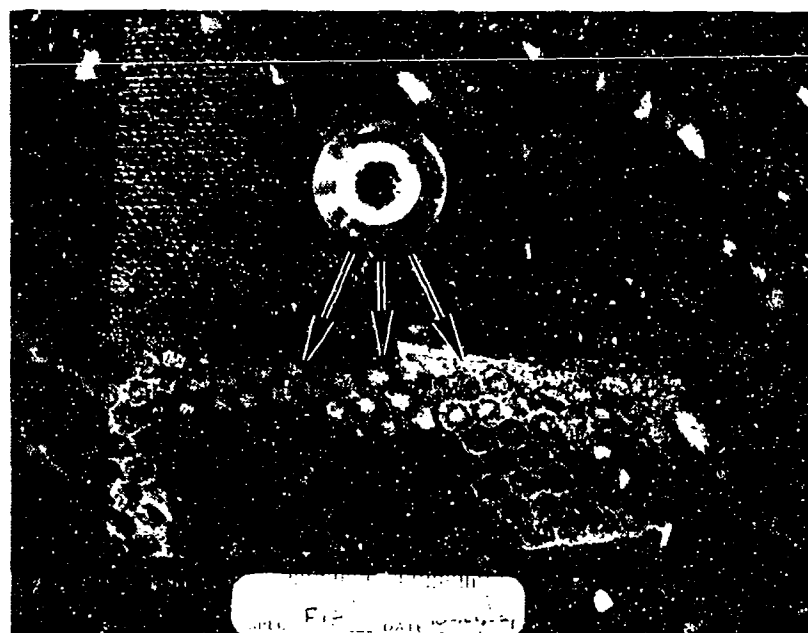


(b)

Figure 2-77. As-Received Documentation of Compound Plate and Fastener Assembly
 (a) Lateral View of Assembly
 (b) Top Surface of Plate



(c)



(d)

Figure 2-77. (Continued)

(c), (d) Delamination in Bottom Surface of Compound Plate (Mating Halves)

The regions labeled A, B, C, and D are where detailed SEI⁺ examination was carried out. The arrows indicate fracture mapping.

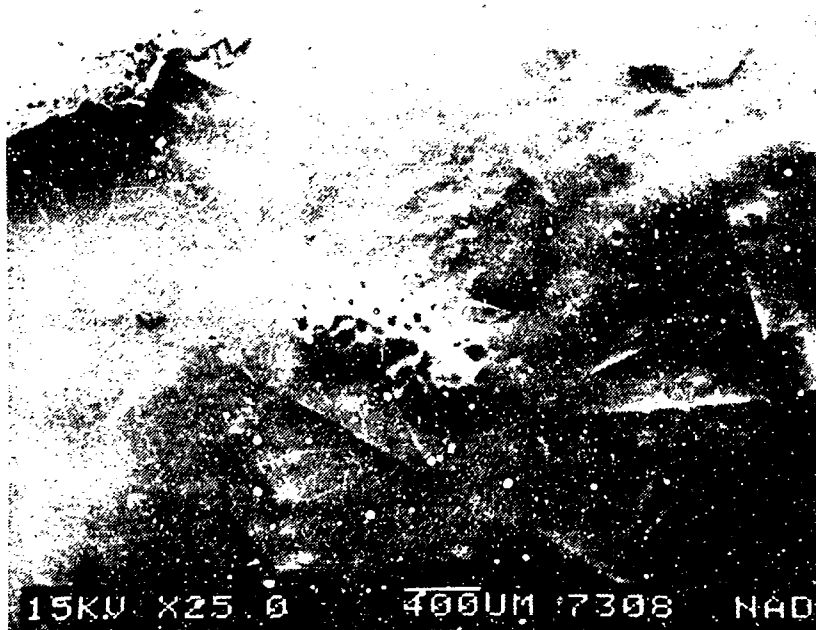


(a)

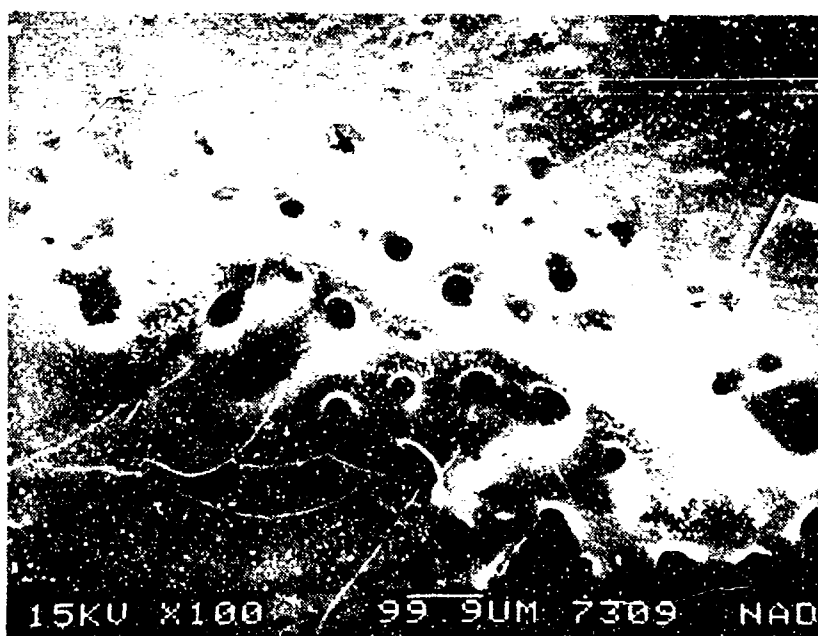


(b)

Figure 2-78. SEM Photographs in Region A of Delamination of Bottom Surface of Compound Plate
 (a) Mixed Cohesive-Adhesive Failure
 (b) Holes and Voids in Resin
 Note river patterns (arrow)



(a)

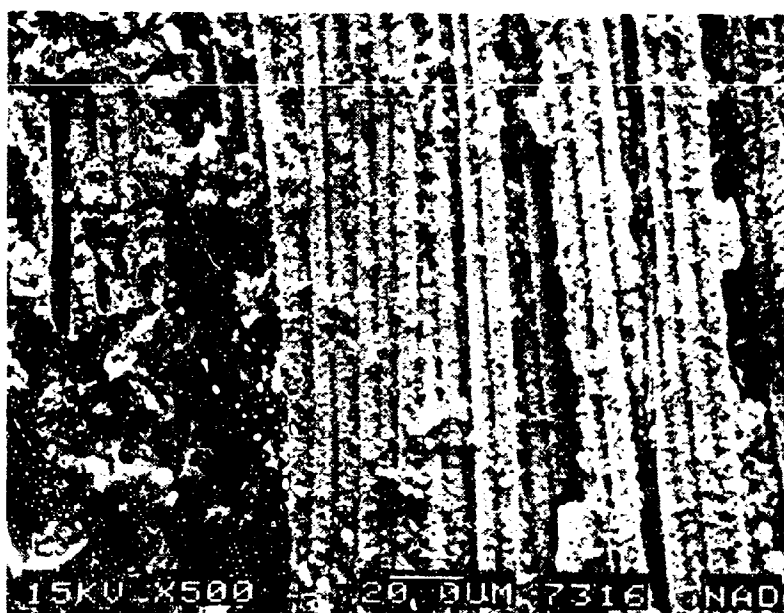


(b)

*Figure 2-79. SEM Photographs in Region B of Delamination of Bottom Surface of Compound Plate
(a), (b) Low and High Magnifications Showing Melted Surface Associated With Porosity and Cracks*

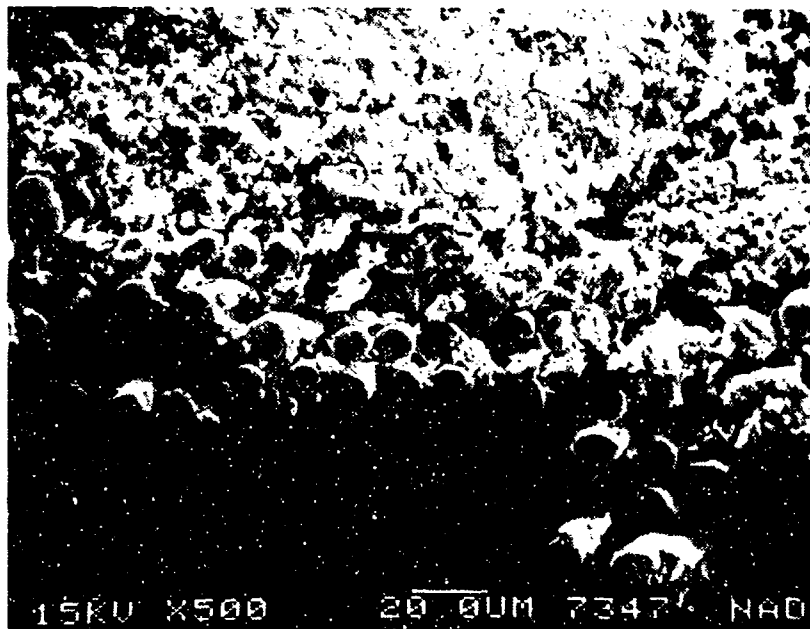


(a)

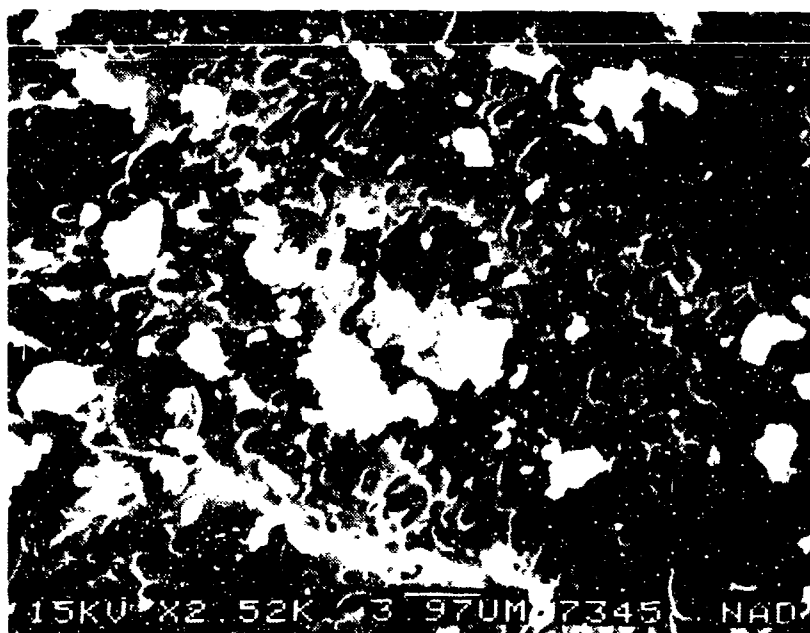


(b)

Figure 2-80. SEM Photographs in Region C (Honeycomb Region) of Delamination of Bottom Surface of Compound Plate
 (a) Adhesive Failure of Honeycomb
 (b) Heat Damage to Adherend



(a)



(b)

Figure 2-81. SEM Photographs of Bolt Hole Cross-Section in Bottom Surface of Compound Plate (Region D)
 (a) Compression Fracture of Fiber Ends
 (b) Porosity and Debris in Resin

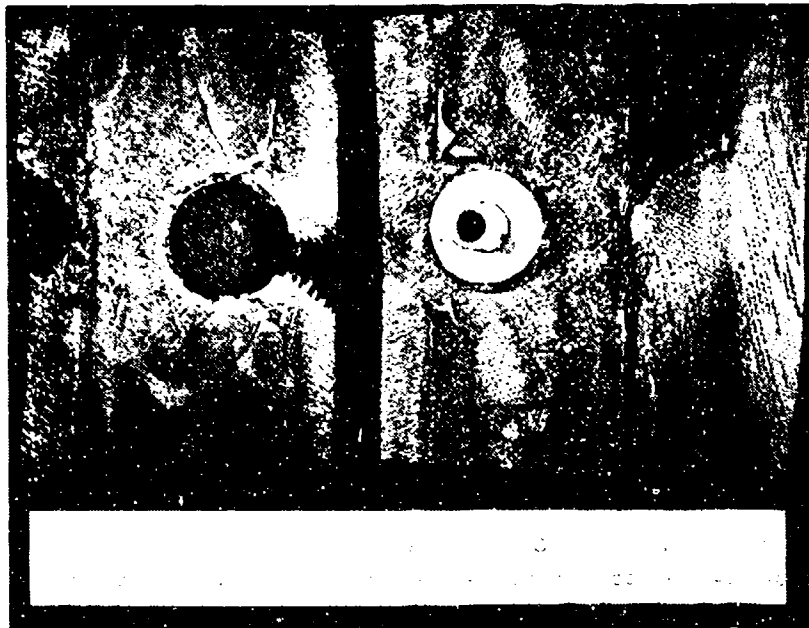


Figure 2-82. Delamination in Top Surface of Compound Plate (Mating Halves)

2.10.3.4 Stress Analysis

Elementary stress analysis indicated that the delaminations in the compound plate were caused by adhesive failure of the honeycomb leading to bending loads being introduced. It was also believed that the thermal stresses caused by heating/cooling of the joint resulted in additional tension and bending loads at the bolt hole.

2.10.4 Summary

Failure occurred due to overheating of the assembly. This led to melting and pyrolysis of the resin and the concomitant melting of the adhesive in the bonded region. Adhesive failure occurred and the effect of the core separation combined with thermally induced stresses caused by heating/cooling led to tension-cleavage failure at the bolted joint (see editorial note in Section 2.12.3).

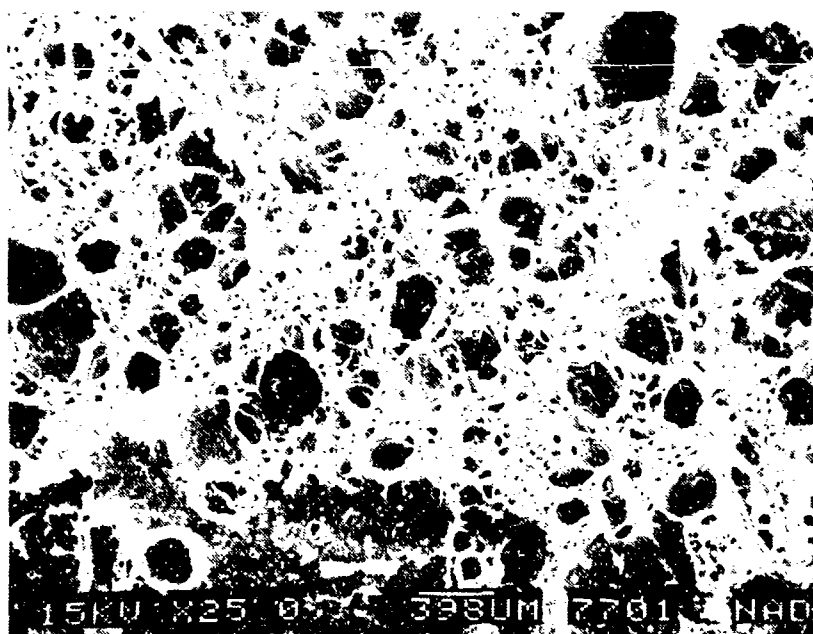
2.11 FAILURE ANALYSIS OF A COMPOSITE ARCH REINFORCEMENT

2.11.1 Abstract

Failure analysis was performed by Northrop Corporation on a failed composite arch reinforcement for a canopy windshield. The failure analysis logic network (FALN) was used to determine the failure location, and to establish the cause for failure of the part. It was determined that under application of bending and torsional loads, cracks initiated at several fastener holes



(a)



(b)

Figure 2-83. Optical and SEM Photographs of Delaminated Fragment of Top Surface of Compound Plate
 (a) Oblique View Showing Bent Contour of Fragment
 (b) Voids on Top Surface

where fasteners may have been loose. Under applied loads, cracking occurred across the sheath, with multiple internal delaminations in the bow. It was determined that the part was of poor quality, and this may have accelerated the failure process.

2.11.2 Background

One composite arch reinforcement for the forward windshield of a T-38 canopy was submitted to Northrop by the Air Force for evaluation. No service records or flight history of the component were available. To assist in the investigation, the Air Force provided sketches showing the location of the component in the canopy. It was also reported that the arch had been fabricated using a combination of glass and Kevlar/epoxy, and that the part was bonded to a cast magnesium frame in the canopy.

2.11.3 Analysis of Failure

The FAILN sequence consisted of initial visual examination and macroscopic documentation of the part, followed by NDE evaluation. The fracture regions associated with the failure were macroscopically examined. Internal fractures were revealed by ply sectioning to expose fracture surfaces. Scanning electron microscope (SEM) examination was carried out on several fracture samples. Optical cross-sections were taken through several regions of the part. Elementary stress analysis was performed on the part. Based on all the results obtained, the cause for failure was established.

2.11.3.1 Visual Examination

Figure 2-84 shows a collage of the part in the as-received condition. Close examination of the part indicated that the component consisted of a thin woven sheath (believed to be Kevlar/epoxy) enclosing a laminated bow (believed to be filament wound Kevlar/epoxy and glass/epoxy). The part was associated with extensive cracking all around the outer periphery (see Figure 2-84b); and along the inner diameter in mid-section regions containing fastener holes (see Figure 2-84c, and Figure 2-85a). When viewed obliquely, the sheath appeared torn in several areas (see Figure 2-85b). The entire sheath appeared loose and disbonded, and barely held in place by the ends. In addition the bow was associated with extensive delaminations (see Figure 2-85c), as determined by simple visual examination of the part.

2.11.3.2 NDE Testing of Component

The part was examined using conventional X-ray radiography, with emphasis around the fastener holes where cracks had been observed. No significant indications were determined other than those visually detected. Ultrasonic testing could not be performed due to unavailability of a cylindrical transducer.

2.11.3.3 Fractographic Examination

Guided by the visual and NDE tests, the part was sectioned into four sections for detailed fractographic examination. Figure 2-86a shows the part after sectioning. The sections have been

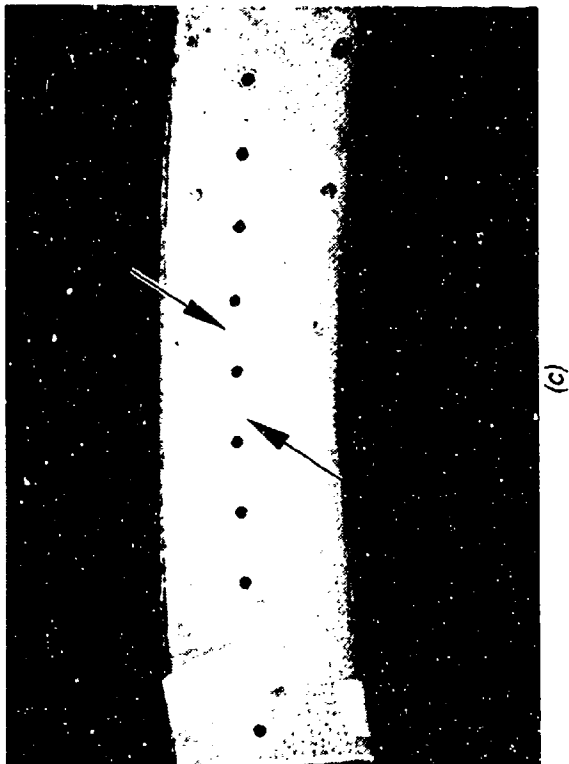
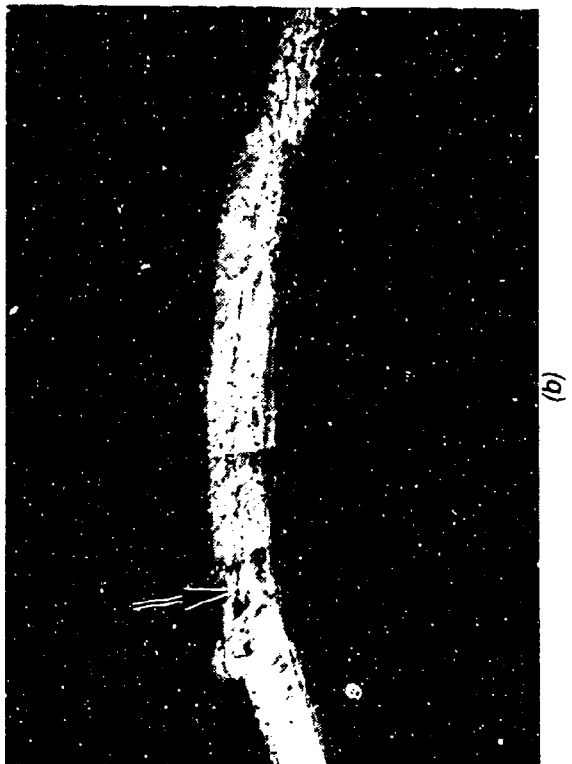
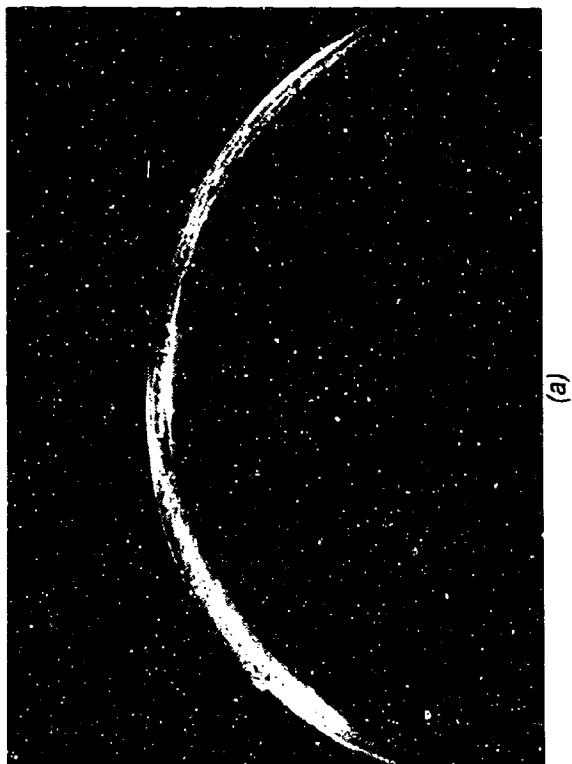
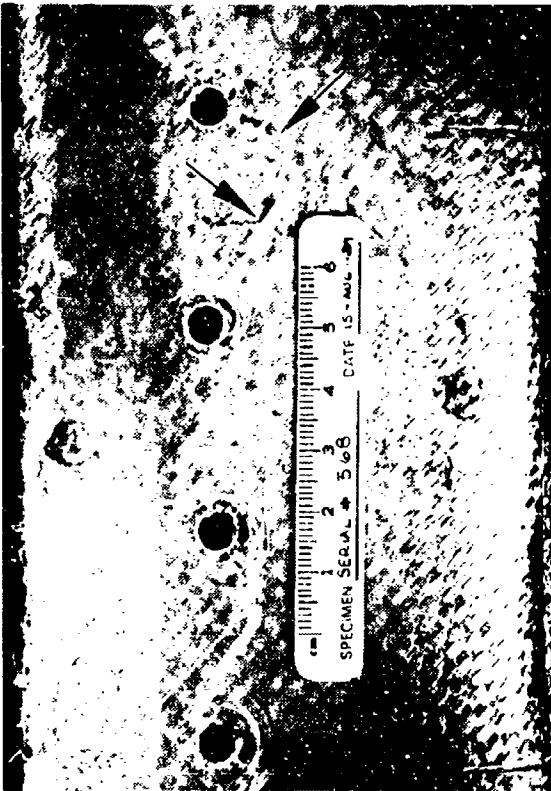


Figure 2-84. As-Received Documentation of Composite Arch Reinforcement
 (a) Overall View
 (b) Cracking in Outer Periphery of Sheath (Arrow)
 (c) Cracks in Mid-Section Fastener Holes (Arrows)



(a)

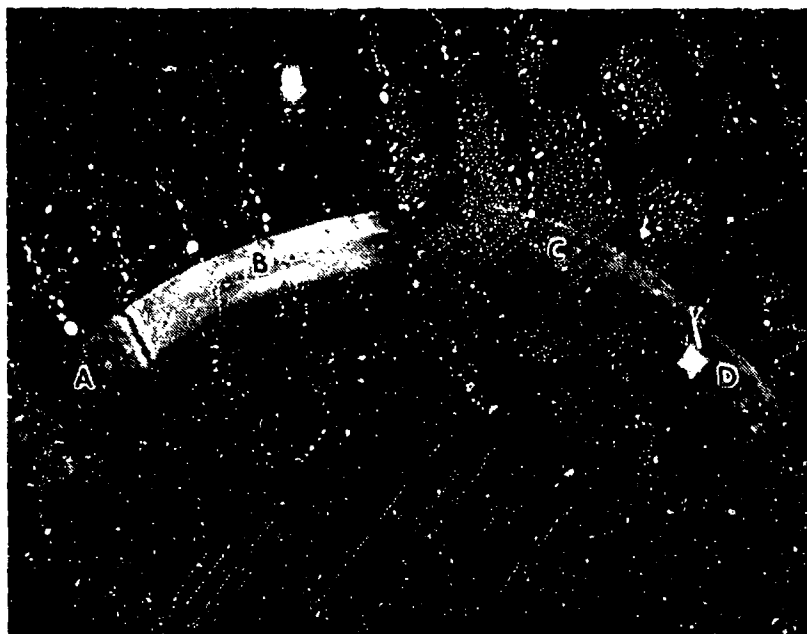


(b)

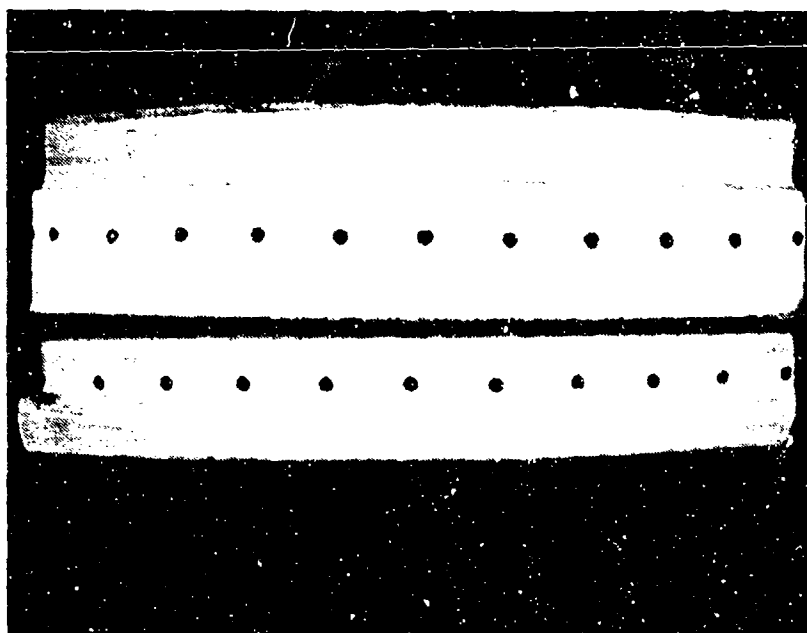


(c)

Figure 2-85. Documentation of Cracks in Part
 (a) Shear Cracks in Fastener Holes (Arrows)
 (b) Oblique View Showing Tearing of Sheath
 (c) Delaminations in Bow Contained by Sheath
 (Arrows)



(a)



(b)

Figure 2-86. Documentation of Ply Removal and Sectioning
(a) Sectioning of Part

Note: The fragment labeled B contain fastener cracks.

(b) Delamination of Bow in Fragment Labeled C

arbitrarily labeled as A, B, C, and D in Figure 2-86a. Upon sectioning, the sheath totally separated from the bow in the sections labeled B, and C. In addition the bow delaminated into two fragments in the section labeled C, as is illustrated in Figure 2-86b.

Initial examination was concentrated on the cracks observed in the sheath and bow around fastener holes (refer to Figure 2-85a). The general appearance of these cracks suggested that these were shear cracks, rather than tensile cracks. Figure 2-87 presents fracture features observed in the sheath in the region of a fastener crack. The fracture was characterized by dense tangles of fibrils (Figure 2-87b), as would be expected in translaminar failures in Kevlar/Epoxy. Examination of the regions below the fibrils revealed a delaminated surface associated with hackles, as is shown in Figure 2-87c, indicating that the fastener cracks were shear cracks. The orientation and morphology of the fibrils suggested that cracking in this region occurred under in-plane shear loads, resulting in tensile failures of the Kevlar fibers. Figure 2-88 presents a delaminated region in the bow in the vicinity of a crack. The fracture was once again characterized by shear failure characteristics, namely the occurrence of hackles in the resin (Figure 2-88a). The glass fibers, and Kevlar fibrils (Figure 2-88b) were characterized by tensile fracture characteristics.

Figure 2-89 shows features observed on the bottom surface of the sheath that had separated from the bow. As can be seen in Figures 2-89b and 2-89c, there was practically no evidence of bonding of the sheath to the bow. Figure 2-90 shows optical and SEM photographs of the mating surface where the sheath should have been bonded. Again there was practically no evidence of fracture, with the surface appearing to be in the original unbonded state, and with occurrence of porosity.

SEM examination was also carried out on the delaminations in the bow (refer to Figure 2-86b). Figure 2-91 presents optical and SEM fractographs of fracture features observed in a principal delamination in the bow mid-section. Fracture was characterized by in-plane shear failure characteristics, namely translaminar tensile fracture in the glass and Kevlar fibers (Figure 2-91b), and hackles in the fractured resin (Figure 2-91c).

2.11.3.4 Microstructure/Material Tests

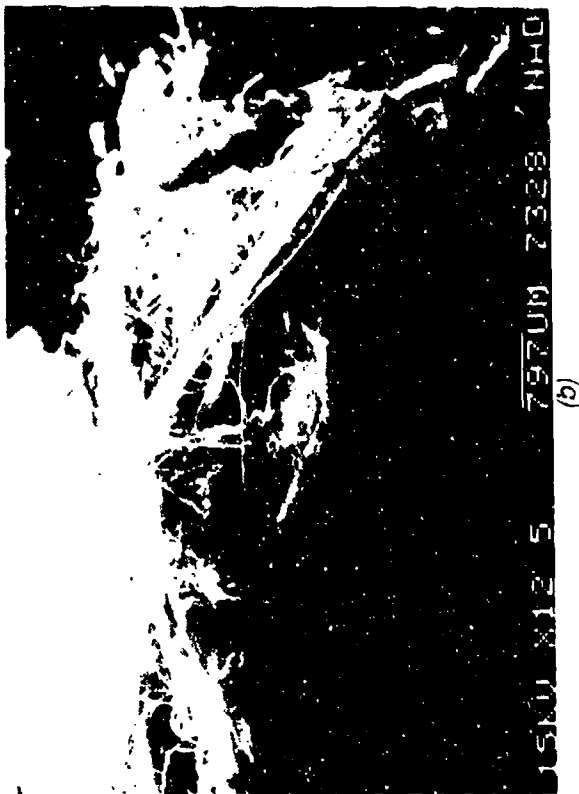
Microstructural examination was carried out on sections taken through the part in a region of fastener holes. As can be seen in Figures 2-92 and 2-93, extensive delaminations were present in the bow, with the sheath totally separated from the bow. The glass and Kevlar plies were characterized by extensive porosity, indicating that the part may have been of poor quality.

2.11.3.5 Stress Analysis

Elementary stress computations indicated that the delaminations in the sheath and bow were caused by the part being subjected to bending and torsional loads. The occurrence of shear cracks in mid-region fastener holes suggests that one or more of the fasteners may have been loose in these regions introducing localized bending and buffeting. Shear cracks formed in these regions, and with the resultant change in loading, the sheath and bow delaminated. The sheath was very poorly bonded to the bow and the bow exhibited severe porosity. It is believed that these material defects resulted in enhanced delamination of the bow.



(a)

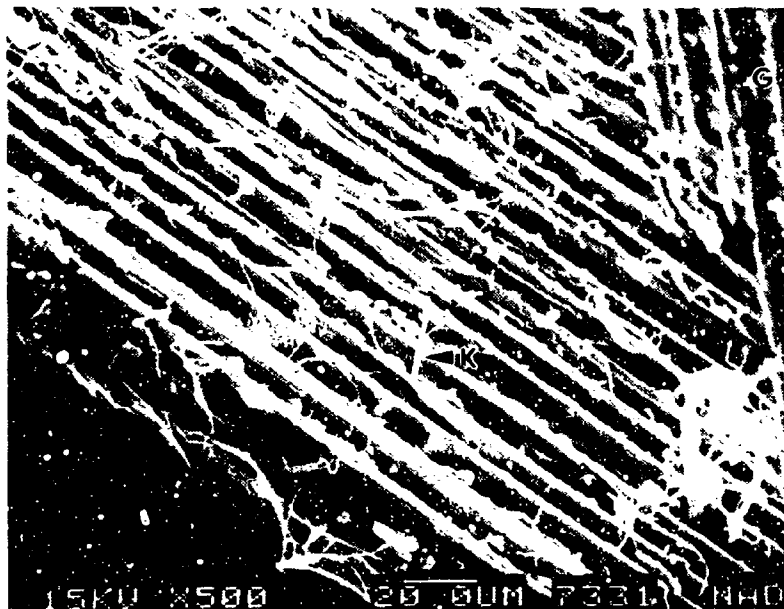


(b)

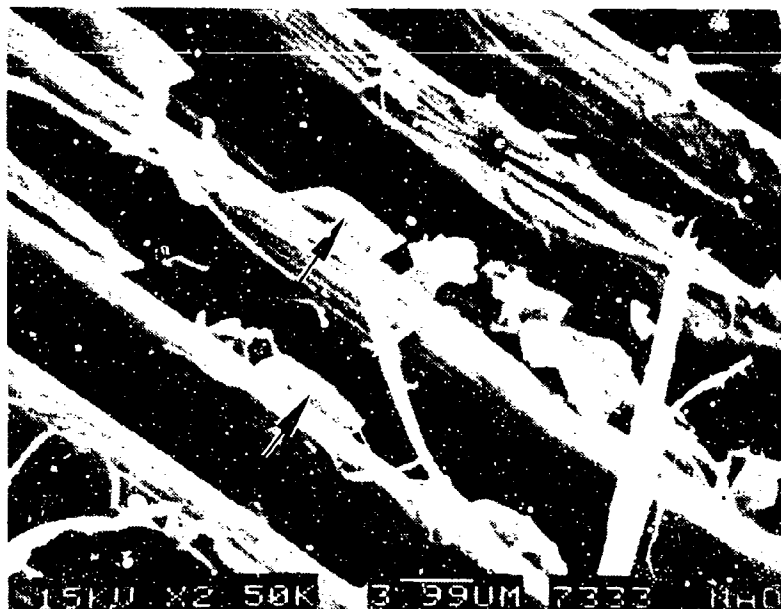


(c)

Figure 2-87. Optical and SEM Photographs of Shear Fracture at Fastener Hole
 (a) Macro photograph of Crack
 (b) SEM Photograph Showing Kevlar Fibrils in Crack Viewed End On
 (c) Delamination Surface Containing Hackles (Arrows)



(a)

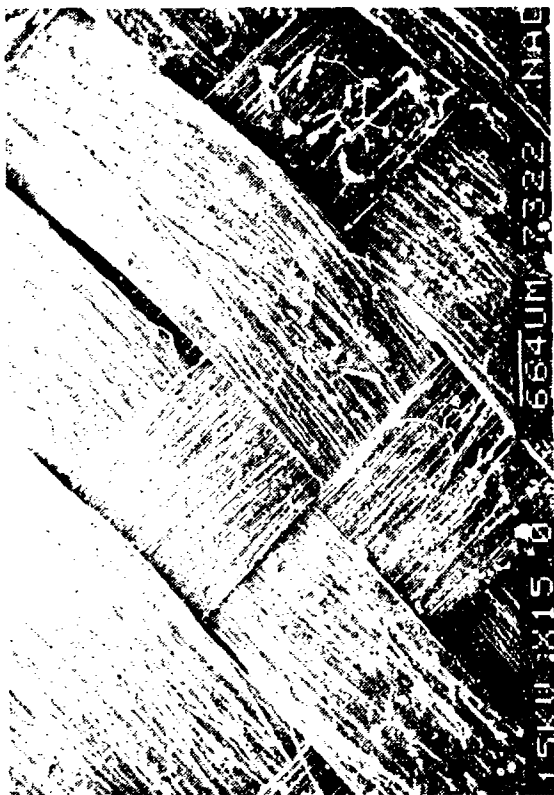


(b)

Figure 2-88. SEM Characterization of Fastener Hole Crack in Bow
 (a) Glass (G) and Kevlar Fibrils (K)
 (b) Hackles in Resin (Arrows)



(a)

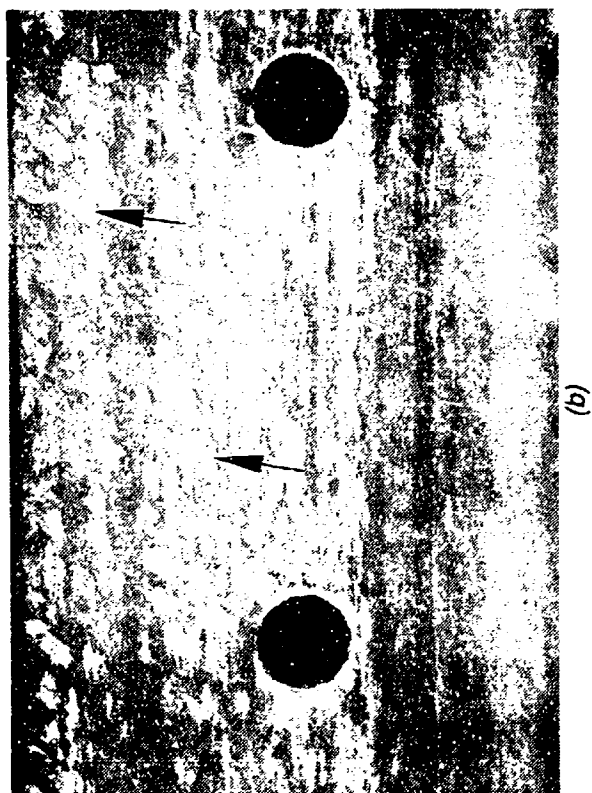


(b)

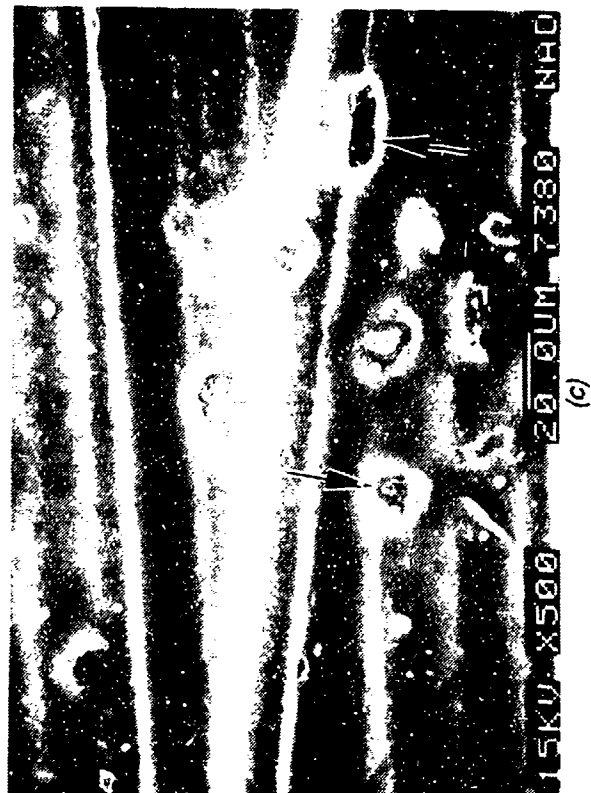


(c)

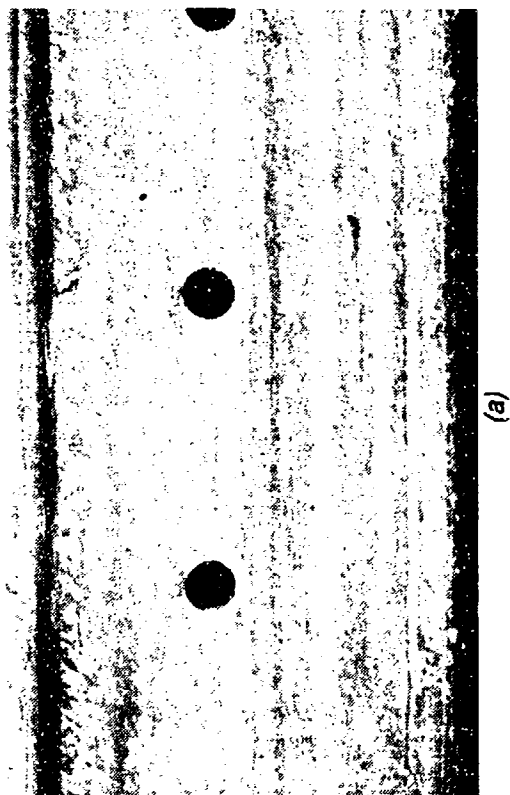
Figure 2-89. Characterization of Sheath Surface
 (a) Macro photograph Showing Separation From Bow
 (b) Macro photograph of Sheath Surface
 (c) Absence of Bonding With Bow



(b)



(c)



(a)

Figure 2-90. Evaluation of Bow Surface
 (a) Macrophoto of Surface Where Sheath Separated
 (b) Higher Magnification Photo Showing Traces of
 Glass Scrim (Arrows)
 (c) SEM Photograph Showing Unbonded Surface
 With Porosity (Arrows)



(a)



(b)



(c)

Figure 2-91. SEM Characterization of Bow Delamination
(a), (b) Tensile Failure of Kevlar and Glass Fibers
(c) Hackles (Arrows) in Resin

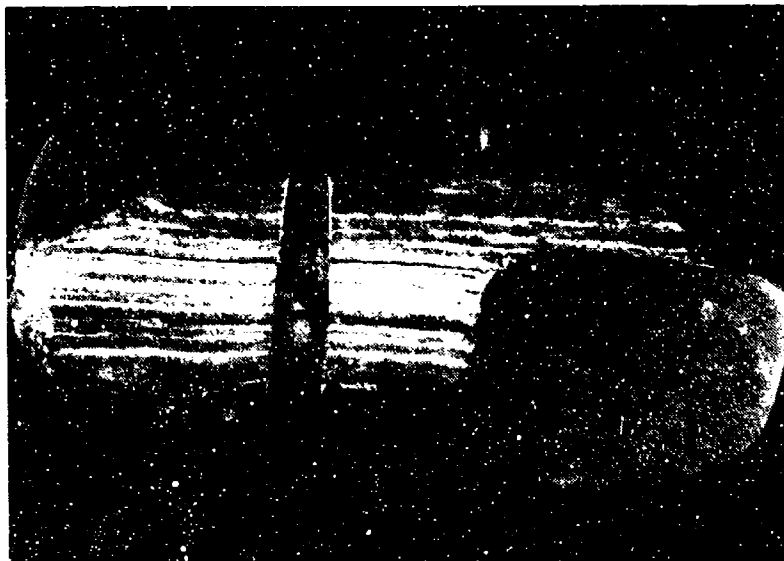


Figure 2-92. Macro photograph of Cross-Section Taken Through Fastener Hole

2.11.4 Summary

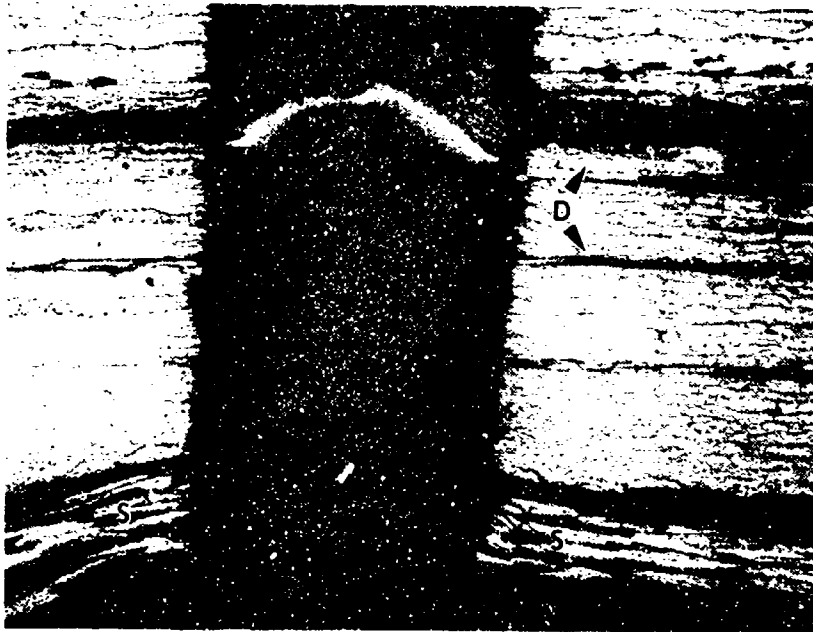
Based on all the tests performed it was concluded that failure of the part occurred due to a combination of one or more loose fasteners coupled with poor quality of the part. Under bending and torsional loads, shear cracks initiated at fastener holes, possibly leading to increased bending and buffeting of the part. The part being of poor quality eventually delaminated leading to failure.

2.12 EDITORIAL NOTES

The following comments were provided by Ms. Patricia Stumpff, the Air Force Program Monitor, concerning the following case histories presented in this part of the Technical Handbook.

2.12.1 Ballistically Damaged Composite Test Panel

The actual cause of damage was a projectile penetrating the panel from the exterior to the interior surface, not from the interior to the exterior. During the test, there was significant airflow over the exterior surface of the panel at the time of impact. This airflow apparently contributed to the ply damage on the exterior surface. However, even though the exterior surface exhibits fiber brooming similar to that seen on back sides of composite panels after impact, the hole made by the projectile is more rounded on the exterior surface than the interior surface. This would indicate an exterior to interior path for the projectile. Had a cross section of the damaged area been made, the distribution of microcracking in the composite probably would also have indicated the correct path of the projectile.



(a)



(b)

Figure 2-93. Optical Photomicrographs of Cross-Section Through Fastener Hole
 (a) Separation of Sheath (S) and Delaminations (D) in Bow
 (b) Delaminations (D) and Porosity (P) in Bow

2.12.2 Main Landing Gear Strut

There was visual evidence of a manufacturing flaw/repair in the composite bolt hole region. The relationship of this flaw to the failure was not sufficiently examined in this analysis.

2.12.3 Compound Plate and Fastener Assembly

It appears difficult to determine from the evidence exactly how, or if, the overheating of the composite was involved in the failure. Because river patterns, voids, melted and resolidified surfaces were all present, it cannot be stated with complete confidence that overheating caused the delamination. Overloads, excessive porosity or other factors could have been responsible for the failure with overheating occurring after the failure event.